8-1-2011

Evaluation of water transport in PEMFC gas diffusion layers using image analysis

Michael Daino

EVALUATION OF WATER TRANSPORT IN PEMFC GAS DIFFUSION LAYERS USING IMAGE ANALYSIS

by

Michael Mario Daino

A DISSERTATION

Submitted in partial fulfillment of the requirements
for the degree of Doctor of Philosophy
in
Microsystems Engineering
at the
Rochester Institute of Technology

August 2011

Author: _____
Microsystems Engineering Program

Certified by: _____
Satish G. Kandlikar, Ph.D.
Professor of Mechanical Engineering

Approved by: _____
Bruce W. Smith, Ph.D.
Director of Microsystems Engineering Program

Certified by: _____
Harvey J. Palmer, Ph.D.
Dean, Kate Gleason College of Engineering

NOTICE OF COPYRIGHT

Evaluation of Water Transport in PEMFC Gas Diffusion Layers Using Image Analysis

By

Michael Mario Daino

Submitted by Michael Mario Daino in partial fulfillment of the requirements for the degree of Doctor of Philosophy in Microsystems Engineering and accepted on behalf of the Rochester Institute of Technology by the dissertation committee.

We, the undersigned members of the Faculty of the Rochester Institute of Technology, certify that we have advised and/or supervised the candidate on the work described in this dissertation. We further certify that we have reviewed the dissertation manuscript and approve it in partial fulfillment of the requirements of the degree of Doctor of Philosophy in Microsystems Engineering.

Approved by:

Dr. Satish G. Kandlikar _____
Committee Chair and Dissertation Advisor — Date

Dr. Steven Day _____
Prof. of Mechanical Engineering

Dr. Maria Helguera _____
Prof. of Imaging Science

Dr. Navalgund Rao _____
Prof. of Imaging Science

MICROSYSTEMS ENGINEERING PROGRAM
ROCHESTER INSTITUTE OF TECHNOLOGY
August 2011

ABSTRACT

Kate Gleason College of Engineering
Rochester Institute of Technology

Degree: Doctor of Philosophy **Program:** Microsystems Engineering

Name of Candidate: Michael Mario Daino

Title: Evaluation of Water Transport in PEMFC Gas Diffusion Layers Using Image Analysis

Liquid water transport through the gas diffusion layer (GDL) of a proton exchange membrane fuel cell (PEMFC) was investigated through three interrelated studies utilizing the tools of image processing. First, a new framework and model for the digital generation and characterization of the microstructure of GDL materials with localized binder and polytetrafluoroethylene (PTFE) distributions were developed using 3D morphological imaging processing. The new generation technique closely mimics manufacturing processes and produces realistic 3D phase-differentiated digital microstructures in a cost- and time-effective manner. The generated distributions of hydrophobic (PTFE) and hydrophilic (carbon) regions representative of commercial GDL materials provides water transport modeling efforts with more accurate geometries to improve PEMFC water management. Second, through-plane transport in an operating PEMFC was investigated by developing and testing a transparent (visible and infrared) fuel cell. Visible observations and subsequent video processing revealed condensation of microdroplets on the GDL and implied the existence of condensation within the GDL. Temperature gradients across the cathode GDL under realistic operating conditions were obtained in a noninvasive manner using infrared imaging and subsequent image analysis. Recommendations for improving accuracy of PEMFC temperature measurements using infrared imaging were made. The final contribution of this work was the measurement and analysis of water breakthrough dynamics across GDL materials with and without microporous layers (MPLs). Dynamic breakthrough events, or recurrent breakthroughs, were observed for all GDL material investigated indicating the breakdown and re-build of water paths through the GDL caused by an intermittent water drainage process from the GDL surface. GDL materials without an MPL exhibited a dynamic breakthrough location phenomenon and significantly elevated water saturations. The results suggest that the MPL not only limits the number of water entries into the GDL substrate but also stabilizes the water paths. These dynamic breakthrough events were explained in terms a Haines jump transport mechanism. The main contributions of this work are: (1) Development of a new digital GDL microstructure generation algorithm, (2) Evaluation of infrared temperature measurements in the through-plane direction of a PEMFC, and (3) Identification of a new water transport mechanism in GDL materials.

Abstract Approval: Committee Chair _____

Program Director _____

Dean KGCOE _____

ACKNOWLEDGMENTS

I would like to thank my advisor, Satish Kandlikar, for providing me this great opportunity to be a member of his research team. The knowledge that I have gained under his advisement has far exceeded any and all expectations. His unending excitement for his career is an inspiration to all.

A special thanks to my wife, Stefanie, who fully supported me throughout this experience. I am forever grateful for her patience and understanding. Without her continuous support, this would not have been possible.

I would also like to thank my parents, Bill and Linda, who endured my younger years and provided unwavering encouragement throughout life's challenges. To my father, who taught me that hard work always pays off and to my mother who "made me go to college", many thanks.

Support for this project was provide by the US Department of Energy under award numbers: DE-FG3607GO17018 & DE-EE0000470 and by the New York State Energy Research and Development Authority under contract no. 9575.

Contents

List of Figures

Chapter 1

Introduction

1.1 Motivation

The demand for petroleum is ever increasing with 70 % of the United States' total consumption fueling the transportation sector [1]. This demand for petroleum cannot indefinitely be met as world-wide supplies of fossil fuels continue to be reduced, further increasing costs and may eventually lead to prohibitively expensive gasoline prices for private transportation. In addition, 43 % of the United States' carbon dioxide emissions from 2000-2006 were solely from petroleum consumption [1]. This establishes transportation as a sector where significant progress can be made to reduce both national petroleum imports and greenhouse gas emissions. The proton exchange membrane fuel cell (PEMFC) is considered one of the most promising technologies to displace the internal combustion engine in the private transportation sector due to its high efficiency, low emissions, quiet operation, quick startup and refueling, and variety of feedstocks for hydrogen fuel production [2].

PEMFCs use hydrogen and oxygen to generate electricity with water and heat as the only byproducts of the electrochemical reaction. Although water is a byproduct and needs to be removed from the cell, the most widely used membrane (Nafion®) must remain hydrated to sustain protonic conductivity [3]. An overabundance of water in a PEMFC

may block reactant pathways and/or catalytic sites significantly impacting performance and may potentially lead to cell failure. Maintaining a sufficient amount of water in the cell without hindering reactant transport is a critical aspect of PEMFC research that continues to be widely studied [4–8]. Thus, effective water management in PEMFCs is critical for high performance, reliability, efficiency, and vital in cold-start environments. Specifically, the gas diffusion layer (GDL) strongly affects the water distribution throughout the cell and must be well characterized in terms of material properties and microstructure for evaluation of its effect on cell performance and longevity.

1.2 Proton Exchange Membrane Fuel Cells

Proton exchange membrane fuel cells are electrochemical devices that convert chemical energy in hydrogen molecules into electricity. The materials used on the cathode and anode of a PEMFC are typically mirror images of one another. The major components are shown in the schematic of a PEMFC cross-section in Fig.1.1. The gas distribution channels usually have hydraulic diameters of a millimeter or less and are made of an electrically conductive material such as graphite. The gas channels supply hydrogen to the anode and oxygen (usually air) to the cathode and also remove excess water from the cell. The regions between the channels (referred to as lands or ribs) in contact with the GDL surface allow for current to flow from the anode where hydrogen is oxidized to the cathode where water is produced. Gas diffusion layers are generally made of graphitized carbon paper or cloth and are highly porous (ϵ >70 %) with pore sizes of about 10-30 μm for paper GDL [9]. The microporous layer (MPL) is an additional layer of carbon particles and polytetrafluoroethylene (PTFE) and in the absence of cracks has pores much smaller (around 0.1-0.5 μm) than the GDL substrate [9]. The cracks in the MPL shown in Fig. 1.1 play an important role in PEMFC water management and will be discussed in detail in chapter 5. The catalyst layer (CL) is comprised of nanoparticles of carbon supported platinum (shown as

silver spheres on larger black spheres) and ionomer (shown in green) from the PEM. The PEM is typically based on chemically stabilized perfluorosulfonic acid/PTFE copolymer in the acid form made by DuPont™ under the name Nafion®.

The operation of a PEMFC can be described by following the path of the reactants and product water through the fuel cell materials. Hydrogen is supplied to the anode by gas distribution channels where it diffuses through the anode GDL and MPL into the anode CL. In the anode CL, hydrogen is oxidized and the electrons are conducted back through the MPL and GDL into the lands of the anode gas distribution channels. The free electrons flow through an electric load (electric motor for automotive applications) as they travel toward the cathode. The PEM conducts the protons toward the cathode where they are joined by the electrons and oxygen that conducted and diffused through the cathode GDL and MPL from the cathode gas distribution channels and lands, respectively. The protons, electrons, and oxygen react in the cathode CL to form water and heat. The half cell and overall reactions are shown in Eq.1.1.

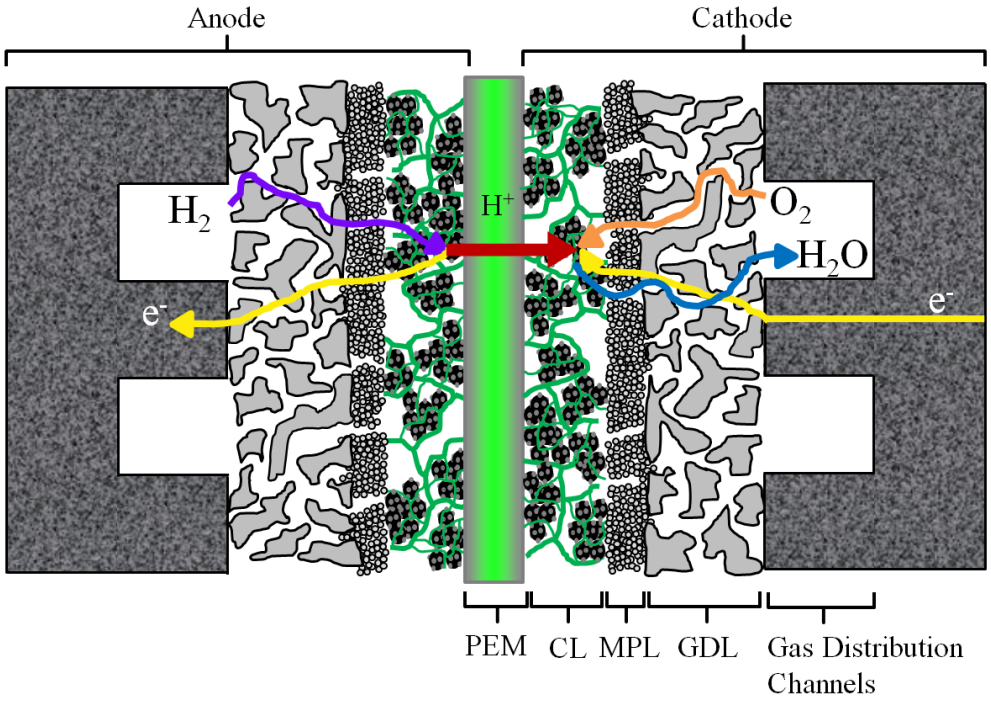

Figure 1.1: PEMFC schematic (not to scale).

$$\begin{aligned} \text{Cathode:} \quad & 1/2O_2 + 2H^+ + 2e^- \rightarrow H_2O \\ \text{Anode:} \quad & H_2 \rightarrow 2H^+ + 2e^- \\ \text{Overall:} \quad & O_2 + 2H_2 \rightarrow 2H_2O \end{aligned} \tag{1.1}$$

1.3 Gas Diffusion Layer Materials and Properties

Gas diffusion layers used in PEMFCs are essential for efficient operation and play a pivotal role in water management. The requirements of a GDL material can be summarized as follows:

1. Distribute reactants uniformly to catalyst layers
2. Provide pathways for water removal
3. Conduct electrons and heat
4. Provide mechanical support to membrane
5. Resist compression into channels

The two general types of GDL materials used in PEMFCs that meet these requirements are carbon fiber paper and carbon fiber cloth. Carbon fiber paper is generally manufactured using paper manufacturing techniques with a binding substance and is typically treated with PTFE to increase hydrophobicity prior to use. Carbon fiber cloth is made by weaving carbon fibers together and thus does not require a binder material but is also typically treated with PTFE prior to use. A commercially available and widely used carbon fiber paper and carbon fiber cloth GDLs produced by Toray Industries, Inc. are shown in Fig. 1.2.

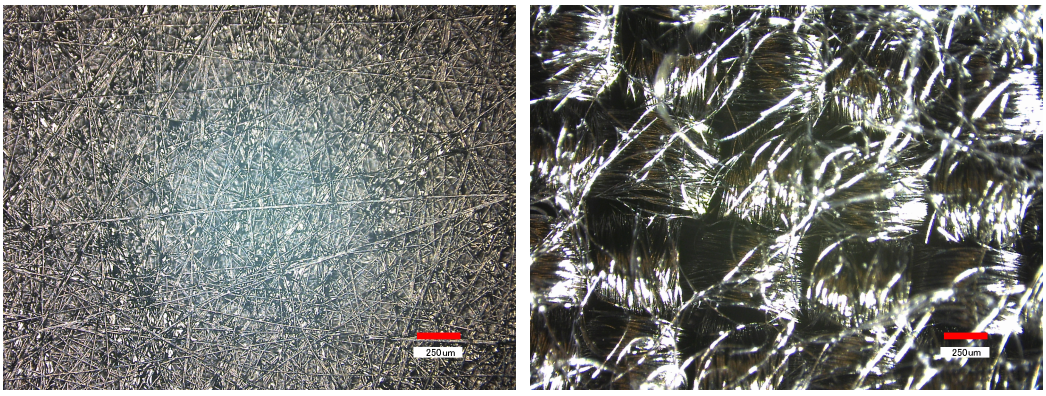

(a) Carbon fiber paper (b) Carbon fiber cloth

Figure 1.2: Digital microscope images of general GDL types (Toray Industries, Inc.).

There are significant differences in the material properties among the commercially available carbon fiber paper GDLs. Sample confocal laser scanning microscope (CLSM) images of four carbon fiber paper GDLs can be seen in Fig.1.3. Qualitative differences in the GDL substrates and binding material can clearly be seen in the figure. The binding material of TGP-H-060 0 wt.% PTFE (Toray Industries, Inc.) can be characterized as large smooth sections spanning across multiple fibers as opposed to the binding material of SGL 25BC (SGL Carbon Group) which is rough and coats most of the fibers but spans across a smaller area. The binding material used in Freudenberg H2315 is similar in structure to that of SGL although used much more sparingly rarely spanning across fibers. MRC (Mitsubishi Rayon Corp.) 105 uses binder that restricts access in/out of the material similar to Toray except that it has many smaller irregular openings throughout which resemble a spider's web. As Fig.1.3 illustrates, the binding material may have a significant impact on the accessibility of drainage locations for water migrating out from the cathode CL or emerging from the GDL into the channels. The differences in restrictions to the surface of the GDLs are further contrasted in the 3D images of the TGP-H-060 0 wt.% PTFE versus Freudenberg H2315 shown in Fig.1.4.

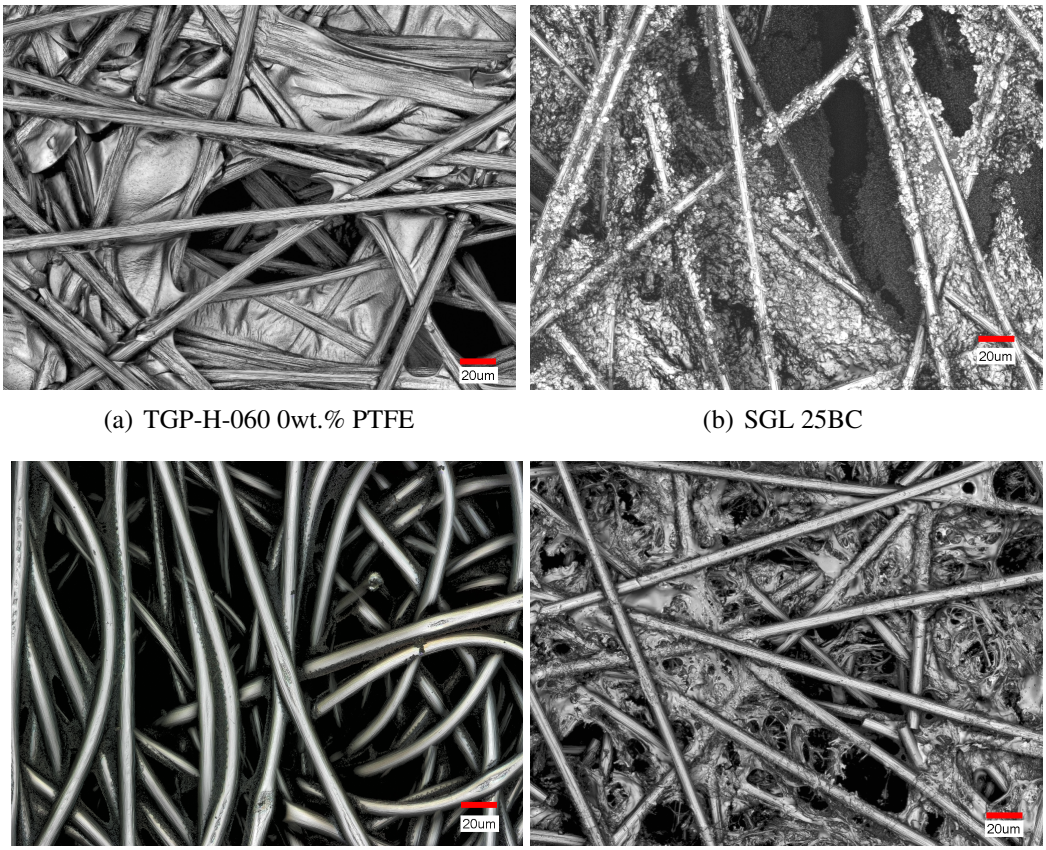

(a) TGP-H-060 0wt.% PTFE (b) SGL 25BC

(c) Freudenberg H2315 (d) MRC U-105B

Figure 1.3: Confocal laser scanning microscope images of GDL materials.

1.4 GDL Microstructure and Water Management

The flow of reactants and product water through GDL materials is highly dependent on the microstructure and material properties. A low porosity GDL has limited flow paths for the reactants to reach the catalyst layers as well as for the transport of the liquid water from the cathode CL to the gas distribution channels. Thus, for PEMFC applications, highly porous GDLs are used with specific attention given to the associated trade off with other material properties such as conductivity and mechanical strength. Similarly, a strongly non-wetting GDL would require significant pressure for the water to enter the pore network and a strongly wetting GDL would saturate with water leaving insufficient reactant pathways. In order to develop an optimized GDL for PEMFCs, both the microstructure and material

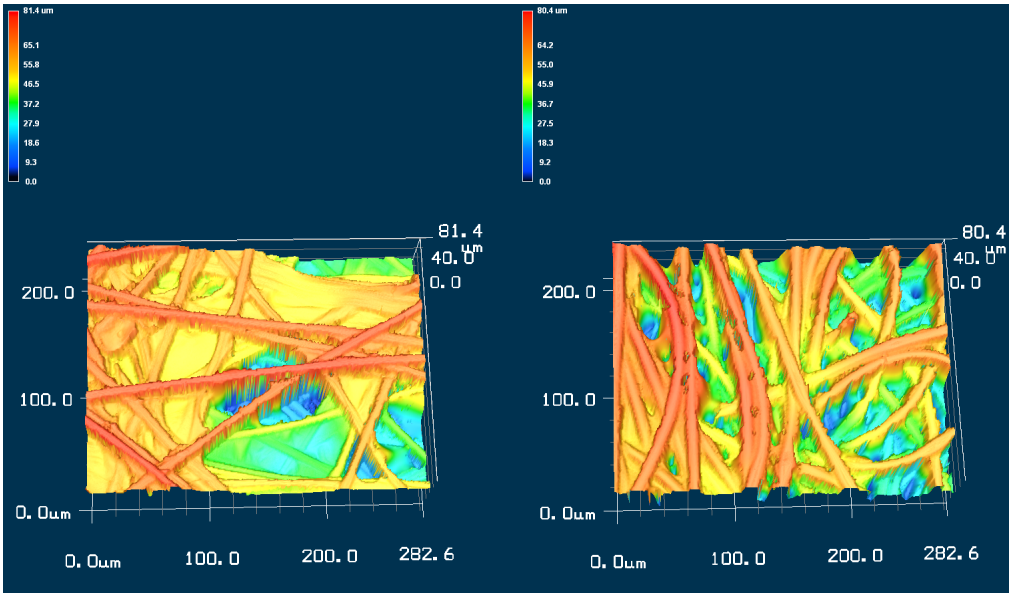

Figure 1.4: 3D CLSM images of TGP-H-060 0 wt.% PTFE (left) and Freudenberg H2315 (right).

properties need consideration.

The microstructure of GDL materials can vastly vary as was exemplified for common GDLs in §1.3. The pore size distribution, porosity, fiber diameter distribution, binder characteristics, and tortuosity of the microstructure strongly affect the availability and length of flow paths for both reactants and product water. Additionally, the dominant forces governing the fluid transport are functions of the scale and geometry of the microstructure as well as the fluid properties. In order to accurately model the liquid water transport through GDL materials, the microstructures need to be sufficiently characterized.

Water management in PEMFCs has been identified as critical for performance and efficiency [4,6,10–12]. Water management in PEMFCs is aimed toward optimizing the hydration of the membrane without excess water blocking reactants in the gas channels, GDL, MPL, or CL. Water hold-up within the GDL requires additional consideration for efficient cold-starts in northern climates. An under hydrated PEM has reduced protonic conductivity and an overabundance of water within the fuel cell causes mass transport losses. Both of these extremes reduce fuel cell performance and may lead to cell failure. Water distri-

bution and transport processes are not completely understood in PEMFCs and thus there is a tremendous need for a fundamental understanding in order to design and operate an optimized PEMFC.

1.5 Objectives

The main contribution of this work was to increase understanding of water transport through a GDL of a PEMFC with three interrelated objectives. The first objective was to develop a mathematical model to digitally generate the three-dimensional (3D) microstructures of GDL materials incorporating both carbonized binder and wet-proofing treatments. The developed software will allow for intuitive input parameters such as global porosity, fiber radius, etc. of the GDL material and the resulting structures can then be readily used for analyzing transport processes using commercial CFD software packages. The second objective was to study through-plane transport processes in a PEMFC using visible and infrared imaging of a newly designed transparent fuel cell. The visible imaging allowed for high-magnification examination of the GDL cross-section and the infrared imaging revealed the temperature gradient across the GDL. The third and last objective of this work was to investigate fundamental water transport mechanisms through GDL materials in a well-controlled ex situ experiment. The ex situ experiments allow for characterization of water transport properties in the GDL that are otherwise impractical. The combination of these objectives investigates the GDL material using ex situ, in situ, and microstructure modeling approaches for improved understanding of transport processes.

Chapter 2

Literature Review

2.1 GDL Numerical Modeling

Liquid transport in porous media has been modeled on the pore scale with a variety of methods and can be broadly classified as rule-based and first-principle based methods [13]. A comprehensive review of modeling approaches for flow in porous rocks can be found in [14]. Rule-based approaches incorporate the governing physics of the transport mechanisms in the porous medium on a regular idealized representative geometry. Promising rule-based approaches that have been applied to GDL liquid transport modeling are pore network [15–27] and full morphology models [28]. As the classification implies, first-principle based models are built from first principles to predict the transport on a discretized grid. Applying CFD methods to study GDL liquid transport has been a challenging task due to the complex boundary conditions imposed by GDL microstructure. To overcome this difficulty of standard CFD methods, Lattice Boltzmann (LB) methods have been utilized to simulate the liquid transport through GDL materials [29, 30]. The rule-based and first-principle based models require vastly contrasting computational resources and complexity which may not be necessary or more accurate for GDL transport modeling [25]. Although these modeling approaches fundamentally differ from one another, each method

requires an accurate representation of the microstructure and material properties.

2.1.1 Stochastic GDL Generation

Gas diffusion layers commonly used in PEMFCs (e.g. Toray TGP-H) are comprised of graphitized fibers and carbonized resin and are usually treated with PTFE to increase hydrophobicity prior to in situ testing [9]. The distribution of these solid phases as well as their three-dimensional geometry within a GDL has been challenging to determine due to the opaqueness and multiple length-scales of GDL materials. Advanced three-dimensional (3D) imaging techniques utilizing x-rays (synchrotron [31, 32] or non-synchrotron [20, 33–37]) for computed tomography reconstruction of GDLs have recently been employed to reveal the 3D microstructure with various spatial resolution and contrast between GDL material and void. The distributions of carbonized resin, graphitized fibers, and wet-proofing agent (e.g. PTFE) are highly desired for transport modeling but the ability to differentiate these phases throughout the GDL remains a considerable challenge. Additionally, the time required and expense of sophisticated micro-CT (computed tomography) imaging systems is prohibitively substantial. A relatively new method utilizing the field of stochastic geometry to predict the internal microstructure of GDL materials has proven to be a valuable tool to ascertain GDL 3D geometry and composition in a cost- and time-effective manner [28]. Stochastic generation has been applied to various porous materials including coalescers [38], acoustic trim [39], solid oxide fuel cell electrodes [40], PEMFC GDL [28–30, 41–44], and PEMFC catalysts [29, 45, 46]. Since the initial application of stochastic geometry to generate a virtual GDL by Schulz et al. [28] in 2007, many studies have used the original concept [39] for pure fiber GDLs [29, 41, 47, 48], fiber with carbonized resin (referred to as binder) [32, 42–44, 49], or fiber with PTFE but without binder [30].

Schulz et al. [28] were the first group to apply stochastic generation to “reconstruct” GDL materials to obtain the 3D microstructure for the simulation of liquid flow. The frame-

work of the authors' generation algorithm used the following assumptions for carbon fiber paper digital generation:

- Fibers infinitely long
- Fiber crimp is negligible
- Fibers may intersect
- Fiber system is macroscopically homogeneous and isotropic the in-plane direction

Utilizing these assumptions enabled the use of a stationary Poisson line process model with a one parametric directional distribution for GDL fiber system. The fibers were attached to the lines generated by the Poisson line process and the directional distribution was given in polar coordinates as a function of altitude in terms of density:

$$\rho(\theta) = \frac{1}{4\pi} \frac{\beta sin\theta}{(1(\beta^2 - 1)cos^2\theta)^{\frac{3}{2}}} \tag{2.1}$$

where β is anisotropy parameter with β = 1 represents an isotropic system and increasing β results in a more layered structure with fibers accumulating in planes. The digital generation of Toray TGP-H-090 and SGL 10BA were computed using β values of 10,000 and 100, respectively. The results of the generated structures' pore size distribution and permeability were in good agreement with experimental data validating the overall technique. It is also worth noting that Schulz et al. [28] developed a full-morphology (FM) model to simulate water transport through the generated GDL materials.

The work of Schulz was extended by Thiedmann et al. [42] by including the effects of the carbon binder used in the manufacturing of GDL materials. The mathematical model used for the addition of binder assigned a probability of being filled with binder to each non-fiber (pore) region of each layer of the fiber skeleton. This method was referred to as Bernoulli filling and resulted in horizontally oriented sections of binder. The generation of binder material was further improved by Becker et al. [32] where the binder was treated

as a wetting-fluid by filling the smallest pores first. The authors used the morphological opening of spheres of increasing radius on the fiber skeleton to determine the pore size for each voxel throughout the digital structure. The voxels were then filled with binder material in ascending order until the desired porosity was achieved. Hao and Cheng [30] used the algorithm proposed by Schulz et al. [28] for the fiber skeleton and built upon that method by incorporating the addition of PTFE but did not consider binder. PTFE was added by randomly filling voxels near fibers until the desired porosity for the particular PTFE loading was achieved.

Since GDL carbon paper materials used in PEMFCs usually have a carbon binder material and are generally subsequently treated with PTFE, there is clear need for a digital generation algorithm that fully incorporates both phases. The addition of the binder and PTFE should mimic actual manufacturing processes and allow for intuitive realistic input parameters. A phase-differentiated (fiber, binder, PTFE, and void) 3D model of the GDL microstructure can then be generated in a cost- and time-efficient manner which can be used for transport modeling with any of the model approaches.

2.1.2 Pore Network Modeling

Pore network modeling has been used to gain insight into the liquid transport within a porous media in a computational efficient manner. This rule-based modeling approach is accomplished by first reducing the complex interconnected pore structure of porous media to a representative network of regular pores (e.g. spheres). Liquid transport modeling through the representative simplified network is much less computationally expensive and avoids associated challenges with the true geometry. Through this method, fluid transport can be simulated and the effects of material properties such as pore distribution, porosity, and wettability and can be quickly evaluated.

Pore network modeling has been successfully implemented for a variety of porous media dating back to the pioneering work of Fatt in 1956 [50–52]. There is a vast variety of

applications for liquid transport in porous media including, pharmaceuticals, paper industry, oil recovery, PEMFC GDL, and many others which has motivated the study of pore networks for porous media in the generalized form [53–57]. Current advances in pore network modeling from its early starts can be found in review papers for the interested reader [58–60].

Water transport modeling in GDL materials typically neglect dynamic interactions on the pore scale and are more focused on steady-state condition of water flow paths. However, dynamic behavior of water transport has been observed experimentally in two aspects: recurrent breakthroughs and dynamic breakthrough locations [61]. These phenomena can be explained in terms of Haines jumps used in geological disciplines [62]. Haines jumps are a description of discontinuous drainage displacements where the non-wetting fluid (water in GDL) in a porous media becomes disconnected (or choked-off) due to constrictions in the pore network. These phenomena have yet to be simulated in pore networks for GDL materials and may play a vital role in water transport.

2.2 Imaging Techniques for PEMFC Research

The water transport through each of the layers of a PEMFC has been significantly difficult to study due to material opaqueness and multiple length scales. Some of these challenges have been met using a variety of imaging modalities to reveal fundamental water transport mechanisms through PEMFC materials. These imaging techniques have been vital to the understanding of water transport for direct visualization of the processes as well as quantifying the water throughout the fuel cell. Coupled with additional measurements of physical quantities of the system, imaging techniques provide a greater fundamental understanding than the physical quantities alone. Additionally, imaging techniques provide a variety of observations on the fuel cell that may not be obtained by other means.

A wide variety of imaging techniques has been employed for PEMFC research to aid

in our understanding of the physical phenomena within the cell with several reviews given in [63–69]. Imaging objectives range from material characterization to two-phase flow in the gas distribution channels. Imaging systems gather information on the specimen or processes under study that is unique to the system's operating principles. Imaging specimens using different imaging modalities can often complement one another in order to gain a greater understanding than either could reveal independently. PEMFC water management studies have utilized visible, infrared, X-rays, fluorescence microscopy, nuclear magnetic resonance (NMR), and neutron radiography to visualize water, measure temperature distributions, and quantify water content.

Visualization of water content and transport in PEMFCs is crucial in a comprehensive understanding of fuel cell operation. Imaging systems in various modalities have been and are currently being developed to reveal and measure physical properties of fuel cell components with a specific interest in water observation and quantification. Direct visualization with reflected visible light has been able to reveal flow regimes for two-phase flow in the gas distribution channels, droplet emergence phenomenon, contact angles, and quantification of water in the gas distribution channels (with subsequent processing techniques). Visible light imaging systems utilize a very mature technology that has been used for over 400 years and offers the most intuitive means of visualization. Infrared imaging can obtain non-contact temperature distributions without the use of intrusive probes or sensors (e.g. thermocouples). The overall electrochemical reaction in the fuel cell is exothermic and thus the temperature distributions allow for the study of local current densities. X-ray imaging has the potential for high spatial resolution but contrast between water and fuel cell materials can be challenging. Fluorescence microscopy has been employed for ex situ studies of water transport phenomena within top most portions GDL materials but would require novel methods to be used during in situ observations. Neutron imaging has the advantage that fuel cell hardware modification from what is typically used is minimal (if at all) which is generally required by other imaging techniques. Neutron radiographs measure water

thickness but require extremely sophisticated imaging systems requiring a nuclear reactor and beam time in established facilities is in great demand. Magnetic resonance imaging (MRI) has been applied to PEMFC research only through severe modification of fuel cell hardware required by eliminating ferromagnetic materials and using conductive materials in moderation and only when absolutely necessary.

2.2.1 Visible

Visualization studies utilizing visible light, roughly in the range of wavelengths 400 nm $\leq \lambda \leq$ 700 nm, are intuitive to interpret and have revealed a variety of water transport phenomena. The simplest experimental setup consists of an in situ or ex situ visualization test section, light source, and light measuring device. In situ experiments typically require flow fields that are modified with a visibly transparent plate or window to allow for live observation of the water content in the gas distribution channels. Visibly transparent materials reported in literature are usually polycarbonate (Lexan®) or polymethyl methacrylate (Acrylic) although there are many other materials that could be used. The addition of a viewing window changes the physical properties of the channel, such as surface energy and heat transfer properties, but still reveals valuable information on the water transport between the channel and GDL.

The light that is incident on the fuel cell materials such as GDL, MPL, or CL is generally reflected or absorbed from these opaque materials. The light that is reflected is captured with an optic, focused onto a focal plane, and measured by a light sensitive device (or material such as photographic film). Image contrast is achieved from local differences in material reflectivity and/or topology using uniform illumination. Visible imaging can be used with a wide field of view for overall assessment of the cell, e.g. gas distribution channels, or high magnification can be used to study fine features such as droplet formation.

Visualization with visible light is relatively straightforward but the incorporation of an observation window may prove to be challenging. The availability of imaging sensors

and optics makes these imaging systems cost effective and with state-of-the-art supporting software, relatively simple to operate. There are many high-speed cameras that far exceed temporal resolutions of other modalities that can capture transient phenomena otherwise unobtainable. One disadvantage to using an observation window is the modification to the fuel cell could affect the phenomenon under study and thus must be carefully considered.

There have been many studies reported in the literature using reflected visible light due to cost and availability of the associated mature technology. Transparent PEMFCs have been developed for studying water in cathode channels [70–86], anode channels [72, 76, 86, 87], cathode CL [88–90], and even 'within' GDL by cutting groves [91]. These techniques provide direct qualitative observation of the PEMFC and when correlated to physical measurements, provide a more complete understand of the phenomenon under study.

Ex situ experiments have utilized for investigating water transport properties such as GDL intrusion into gas distribution channels [92], dynamic water breakthrough phenomena [61], two-phase flow patterns for parallel channels under automotive operating conditions [93], and investigating the effects of channel properties [94]. Chen [95] used an ex situ experiment to study the dominate frequency of the pressure drop in two 1.5 x 1.2 mm parallel channels. Carbon foam was used by the author to simulate the intrusion of actual GDL materials and video was captured at the outlet. The dominate frequencies of the pressure drop data were correlated to water flow patterns in the channels. Chen [96] studied the effect of filling the reactant channels with foam inserts on the flow patterns and associated pressure drop. The author found the foam inserts exhibited significantly less mal-distribution with a four-fold two-phase pressure drop penalty. Yu et al. [97] also utilized an ex situ test section with visualization to validate the use of double parallel conductance probes for detection of flow patterns in gas channels. Ex situ experiments allow for more control over the experimental conditions and specific transport properties can be isolated that may be extremely difficult to perform in an in situ environment.

Lu et al. [93] mimicked automotive operating conditions in an ex situ experiment by back calculating the water flow rates from current density and air flow rates from cathode stoichiometry. Film, mist, and slug were found to be functions of the water and air flow rates. Further analysis of the ex situ data showed that there is a maldistribution of flow in parallel channels due to the presence of water. Maldistribution in flow channels of PEMFCs reduces performance and can lead to material degradation [98, 99].

In situ imaging allows for direct access gas distribution channels to monitor water accumulation and removal. Visible images and video are very intuitive to interrupt due to our familiarity with the visible spectrum. Figure 2.1 is a sample image from an in situ experiment where the fibrous GDL structure can be clearly seen in the channels. The image was captured with a Photron fastcam 1024 pci high-speed camera equipped with a long working distance microscopic lens. Details of the experimental setup can be found in [100]. The image in Fig.2.1 is a sample of three of twenty-two cathode gas distribution channels that portrays both droplet formation (circled) as well as film flow (boxed).

Hector et al. [101] measured the strain accumulation in membrane and MEA materials after a single hydration/dehydration cycle using digital image correlation between consecutive images during drying period. The membranes and MEAs used were initially marked with contrast marks to allow for correlation after the hydration/dehydration cycle. A digital image correlation algorithm was used to correlate the contrast marks to a digital grid pattern for cumulative or incremental correlation. A digital grid (37 x 48) was placed over each image to act as a strain gauge. The digital image correlation was able to provide cumulative strain maps for the samples as well as the drying induced strains at each pixel location. The algorithm was able to compute the strains for most of the field of view with an area of $\approx$ 1500 mm^2 on the membranes and MEAs with an uncertainty of 100 microstrains. A 3D DIC technique has recently been developed to measure the local thickness and compressibility of GDL materials [102].

Droplet formation, growth, and detachment on a cathode GDL have been studied by

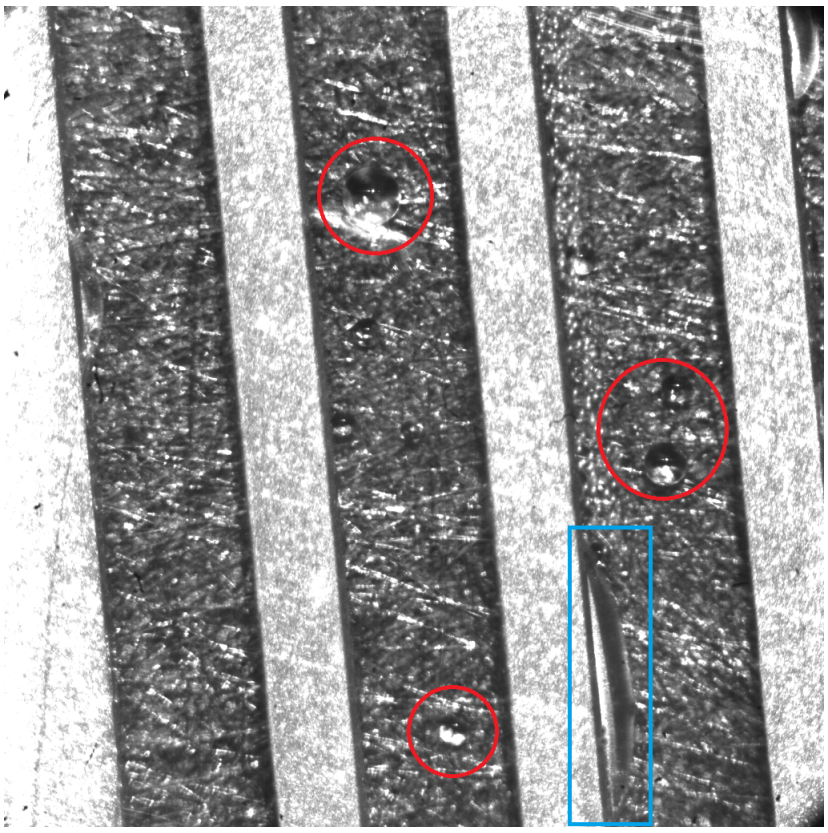

Figure 2.1: Example image of in situ cathode channel visualization. Note lands are 0.5 mm wide.

Yang et al. [82] utilizing transparent polycarbonate windows for visible imaging. Through direct observation of the flow channels, it was observed that droplets emerge from preferential locations on the GDL surface. The droplets grew until they made contact with the channel walls and wicked onto them due to the hydrophilicity of the channel walls. The water was removed from the channels in an annular flow. It was observed that under practical stoichiometric ratios two-phase flow in the cathode channel was dominated by annular film flow.

Zhang et al. [83] studied the detachment diameter of a droplet from carbon paper as a function of Reynolds number. The authors empirically derived an expression for the detachment diameter for the particular GDL used as a function of air Reynolds number. Zhang et al. [83] also utilized the captured video to mathematically model the spreading

factor of the droplets on the hydrophilic walls.

Water flow in gas distribution channels is an important parameter in understanding water transport and removal from the fuel cell but water transport begins in the CL, MPL, and GDL. However, due to their opaque nature, additional modifications to the fuel cell are necessary to visualize water transport through them. Ge and Wang [89] studied water and ice formation on the cathode CL under cold start conditions by utilizing a silver mesh as the cathode GDL. Optical access directly to the surface of the cathode CL was obtained through the 0.38 x 0.38 mm openings between the wires and was monitored for water formation during cold start conditions. Water droplets were observed to form and grow on the CL with diameters in the range of 10-40 μm. Water was differentiated from ice/frost particles by observing the captured images as a video which revealed that the droplets were clearly growing. The droplets were confirmed to be liquid through a quenching experiment during which the cell was cooled to -3°C for 2 hours. During the quenching, the droplets underwent a phase transition where their perimeters transitioned from round to irregular. The cell was then allowed to warm to room temperature and the ice particles melted and the resulting water was wicked onto the hydrophilic silver mesh. Although the silver mesh GDL allowed for direct visual access to the CL surface, it exhibited large thermal and electrical contact resistances that are not characteristic of commercial PEMFCs.

Ge and Wang [90] modified their experimental setup to better represent commercial PEMFC by using cutting micro-holes with diameters $\approx$ 400 μm were cut into the cathode GDL (Carbon paper) along the length of the channel to obtain visible access to the CL. Under cold start conditions of -1°C and -3°C water formation was captured using a digital camera equipped with a zoom lens. Through the micro-holes, water droplets with diameters 10-50 μm were observed on the CL. The authors confirmed that the droplets were indeed water and not ice or frost through the same quenching procedure previously described.

Ge and Wang [87] utilized a similar experimental setup to study water formation and transport in the anode channels of a PEMFC as they did for their cold start experiments

previously described. Water droplets or water film were not observed in the anode channels for 0.5 or 0.8 A/cm^2. Under these higher current densities there is a higher water flux from the anode to the cathode from electro-osmotic drag and thus less water accumulates in the anode channels. It was found that current density is the controlling parameter for water formation in the anode channels. Water droplets were captured for a current density of 0.2 A/cm^2 and their locations (whether on GDL or window surface) were distinguished by comparing images taken under different lighting conditions. One image was taken with illumination at normal incidence and the other with just ambient light using a longer exposure. The reflection from the droplets with the normal incidence revealed that the droplets are formed on the channel walls or the transparent window but not on the GDL surface. Using the ambient light condition, it was observed that water droplets never emerge from the GDL under any of the operating conditions studied. This revealed that water clogging of the anode channels does not come from the GDL in liquid form but rather in vapor form followed by condensation. This formation of water in the anode channels is rather slow and longer experiments (2 hours) were carried out to reveal anode flooding. Droplets were observed to form, grow, and eventually clog the channel. The effect of GDL hydrophobicity was also investigated by the authors. It was found that a hydrophilic GDL would wick a growing droplet from the channel wall and the channels would not be blocked. However, this wicked droplet would absorb into the GDL blocking reactant pathways and may lead to local fuel starvation.

Kimball et al. [103] used a transparent fuel cell to study the correlation between liquid water in the cathode reactant channels to the local current. The authors found that droplets emerge from the largest pores in the GDL and form slugs causing local currents near the outlet to drop. Jiao et al. [104] used a transparent PEMFC to study the effect of compression on through-plane water transport in the GDL from channel to channel and found that air flow rates have a significant effect on water removal from under the land regions. An optical reconstruction technique was applied to image data captured at various precise sample to

lens distances by Berejnov et al. [105]. These images were then analyzed to determine the depth at each pixel location producing a 3D surface image of the GDL samples. The resulting 3D images that were obtained in a cost-effective manner (through digital image processing) are similar to that produced optically by a confocal laser scanning microscope.

2.2.1.1 Confocal Laser Scanning Microscopy

Confocal microscopy has considerably increased the capability of optical microscopy in terms of contrast and spatial resolution. Employing the principle of confocal optics has enabled microscopists to obtain unparalleled three dimensional images of specimen as well as optical sectioning in the axial direction. However, this increase in resolution, contrast, functionality in confocal imaging systems, specifically confocal laser scanning microscopes (CLSMs), are obtained at the price of complexity and cost of the system as well as reduced temporal resolution. CLSM systems require a series of precisely aligned optics, specially designed objectives, laser sources, specialized computational capabilities, and other periphery equipment not required by conventional microscopes. Although there are significant technical difficulties associated with a CLSM and lower temporal resolutions than digital microscopes, confocal imaging systems have been used extensively in biology for many years and recently have been applied to many other disciplines.

A CLSM has a significant reduced temporal resolution due to raster scanning the image pixel-by-pixel. A single photon detector is used to measure the image pixel-by-pixel in a serial fashion opposed to a focal plane array used in convention digital microscopes that independently capture the light at each pixel location. Scanning at acceptable rates for dynamic processes is significantly difficult to achieve in current CLSMs. Specialized systems have been developed that can achieve video rates (30-60 fps) but this temporal resolution is much lower than conventional digital microscopes (Over 10,000 fps and much higher using pixel binning or subwindowing).

A scanning confocal optical system, first patented by Marvin Minsky in 1957, used in

microscopy has many clear advantages over conventional microscopes. As outlined in Minsky's patent the advantages include: Reduced blurring from scattered light, increased resolution, improved signal-to-noise ratio, permits clear observation of thick light scattering specimens, z-scanning can be achieved, and electronic adjustment of magnification [106]. Although the basic principle was patented in late 1950's it wasn't until the later 1980's that CLSMs were first available on the market. This delay in the development in a commercial CLSM system was mostly due to the invention and development of the laser as well as the essential computational power required that was made possible from advances in computer technology.

A CLSM employs the use of epi-illumination and a pinhole to increase contrast and to obtain three dimensional images of specimens. CLSMs use a collection of optics, electronics, and a detector to collect and measure two and three dimensional high resolution images. CLSM are confocal in the sense that the objective lens is used to illuminate and image the specimen and thus uses epi-illumination. The objective focuses light onto only a small portion of the specimen and only light that was reflected from the small illuminated volume will be captured by the objective. A pinhole aperture is used to collect light reflected from only a narrow thickness into the specimen. Light collected by the objective lens that is not from the volume in focus including any background light, is not measured by the detector because it is blocked by the pinhole. This ability to 'ignore' out of focus light is illustrated in Fig. 2.2 using simple ray tracing. In the configuration shown in Fig. 2.2, only the object represented by the green arrow would reach the detector and the rays from the out of focused object (black arrow) are blocked by the pinhole.

The pinhole provides a method to evaluate only a narrow depth into the specimen without having the additional blur from the out of focus planes. Planes perpendicular to the optical axis (along the axial direction) in the object plane will only be in focus over the objective lens' depth of field. The depth of field of an objective is given by [107]:

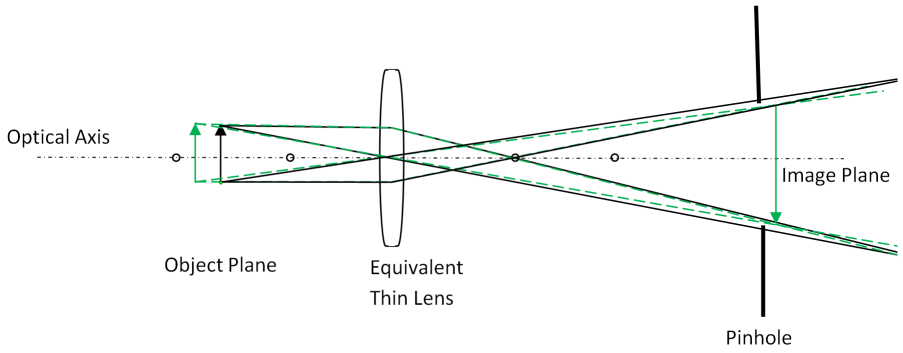

Figure 2.2: Illustration of operating principle of confocal pinhole system with simple lens. Note that rays from the black arrow are blocked by the pinhole and do not reach the image plane where the image is recorded.

$$Z_{field} = \frac{n\lambda}{NA^2} \tag{2.2}$$

where n is the index of refraction of the material between the objective and the specimen, λ is the wavelength, and NA is the numerical aperture. The numerical aperture is defined as:

$$NA = nsin\theta \tag{2.3}$$

where n is the index of refraction of the medium between the objective lens and the specimen and θ is the half-angle of the maximum cone of light that can be collected by the lens. The NA of an objective is commonly used as a measure of the maximum resolution that can be achieved by an objective. As Eq. 2.2 shows, NA is also a measure of the depth of field of the objective. As NA increases, the distance along the optical axis where the specimen will be in focus will decrease. This decrease of the depth of field with increasing NA results in axial resolution increasing. In addition to an increase in axial resolution, the lateral resolution of the objective also increases with increasing NA and is discussed in detail later in the text.

In order to obtain different object planes in focus, referred to as optical sectioning, the objective or specimen stage can moved by a step motor. This is necessary because typical objectives have a fixed working distance. The plane that will be in focus is centered about the working distance of the lens. Thus, the working distance also gives the overall range in the axial direction that confocal images can be obtained for a given objective.

Conventional microscopes use white light and the image is collected either by the retina, film, or electronic detector such as a charge-coupled device (CCD). These collected images are two dimensional and the commonly used resolution criterion to compare imaging systems (often referred to as the diffraction limit) is given by Rayleigh's criterion:

$$\Delta r = 1.22\lambda f/\# \tag{2.4}$$

where Δ r is the minimum distance between two point sources in the object plane and f/# is the f-number of the objective defined by:

$$f/\# = \frac{f}{D} \tag{2.5}$$

where f is the effective focal length and D is the diameter of the objective. For applications where air is the medium between the objective and specimen (n $\approx$ 1) and utilizing the paraxial approximation, the f-number can be written as:

$$f/\# = \frac{1}{2NA} \tag{2.6}$$

Using the reasonable approximation in Eq. 2.6, the Rayleigh criterion can be written as:

$$\Delta r_{min} = \frac{1.22\lambda}{2NA} = 0.61\frac{\lambda}{NA} \tag{2.7}$$

Equation 2.7 clearly shows the inverse relation of the minimum resolvable distance and

the numerical aperture previously discussed. Rayleigh's criterion is based on the image collected from two point sources having the Airy disk of one on the first minimum of the other. The Airy disk pattern collected at the image plane is due to the diffraction of light and thus cannot be avoided. This criterion effectively requires roughly a 26 % decrease in intensity between the two peaks of the collected image. In confocal microscopes, due to the presence of the pinhole, this criterion results in a minimum resolvable distance two points in the object plane as [108]:

$$\Delta r_{confocal} = 0.88\lambda f/\# = 0.44\frac{\lambda}{NA} \tag{2.8}$$

Thus, comparison of Eqs. 2.7 and 2.8 clearly shows the improved lateral resolution of confocal over conventional microscopes. This increase in resolution can be attributed to the reduction of the side lobes of the airy disk of the confocal microscope compared to conventional [108]. The reduction of the side lobes allows for dim objects near brighter object to still be resolved that would be otherwise washed out by the side lobes in the point spread function of a conventional microscope.

Depth of field given by Eq. 2.2 can be used as a metric for the axial resolution but strictly speaking it is not a resolution. A working definition of axial resolution similar to the Rayleigh criterion for lateral is a more appropriate metric. As in the lateral Rayleigh criterion, a 26% dip in intensity for two point sources located Δz apart is given by [108]:

$$\Delta z = 1.5\frac{n\lambda}{NA^2} \tag{2.9}$$

Equation 2.9 shows the increase in axial resolution over conventional microscope given by Eq. 2.2 that uses Z as the total thickness in focus which would be Z=2Δz in the notation in Eq. 2.9. The selection of the pinhole diameter used in CLSM also has an impact on the maximum resolution that can be obtained by an objective. The image of the pinhole on the specimen determines the area of the specimen that will be illuminated. A pinhole that is

smaller than minimum resolvable distance (given by Eq. 2.8) will not improve resolution, but it would only decrease the signal-to-noise ratio. However, a pinhole that is too large will accept light that is scattered from a larger depth (or axial distance) into the specimen blurring the acquired image. From these considerations, the pinhole must be optimized for the particular objective being used.

In a typical CLSM, galvanometer mirrors are used to deflect the laser beam and the image is built up pixel by pixel using a photomultiplier tube (PMT). When there is significant depth to the specimen or when conduction optical sectioning, multiple images are captured to obtain each axial slice of the specimen. This is achieved by moving the objective very precise amounts to obtain each axial slice. This movement of the objective is extremely critical for calculating three dimensional renderings of the sample and is discussed later. Each image 'slice' represents the depth into the specimen and where features in the specimen are absent at that depth, there will not be any photons incident on the PMT due to the blocking from the pinhole. Axial sectioning of the specimen can be obtained by simply considering one image from a particular depth into the specimen. When the overall image of the specimen is desired, each of these image slices is then combined digitally by considering each pixel location independently. An algorithm is implemented at each pixel location such that the greatest digital count at that location is extracted from the slices and used as the digital count in the final composition image. This process is repeated for each pixel location and thus an apparent infinite depth of field (limited by the working distance of the lens) is achieved.

The apparent infinite depth of field is limited by the working distance of the objective because if there were features in the specimen that were deeper into the specimen than the working distance of the objective, the objective would not be physically able to get close enough to get those features in focus. The process of taking multiple image slices and compiling each in-focus image into one image with overall focus can be implemented in conventional digital microscopes using digital image processing to make decisions on

which slice contains the 'in-focus' pixel. This process of relying on image processing is rather limited and has a large variation of success depending on the specimen, unlike confocal systems were the pinhole physical constrains the light is specimen independent. It is also worth mentioning that each of the images captured are in grayscale and not in color as obtained by conventional microscopes.

Three dimensional image rendering can be obtained using the relative location of the objective lens for each image slice. By moving the objective in very small amounts between each image slice different pixels will have different digital counts dependent on whether there is a feature in specimen at that three dimensional location. The digital count will reach a maximum value at the objective location corresponding to the depth at which that feature is in optimal focus.

One of the major advantages of CLSM is the blocking of scattered light that is not in focus. Light that is scattered from a volume that is not in focus cannot pass through the pinhole that would otherwise blur the image and decrease contrast. This is apparent for specimens that have a relatively large range in depth and can be clearly observed in imaging of PEMFC GDL materials. Figure 2.3 exemplifies the difference between conventional and confocal laser microscopes while imaging a GDL. In Fig. 2.3(a), only a small portion of the GDL's fibers can be seen and the rest of the image is out of focus due to the limited depth of field of the objective. This same area of the GDL is drastically different when imaged with a CLSM as shown in Fig. 2.3(b). The improved image spatial resolution and contrast as well as the apparent infinite depth of field in the CLSM image clearly show the advantage of a CLSM over a conventional microscope. Since the CLSM takes a series of images at a sequence of depths and then composes all of the measured digital counts into one image, an apparent infinite depth of field was achieved.

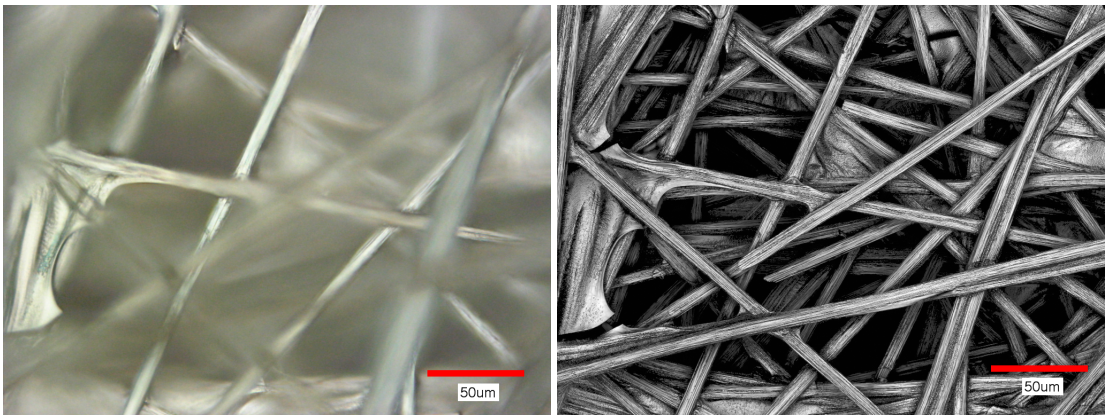

(a) Conventional microscope image of a GDL (b) Confocal laser scanning microscope image of a GDL

Figure 2.3: Conventional versus laser confocal microscope images of a GDL material. Note the increase in the depth of field and contrast in the CLSM image.

2.2.2 Infrared

Infrared is a general classification of electromagnetic (EM) radiation ranging in wavelengths from roughly 780 nm up to 1 mm. This regime of the electromagnetic spectrum can be further divided into near infrared (0.7 μm $\leq \lambda \leq$ 1.0 μ m), short-wave infrared (1.0 μm $\leq \lambda \leq$ 3.0 μm), mid-wave infrared (3.0 μm $\leq \lambda \leq$ 5.0 μm), long-wave infrared (7.0 μm $\leq \lambda \leq$ 14.0 μm), and very-long wave infrared (15.0 μm $\leq \lambda \leq$ 100 μm). Each of these bands can reveal different information and detectors are generally designed to detect in one of these ranges. Imaging system designed for these bands of the EM spectrum are analogous to visible systems with the exception of materials (sensor and optics). External infrared light sources are not necessary and are generally not used. Any object above absolute zero will emit EM radiation in the infrared and thus the emitted light is measured along with any reflected infrared light from the surroundings. Temperature measurements can be obtained through system calibration or with sufficient knowledge of each element of the system. Emissivity, reflected temperature of the surroundings, distance to the specimen, and external optics all have to be considered for accurate temperature measurements. In addition to temperature measurements, contrast between objects can be obtained from

differences in geometry as well as emissivity.

Infrared transparent PEMFC are similar to those used in visible with the exception of the window material selection. Transmission spectra have to be considered to ensure that the band of light to be detected will pass through the window in nearly equal amounts. Not meeting this criterion will result in a distorted image or no image at all. Many studies have used infrared windows such as sapphire, ZnSe, CaF_2, ZnS, MgF_2 which are transparent in the both visible and mid-wave infrared. Silicon can also be used for a mid-wave infrared window but does not transmit visible wavelengths. Infrared is generally used to obtain temperature information but different materials at the same temperature can also be differentiated in infrared images.

Digital infrared cameras are not as a mature technology as digital visible responsive cameras due to customer demand and availability of high quality raw materials. Large focal plane arrays are generally not available for infrared sensors, where they are readily available for visible light sensors. Even with equivalent sensors and optics, the theoretical spatial resolution for infrared imaging is somewhat lower than visible as per Eq. 2.7.

Imaging in the infrared spectrum for PEMFC research has typically been used to obtain temperature distributions [109–115] and some have extended the use of infrared photons to measuring water content based on absorption [116–118] but the technique is not limited to temperature measurements. Infrared imaging can measure the optical properties of the specimens similar to visible imaging except that it measures lower energy IR photons. Infrared photons can be used to identify objects in the scene based on reflection, absorption, transmission, and emission contrast. The image in Fig. 2.4 is an example image captured in mid-wave infrared of a GDL surface with water present. The grayscale bar is in degrees Celsius and the temperature measurements were calculated assuming a uniform emissivity of 0.95. The GDL and water were both at room temperature but due to differences in emissivity and geometry to the two isothermal materials are clearly differentiated.

Hakenjos et al. [109] simultaneously imaged the cathode channels and temperature

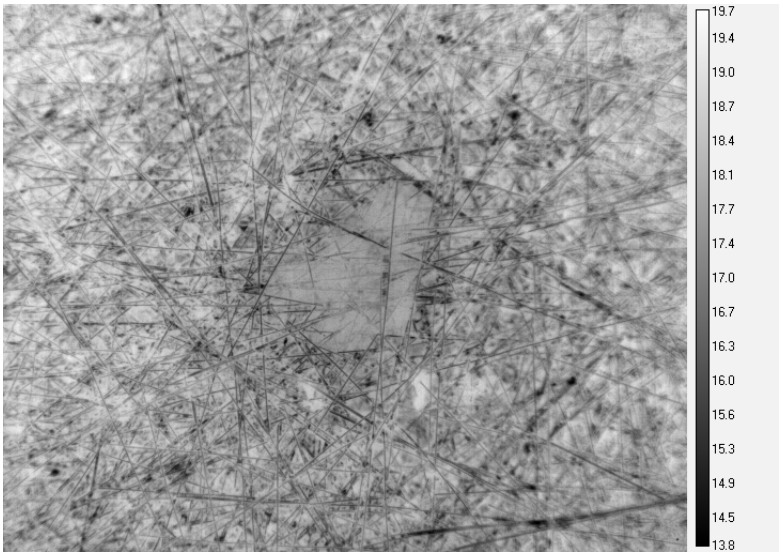

Figure 2.4: Infrared image of water on a GDL material at ambient temperature. Temperature measurements assume uniform emissivity of 0.95 and scale is in degrees Celsius.

distributions while sampling the current distribution in a PEMFC. Visible and long-wave infrared imaging were accomplished through the use of a ZnSe observation window which is fairly transparent for visible and long-wave infrared. The authors reported a minimum error in temperature measurements of less than 0.3°C. It was found that areas of high current density have higher temperature due to the heat released from the reaction.

Ishikawa et al. [110] studied water formation on the cathode CL below 0°C simultaneously in visible and infrared spectra. An interesting experimental setup was constructed utilizing a cold mirror which transmits the infrared and reflects the visible radiation transmitted through a sapphire window. The cold mirror was placed at 45° relative to the GDL through-plane direction which allowed for imaging of the same field of view in both imaging modalities. A gold mesh was used as the cathode GDL and allowed for direct observation on the catalyst layer. The infrared imaging system was able to measure water temperature through the sapphire window to within 1C. The authors observed that liquid water traveled through the catalyst layer under subzero cell conditions. The water droplets that formed and grew on the CL were in a super-cooled state. When the super-cooled state

was broken, the droplets' temperature increased to 0°C and the droplets froze. The heat of solidification was observed by the infrared camera at the moment when the super-cooled state was broken and the droplet froze.

Ishikawa et al. [111] investigated water dynamics in the cross section of a cathode GDL under cold start conditions of -10°C. Simultaneous visible and infrared imaging were conducted on the fuel cell through a sapphire window at the end of a gas channel. The spectral response of infrared camera used was not given but quoted as to having 10 μm spatial, 1/30 s temporal, and $\pm$1°C temperature resolutions. It was observed that when a purge of dry gas was not implemented; ice formation at the GDL/MEA interface formed and blocked gas transport. The maximum current density that was achieved without an initial purge was 0.15 A/cm^2 due to ice formation along the GDL/MEA interface. When a purge of dry gas was implemented prior to running the cell, super-cooled water was observed to form and travel through the GDL to the channel. The super-cooled water formed a droplet on the surface of the GDL. Super-cooled water at the GDL/MEA interface was observed to freeze after 268.5 s but the droplet on the GDL surface remained super-cooled until 378.0 s when it froze. Heat of solidification was captured at the time that the super-cooled water froze at the GDL/MEA interface and was observed to spread along the interface. This study showed that an initial purge prior to start-up super-cooled conditions can allow for liquid water transport through the GDL.

Shimoi et al. [112] conducted a thermal imaging study for which they measured the temperature of the GDL along the gas channels. According to the authors, the temperature difference between the GDL and MEA should be very small, which suggests that the temperature measured for the GDL was considered to be the same as the MEA. A Thermotracer TH5104 with spectral response in the mid-wave infrared was used for the infrared measurements. For the experimental setup the temperature measurements were estimated to be within $\pm$2-3°C. It was verified that higher average current densities have a greater overall temperature along the membrane. Hot spots were observed initially near the inlet.

These hot spots could lead to localized temperatures that exceed the limit that the MEA can withstand without signification degradation. The localized hot spots near the inlet were found to cancel on each electrode for a counter flow configuration using low (42 % RH) humidified H_2 gas to yield a uniform MEA temperature.

Son et al. [113] studied deactivation of an improved catalyst (Pt/γ-Al_2O_3) by using long-wave infrared temperature measurements of a catalyst layer. A catalyst bed was sandwiched by two layers of glass wool and enclosed in a quartz tube reactor. Thermocouples were positioned inside the reactor to measure the inlet and outlet gases. The thermocouples were also used in conjunction with an infrared camera to obtain the effective emissivity of the reactor. The infrared camera used had a temperature precision of ± 2 %. Temperature distribution along the reactor was obtained and analyzed as a function of input gases. The temperature measurements gave insights into the deactivation of the catalyst due to CO poisoning.

2.2.3 Fluorescence

Fluorescence microscopy utilizes the phenomenon of fluorescence to observe specimens opposed to using the reflected light used in conventional microscopy. Fluorescent dye is added to a water reservoir in small concentration as to not change the bulk properties. The specimen is illuminated with light in the spectral band that is specific to the dye added. The fluorescent dye will absorb this narrow band of photons, dissipate some of the absorbed energy, and emit a narrow band of photons of a longer wavelength. The emitted light can then be collected by an appropriate imaging system responsive to the energy of the emitted photons which are typically in the visible range. A narrow band source, such as a laser, is used to illuminate the specimen and filters are used to collect only the narrow band emission. Spatial resolutions are theoretically equivalent to reflection microscopy but temporal resolutions could be significantly reduced if the excitation illumination scans the specimen. Ex situ experiments have been conducted to use fluorescence microscopy for PEMFC water

management research. One advantage of this technique compared to conventional reflection microscopy is that the location of water can be precisely determined. In conventional reflection microscopy, the location of water on the specimen can be uncertain due to the intrinsic transparency of water. In fluorescence, water is the source of the collected light and thus the location can be determined directly from the image. Imaging the specimen using filters centered about the emission wavelength differentiates the dye (in turn the water) from the rest of the specimen. Application to GDL in situ experiments would require novel methods to be used in the design of the experimental setup.

The utilization of fluorescence has enabled a variety of water transport studies that are significantly improved or even impossible with conventional reflection microscopy including water transport through the GDL [119–122], channel-GDL interaction [119], water film thickness in channels [123], GDL internal wettability [124, 125] and water content within the membrane [126–128].

Litster et al. [122] developed the novel technique of using fluorescent microscopy to capture water transport in a GDL. Fluorescein was added in small amounts to a water reservoir such that the properties of water remained unchanged and yet still obtained a fairly strong emission signal. Water was supplied by a syringe pump from under the GDL sample that was held in place by the test section. A blue light source was incident on the GDL as the water traversed from below. The fluorescent dye absorbed the blue photons, dissipated some of the photon energy, and emitted photons at a longer wavelength ($\lambda \approx 510$ nm) than the absorbed photons. Images of the water solution as it traversed the GDL sample were captured at 4 fps with a pixel resolution of 5.35 μm. The intensity of the light captured from the Fluorescein was correlated to the height of the solution. With the correlated height measurements, 3D renderings were created. They used the computed 3D images to reveal more information about water transport through the GDL. A contour plot of the height of the water was computed and used to analyze adjacent paths that the water took to reach the surface. A temporal plot of each water path revealed that the paths are interconnected

within the GDL. A velocity contour plot further validated this claim by showing that when one path began to rise, an adjacent path was observed to be receding. It was found that the method of transport in the GDL was dominated by fingering and channeling rather than the previously thought 'upside-down tree' capillary network.

Bazylak et al. [120] utilized fluorescence microscopy to study the effect of compression on ex situ water transport in a GDL. The fluorescent dye, Fluorescein, was added in a small amount to a water reservoir. Fluorescein has a maximum absorbance and emission at 490 nm and 513 nm respectively. The addition of the fluorescent dye in such a low concentration (83 ppm) had negligible effects on the water properties. A blue light source was used to provide the absorption wavelengths and any wavelength shorter than that of the fluorescent dye's emission was filtered out. The emitted light was captured using a digital visible microscope (Leica Microsystems DML) using a 1.25x objective to provide a field of view that included compression regions of the GDL. The GDL was placed between a Plexiglas plate and an O-ring to supply the compression. The water solution reservoir was placed underneath the O-ring and fed from a syringe pump. The Plexiglas plate had a 2mm hole to allow space for the water after reaching the surface of the GDL. The height of the fluid was correlated to the light intensity captured by the relation proposed by Litster et al. [122]. Together with the calculated height, the 2D images were used to construct 3D images of the water traversing the top layer of the GDL. The authors also correlated their images to pressure measurements during the experiments. It was found that there is a breakthrough pressure needed for the water to traverse the GDL to the surface and it was found to be in the range of 4.8-5.8 kPa for their trials. It was also found that areas that were compressed became preferential areas for water breakthrough, contrary to what was expected. The areas under compression were thought to have small pore radii and thus prohibit water transport. Scanning electron microscope (SEM) morphology study was also conducted to understand this phenomenon and revealed that the compression caused PTFE coating to break and produced more hydrophilic areas that favored water transport.

Bazylak et al. [119] conducted a study of droplet formation and detachment from the surface of a GDL into a gas channel using fluorescence microscopy. Fluorescein dye was used in low concentration in a water reservoir as to not modify the properties of water. The solution was injected from one side of a GDL and emerged on the other in a gas channel made of polydimethylsiloxane (PDMS). PDMS has a contact angle of 78° which is similar to graphite (70-80°) used in typical PEMFCs. A 5x objective was used and the images were captured at a rate of 9.3 fps with a pixel binning of 4 x 4. The imaging system had a spatial resolution of 8.14 μm/pixel. It was found that the droplet diameter at detachment (in the absence of pinning) is constant for a given air flow rate. For a water flow rate of 5 μm/min and air velocity of 2 m/s, the detachment diameter was 2.4 mm.

Esposito et al. [129] used fluorescence imaging technique to study the oscillations and removal of water droplets in an ex situ air flow channel. The authors used digital video processing to determine the dominate frequencies of vertical and horizontal oscillations. It was found that the droplet oscillation frequency does not depend upon air velocity and is only dependent on droplet size. Fishman et al. [130] used fluorescence imaging to reveal the unpinning of microdroplets on GDL materials and related the phenomenon to GDL surface topography.

2.2.4 X-ray

X-ray photons have much shorter wavelengths than infrared or visible, roughly in the range of 0.01 nm$\leq \lambda \leq$ 10 nm. X-ray wavelengths are so short they are generally referred to by their energies which range from 120 eV to 120 keV. X-rays are so highly energetic that they interact with matter more like particles than waves. X-ray imaging systems can use beam attenuation or diffraction to obtain information about the specimen. X-rays are more likely to be attenuated by more dense (due to density or atomic number) than less dense materials. This is due to the density of the electron cloud of the atoms and molecules that the incident photons interact with.

A difference in X-ray absorption results in useful contrast in the image that can be used to differentiate objects in the specimen. Three-dimensional images can be rendered using CT by compiling multiple two-dimensional images or 'slices' into one three-dimensional image. X-ray diffraction (XRD) is routinely used to reveal the crystal structure of materials but also can be used to reveal the hydration state of a proton exchange membrane (PEM) in an operating fuel cell. X-ray images are typically captured through the use of scintillator that converts the X-ray photons into visible light which is then captured with a digital camera. Hence, the transfer function of the scintillator must be taken into account when characterizing the imaging system. Due to the extreme difficulties in focusing X-rays, materials are not readily available (if at all) for use as X-ray lenses as there are for visible or infrared light. As a result, achieving the limiting spatial resolution governed by Eq. 2.7 has been very difficult. Therefore, the maximum resolution will be limited by the scintillator's resolution.

X-ray imaging systems can reveal details of fuel cell materials that cannot be obtained from other imaging techniques. The high energies of X-ray photons enables imaging through GDL material to measure a two-dimensional image (shadow image). Other optical imaging techniques cannot traverse the GDL due to low transmission of lower energy photons. X-ray microtomography can reveal the three-dimensional structure that is essential in understanding water transport. X-rays are greatly attenuated by metals which require significant modification to fuel cell hardware to allow for the beam to pass through the cell materials.

X-ray imaging techniques are being pursued as an additional imaging modality for PEMFC research. X-ray attenuation of synchrotron [131–137] and non-synchrotron [138–141] sources have shown potential to be valuable techniques for water management studies of PEMFCs.

Albertini et al. [131] showed the feasibility of using X-ray diffraction (XRD) of a synchrotron source to measure the hydration state of a Nafion membrane. The study was con-

ducted using the high-energy 87 keV X-ray beam at ID15 line of the European Synchrotron Radiation Facility (ESRF) in Grenoble. This was the first study of in situ time-dependent water content in a Nafion-like membrane fuel cell. A special test section was developed to avoid using the usual PEMFC materials that absorb X-rays and distort the diffraction pattern. A Nafion membrane was restored to its original H^+ form and placed between two Toray carbon papers and the whole assembly was enclosed by two Teflon cylinders. The XRD pattern of dry the membrane was used as reference for comparison to the XRD pattern of a hydrated membrane. A hydrated membrane was imaged as it reached equilibrium with the ambient relative humidity. The hydrated membrane's XRD pattern showed localized deviation from the dry sample. By measuring the difference between these localized deviations, relative hydration measurements were obtained as a function of time.

Lee et al. [138] showed the feasibility of an X-ray imaging system to measure water thickness from the attenuation of a conventional X-ray source. Using an X-ray tube and X-ray camera they found that attenuation due to iopamidol increased linearly with thickness. The attenuation was also able to clearly show contrast between water and GDL materials.

Manke et al. [134] visualized water in a PEMFC utilizing a synchrotron X-ray source at the tomography facility of the BAMline at the Synchrotron BESSY in Berlin. The cell had 8mm holes drilled into the endplates to allow for the transmission of X-rays through the cell. The imaging system used was capable of achieving 3-7 μm spatial resolution using a Princeton VersArray 2048B camera. As in neutron radiographs, each image obtained was normalized by an image of the dry cell to observe the presence of water under operation. The amount of water was quantified by using the attenuation coefficient of the transmitted X-rays. Water was observed to accumulate and discharge from pores in an 'eruptive transport' in a cyclic fashion. This eruptive transport was described as many droplets emerging from the GDL into the channel and forming a single droplet in less than 5 s. The evacuated pores began to fill up again and the process was repeated with a constant frequency. There were also areas where the amount of water was fairly constant which indicated that the

water was in a state of continuous flow.

Sinha et al. [139] used X-ray microtomography to quantify liquid water content in a PEMFC using beam attenuation. The sample was rotated in the X-ray system to obtain 15 2D projections or slices of the sample that were used to construct 3D images of the sample. A dry 3D image of the sample was obtained in this manner. To fully saturate the GDL with water a vacuum was applied to the top of the sample and water was supplied at the bottom. With the GDL saturated, CT was implemented to create a 3D image of the 'wet' sample. Each voxel of the dry and wet samples were used for each voxel of the images obtained during purge to calculate the liquid water saturation at each voxel location. After the cell was saturated, it was purged by applying N_2 at room temperature at 5 L/min. During purge, the 15 slices were obtained periodically to map the water transport. The amount of water removed from the cell was determined to decrease exponentially with purge time. It was also found that very little water was removed from the GDL after 6 min of purge time at room temperature.

2.2.5 MRI

Magnetic resonance imaging (MRI) utilizes the nuclear magnetic resonance (NMR) of the particles (usually protons) to locate their position within a specimen. A strong static magnetic field (1-14 T) aligns the spin of the particles along the axis of the applied field. There are two possible orientations for the spins which slightly differ in energy. A secondary field oscillating at radio frequencies with energy equal to the difference between to spin states will be absorbed and excite the lower energy spin states into the more energetic state. As the excited spin states decay back into the ground state, they emit photons with energy equal to the energy difference between the two states. A gradient in the static magnetic field is used to differentiate the location of the spin states along the field. The emitted photons are measured and used to calculate the location of the spin states. MRI applied to PEMFC research requires significant modifications to the fuel cell. Ferromagnetic materi-

als cannot be used for MRI due to the strong magnetic field used. Even materials with high conductively must be used sparingly to mitigate noise in the NMR signal.

Measurement of water within PEMFCs using MRI has been proven as a viable method with significant necessary modification of the conventional materials [142–154]. Through-plane studies utilizing MRI techniques have recently been successful in resolving water content in relatively thick PEMs that would not currently be possible using typical membranes ($\leq$ 50 μm) due to spatial resolution limitations. These studies have investigated water distribution in the through-plane direction of PEMs and catalyst coated membranes (CCMs) in an ex situ environment [155] using a relatively thick membrane (254 μm) and has also been applied to in situ experiments using a somewhat thinner (178 μm) membrane [156]. Spatial and temporal resolutions are much lower than the other imaging techniques presented but further research is improving the spatial and temporal resolutions.

Feindel et al. [145] were the first to use NMR imaging to obtain in-plane water distribution in an operating PEMFC. The NMR imaging system used had a 7.05 T superconducting magnet. The system was able to capture at the pixel resolution of 234 x2 34 μm with an acquisition time of 128 s. An initial image of the specially designed fuel cell was captured and used as a comparison for different operating conditions. It was found that high cathode gas velocities (50 mL/min) removed the water from channel but resulted in membrane dehydration. Reducing the cathode flow rate increased the water content in the PEM and water accumulated back into the channel. Counter-flow configuration produced a fairly uniform hydration state for the PEM whereas co-flow resulted in dehydration near the inlets. This was the first study where NMR was used to capture the water distribution in an operating PEMFC and proved that NMR can be successfully applied to PEMFC research.

Dunbar and Masel [143] obtained the first 3D quantitative images of the water distribution in an operating PEMFC utilizing MRI. The MRI imaging system used a 14.1T magnet and the flow fields were constructed out of Teflon because convectional magnetically conductive graphite cannot be used in the high magnetic field of a MRI machine. The small

active area (1cm^2) of the cell allowed the use of solid gold current collectors which added minimal noise to the signal. To quantify the amount of water present in the fuel cell, three small glass capillaries with internal diameters of 0.9 mm were added to the cell oriented in each dimension. The capillaries were filled with pure water and were used for calibration. By measuring the received signal from these capillaries with known volumes, the signal from the rest of the cell can be correlated to actual water content. Their voxel size was 138 x 138 x 200 μm where the 200 μm was in the thickness direction. The temporal resolution of the MRI machine was determined by the acquisition time of 4 min 19 s to complete the sequence. Due to the magnetically inductive nature of carbon, no signal can be obtained from the carbon cloth used as the GDL. The authors found that water transport in the channels exhibited a slip and stick behavior in the form of waves. Under no cell conditions tested did they observe slug flow and only wavy-stratified flow was observed. Dry hydrogen was used to determine the dominant phenomenon controlling water transport on the anode of the cell. Under low current density (200 mA/cm^2) water was observed in the anode flow channels. This implies that back diffusion and capillary back pressure were dominant over electro-osmotic drag. This was further confirmed by examining the water concentration in the anode inlet and outlet.

Dunbar and Masel [144] improved upon their previous MRI study [143] of PEMFCs to better resemble commercial PEMFCs. A graphite layer (Aquadag) was painted on the flow fields used in their previous study to resemble the flow fields of a commercial PEMFC. Under various operating conditions, similar images were obtained with 138 x 138 x 200 μm voxel size and 4 min 19 s acquisition time. The water flow in the channels exhibited the same behavior of stick and slip wavy-stratified flow previously observed. The flow fields were examined in fine detail utilizing a visible light image. They found small defects in the channels that corresponded to areas where the flow could get stuck. It is possible that these defects could be the cause of the stick/ slip method of flow in the channel but it was not conclusive from the study. The observation that back diffusion and back pressure

are dominant over electro-osmotic drag for low current densities (200 mA/cm^2) was made for the graphite coated channels. It was also observed that at high current densities (500 mA/cm^2) there was no water measured in the anode. Thus, at high current densities electro-osmotic drag dominates over back diffusion and back pressure.

2.2.6 Neutron

Nuclear interactions are employed in neutron radiography to obtain image contrast. Unlike photons, neutrons strongly interact with the nuclei of atoms rather than electron cloud interactions of the former. However, neutron radiography systems are similar to X-ray radiographs and complimentary in the information gathered due to the atomic number dependence of attenuation. Neutrons are emitted from a source and collimated into a beam. The collimated beam is then incident on the specimen and the remaining unattenuated neutrons encounter a neutron sensitive scintillator which converts the neutrons into photons. These photons are then measured by a visibly responsive sensor. A typical camera would be damaged by the neutron beam so a mirror is used to reflect the photons perpendicular to the neutron beam such that the camera is not in the neutron path. Neutron attenuation is generally greater for low atomic number than for high atomic number elements and thus contrast can be achieved in the collected image.

The attenuation due to hydrogen nuclei is quite high compared to carbon, copper, and other commonly used fuel cell materials. This makes neutron imaging an ideal modality for water management studies for PEMFC research because water content can be measured without modification to the cell. Through calibration the amount of beam attenuation can be related to water thickness along the beam path. This is usually accomplished by taking a 'dry' image of the cell to measure the beam attenuation due to fuel cell components and hardware without water present. This 'dry' image is used as a reference image and each image collected during testing is normalized by it. The resulting processed image is then a measurement of the attenuation due to the presence of water.

Neutron imaging systems are very expensive and there are just a few locations with high neutron fluence sources [64]. However, neutron imaging systems have unparalleled ability to measure water content without having to modify the fuel cell. Spatial and temporal resolutions are significantly less than the optical techniques previously described. A major limiting factor in spatial and temporal resolutions is the beam divergence. The ratio of the distance from the aperture of the collimator to the specimen, L, to the diameter of the aperture, D, can be used to characterize the divergence. A low L/D ratio results in blurring of the image but a high L/D requires a longer exposure time. This ratio must be optimized for the particular source-collimator system [157].

There have been many PEMFC studies that have utilized neutron radiography to detect the water distribution in the in-plane direction of the fuel cell materials for which the neutron beam is perpendicular to the face of the membrane [158–180]. The spatial resolution required to obtain the in-plane distribution is not as critical as when acquiring the through-plane water distribution where the neutron beam is parallel to the face of the membrane, simply due to thicknesses of commonly used fuel cell materials. Recently, high resolution neutron imaging has been applied to resolve the through-plane water distribution that is capable of distinguishing the anode versus the cathode water accumulation [157, 181–184].

Bellows et al. [185] used neutron radiography to conduct the first differential water gradient across a Nafion membrane. A thick (500 μm) membrane was made by thermally bonding four layers of Nafion 117 and used in their study. The thicker membrane provided the necessary data points for water gradient measurements. The authors were able to obtain a dynamic range of 100 between wet and dry membrane conditions and thus validated that neutron radiography can provide sufficient data for water content analysis in an in situ experiment. Chen et al. [159] were able to distinguish four types of areas through fuel cell design and use of digital image masks to isolate them in the neutron images. They imaged in the through-plane direction to obtain the in-plane water distribution with a neutron imaging system. The anode and cathode channels were shifted by one channel

width to enabled through- plane observation of anode channel-rib (land), cathode channel-rib, anode channel- cathode-channel, and anode rib-cathode-rib areas. These areas were isolated in the resulting digital images by using image masks. The image masks digitally isolated these locations by changing the pixel values of areas outside of the area of interest to zero (black) leaving the area of interest unaltered.

Hickner et al. [181] were able to obtain high resolution neutron images of the through-plane water distribution of the center of a 2.1 x 7.7 cm active area cell. Neutron sensitive microchannel plates (MCP) were used to collect and quantify water content. MCP used in their study had pixel resolution of 16.4 x 16.4 μm which enabled differentiation of the cathode and anode as well as the membrane. It was found that at moderate current densities (near 0.75 and 1.00 A/cm^2) water accumulation could not break through the MPL and resulted in a portion of the product water being forced through the membrane to the anode.

Owejan et al. [169] used a scintillator and CCD camera system to record neutron radiographs of an operating 50cm^2 PEMFC. It was found that less water was retained in triangular channels than rectangular. GDLs with lower in-plane gas permeability also were found to retain less water. An unexpected result of the study was the fact that gravity had a significant effect on water accumulation in the gas distribution channels.

The imaging studies used to date to study water transport in PEMFC have been successful in providing an abundance of information on water behavior throughout the fuel cell layers and are at various stages of development. Each imaging modality has proven to be successful in studying water management and have provided unique visualization of water in PEMFCs. The success thus far of these techniques and desire for improved resolution (spatial, temporal, water thickness, etc.) provides sufficient motivation for each modality to continue to be pursued in parallel. Visible and neutron imaging will remain as the two most valuable imaging modalities for water management studies as the result of high spatial and temporal resolutions and ability to measure water thickness without cell modification, respectively. Infrared and fluorescence microscopy will continue to provide valuable fuel cell

temperature distributions and microscopic water transport phenomena. X-ray and MRI will continue to be developed to improve resolutions and reduce the modifications to standard fuel cell materials for in situ studies. Imaging techniques have proven to be invaluable tools in the quest for a complete understanding of water management phenomena in PEMFCs. A comprehensive model describing water transport (and hold-up) from the cathode CL, through the MPL and GDL, and into the gas distribution channels will provide fuel cell engineers with an invaluable tool for PEMFC material optimization.

2.3 GDL Liquid Transport

Liquid water transport from the cathode catalysts layer through the MPL (if present) and the GDL into the channels is an area of intense research as discussed in section 1.2. The transport of liquid water through a GDL is a drainage process in which water, as a non-wetting fluid, displaces the wetting fluid, air. The drainage process in porous media is commonly characterized by two non-dimensional numbers, the capillary number and viscosity ratio (M=μ_{nw}/μ_w) of the fluids. The capillary number is defined as:

$$Ca = \frac{u\mu_{nw}}{\sigma} \tag{2.10}$$

where u, μ_{nw}, and σ are the velocity, viscosity, and surface tension of the non-wetting fluid. When water is injected to a porous media at low a constant flow rate the viscous force is negligible and the displacement will be dominated by capillary forces. At normal PEMFC operating conditions the capillary number is in the range of 10^{-8}-10^{-5} and the viscosity ratio is M=μ_{water}/μ_{air} = 17.5 which results in capillary driven flow [27, 186]. One of the critical constitutive relationships for describing capillary flow in a porous material is capillary pressure versus liquid water saturation (P_c vs. S_w). This has been the focus of several recent investigations [187–189]. A permanent capillary pressure hysteresis between liquid water injection and withdrawal has generally been observed. Gostick et al. [188] accounted

for the capillary hysteresis in terms of the contact angle hysteresis and the pore geometric effects. It should be noted that all these works measured the GDL saturation up to 1, which may be correlated to the GDL under the ribs where the drainage of water is restricted and water remains confined in the GDL. However, for the GDL under the channels, water drainage is quite different because water in this area can be easily removed in the form of droplets and films as well as slugs causing a lower saturation in the GDL. Because of this fact, the GDL saturation in an operating fuel cell is non-uniformly distributed [133, 190].

The dynamics of the liquid water transport through a GDL is also of interest to understand the resistance of reactant gas transport due to water accumulation. However, this has been barely studied until recently due to the difficulties of observing water transport phenomena inside the GDLs. Nam et al. [191] and Nam and Kaviany [192] observed vapor condensation and liquid breakthrough in a GDL using an environmental scanning electron microscope, and proposed a tree-like transport mechanism in which microdroplets condensed from vapor agglomerate to form macrodroplets which eventually flow preferentially toward larger pores and breakthrough. However, this method is not possible to simulate fuel cell operating conditions due to the vacuum requirements. Pasaogullari and Wang [193] also hypothesized a tree-like water transport behavior in GDLs in their two-phase flow model. Lister et al. [122] visualized liquid water flow as it emerged from the surface and a few micrometers below the surface of a GDL using a fluorescence microscope. They observed that water emerges from preferential pathways and suggested a "fingering and channeling" mechanism for water transport in GDL pores. Bazylak et al. [120] found that the preferential water pathways coincided with the compression areas in the GDL, which they accounted for by a loss of GDL hydrophobicity due to the fiber breakup and PTFE coating deterioration caused by compression. In a later study, Bazylak et al. [119] observed the dynamic changes in breakthrough locations for water transport through a GDL and explained it using a dynamic and interconnected network of water pathways within the GDL. Gao et al.s [121] confocal microscope visualization revealed an unstable "column

flow" in GDLs, which is similar to Lister et al.s fingering model [122], except that wider flow paths spanning several pores are observed. Manke et al. [134, 167] and Hartnig et al. [132] investigated the in situ liquid water evolution and transport in an operating fuel cell with synchrotron X-ray radiography. They observed an "eruptive transport" mechanism in GDL pores near the channels, which they describe as the quick ejection of droplets from the GDL into the gas channels. However, water fills continuously in the GDL pores under the central land following a capillary tree-like process [192,193]. Both the ex situ and in situ experiments have clearly demonstrated that there exist fast "water transport channels" within a GDL and that the water transport and breakthrough are dynamic processes. However, the morphology of transport channels and the dynamics of water transport in these channels need further investigation.

Theoretical treatment of water transport in a GDL has been the focus of several models. A large number of works are based on the continuum two-phase flow model [26, 192–195], which describes the flow and transport on the basis of Darcys law. Unfortunately, GDL-specific experimental data on many of the necessary relationships and parameters, such as the water saturation dependent relative permeability, effective diffusivity, and air-water capillary pressure, are scarce, making the application of these models to GDL materials questionable. As an alternative approach, a pore-network model, which has a long history in the study of porous media like soils and rocks [196], has recently been used in modeling water transport in GDL materials [19, 23, 24, 27]. The pore-network model maps a complex pore space continuum onto a regular network of pore bodies interconnect by throats. Several works have shown that invasion-percolation process, which is a strongly capillary-driven process at the limiting case of zero fluid velocity, may be an important mechanism for water transport in GDL. However, most of the pore-network models [19, 24] focus on the numerical determination of the macroscopic two-phase properties, such as the capillary pressure versus saturation correlation (P_c-S_w curve) and the relative phase permeability as a function of S_w, and little work has been done to clearly understand the mechanism of

water transport through a GDL.

The presence of a MPL on GDLs has been shown to improve the fuel cell performance, but the roles of (or mechanisms within) MPL are not clearly understood. It has been postulated that MPL improves the fuel cell water management and mass transport, e.g., avoiding fast dry-out of the PEM at low current densities and electrode flooding at high current densities. Several authors [197,198] have demonstrated that the MPL improves the humidification of the membrane at the anode side. Jordan et al. [198] and Kong et al. [199] concluded that the MPL enhances oxygen diffusion by reducing flooding in the cathode. The critical role of MPL in reducing flooding is a result of the modification of the pore structure (e.g., porosity, pore size distribution, hydrophobicity, and nonuniformity) of GDL, has received wider acceptance in many recent studies [200–203]. Weber and Newmann [204] and Lin and Nguyen [205] explained the function of MPL in reducing the cathode flooding as a capillary barrier, which prevents water from entering the cathode GDL and forces water to permeate from cathode to anode. However, recent experimental studies show that MPL does not significantly influence the water back-diffusion rate [206, 207]. Alternatively, the role of MPL in control of water distribution has been proposed in the theoretical treatment of water saturation distribution in multi-layer electrodes [191, 192]. The authors suggest that the MPL reduces the water saturation in GDL near the catalyst layer and therefore improves the cell performance. In this way, the MPL enhances the cathode water transport rather than hindering it. Gostick et al. [208] measured the water saturation and associated capillary pressure at the point of water breakthrough in GDL samples with and without MPL. Their data demonstrated that the GDL saturation at water breakthrough is drastically reduced in the presence of MPL, suggesting that an MPL restricts the number of points of entry of water into the GDL. However, pore scale phenomena associated with the movement of liquid water and its interplay with GDL pore structure and wettability warrant further investigation.

2.4 Approach

In this work, fundamental transport mechanisms were investigated through three interrelated approaches in an attempt to increase understanding of water transport in and through GDL materials. The first approach was the introduction of a novel method of mathematically modeling the three dimensional microstructure of GDLs incorporating both carbonized binder and wet-proofing polymer (PTFE). The proposed method closely mimics manufacturing techniques and subsequent characterization of the digital GDLs closely match experimental measurements of commercial GDLs. The second approach provided the new capability to study the water transport in the through-plane direction of PEMFC and measure the temperature gradients across the cathode GDL. This body of work was accomplished using visible and infrared imaging at various magnifications of a custom designed through-plane transparent PEMFC. The third approach was used to investigate fundamental water transport mechanisms through the GDL in a well-controlled ex situ experiment. This approach has revealed newly observed water transport mechanisms and an improved explanation of the role of the MPL in a PEMFC.

Chapter 3

Digital GDL Microstructure Generation

3.1 Introduction

Digital generation of GDL microstructures need to incorporate sufficient detail of actual manufactured GDLs such that the geometric models accurately represent the microstructures while maintaining computational feasibility. Consideration of current manufacturing techniques provides a systematic approach for algorithm development for representative GDLs. Gas diffusion layer manufacturing processes result in a random distribution of the fiber orientations which can be digitally represented as a collection of randomly oriented cylinders. The degree of anisotropy (in-plane versus through-plane directions) can vary from zero (isotropic) to highly anisotropic with all of the fibers oriented in one plane, depending on the manufacturing techniques. For wet-laid GDLs, such as Toray TGP-H series, the microstructure is highly anisotropic and the desired thickness and density of the sample is achieved by stacking up layers during the molding process of manufacturing [9]. This process of stacking is mimicked in this work by virtually stacking digitally constructing 2D layers until the desired thickness is achieved.

The current work expands upon previous stochastic generation studies with a novel method of incorporating both carbonaceous binder and the widely used PTFE treatment

utilizing 3D image processing. To the authors knowledge, this is the first attempt in open literature to include the both the binder and PTFE in virtual GDL generation. Further, the method of adding the binder is unique in that mimics the wetting property of the precursor material (thermoset resin) used in the manufacturing process. The implementation of the proposed algorithm was developed in MATLAB®using a toolbox format organization which allows for extension of the current body of work with minimal overhead cost. Additionally, a new underling framework (based on Schladtiz et al. methodology [39]) is introduced allowing for intuitive input of the desired GDL physical parameters such as fiber radius, GDL thickness, porosity, percent binder, percent PTFE, and voxel size through a user-friendly graphic user interface. Equipped with the virtual 3D GDL, material characterization and boundary conditions required for heat and mass transport simulations can be extracted in a financially and computationally efficient manner.

3.2 Mathematical Model for GDL Microstructures

The GDL of PEMFCs will be modeled using a simplified mathematical model of intersecting cylinders coupled with three dimensional morphological imaging incorporating the carbonaceous binder and PTFE wetting-proofing treatments. The method of adding the binder is unique in that mimics the wetting property of the precursor material (thermoset resin) used in the manufacturing process. The implementation of the overall algorithm (see §3.3) was programmed using a MATLAB toolbox organization allowing for extension of the current body of work with minimal overhead cost. The development of this framework (Based on [28]) for digital GDL microstructure generation allows for intuitive input of the desired GDL physical parameters such as fiber radius, GDL thickness, porosity, percent binder, percent PTFE, and voxel size through a user-friendly graphical user interface. Equipped with the virtual 3D GDL, material characterization and boundary conditions required for heat and mass transport simulations can be extracted in a financially and computationally

efficient manner.

3.2.1 Three Dimensional Fiber Substrate

The graphitized fiber skeleton of a GDL was initially modeled as a random collection of cylinders (carbonaceous binder will be considered in §3.2.2). A cylinder oriented along an arbitrary axis was defined as the collection of all points that are less than one radius from the axis of the cylinder. The axis of the cylinder was uniquely defined by the unit vector $\hat{C}$ and a point (x_o, y_o, z_o) that it passes through. For an arbitrary point (x, y, z) in the domain, the closest point on the axis of the cylinder can be written as:

$$(x_o, y_o, z_o) + [(x - x_o)\hat{C}_1 + (y - y_o)\hat{C}_2 + (z - z_o)\hat{C}_3]\hat{C} \tag{3.1}$$

Thus, in order for an arbitrary point (x, y, z) to be contained by the cylinder defined by $\hat{C}$ and (x_o, y_o, z_o), the squared distance, D, between that point and the closest point on the cylinder axis (defined in Eq. 3.1) must be less than or equal to the square of the radius of the cylinder (See Fig 3.1). The distance between points in 3D Cartesian space is given by the distance formula:

$$D = \sqrt{(x_2 - x_1)^2 + (y_2 - y_1)^2 + (z_2 - z_1)^2} \tag{3.2}$$

Using this formulation, any cylinder in 3D Cartesian space is well-defined. Randomization of the collection of digital fibers is achieved through the use of a pseudo-random number generator for both the orientation, $\hat{C}$, and the point (x_o, y_o, z_o) it passes through. To model highly anisotropic GDL, the z-component of $\hat{C}$ is suppressed and z_0 points are selected such that the fiber skeleton can be constructed by stacking layers until the desired thickness is obtained.

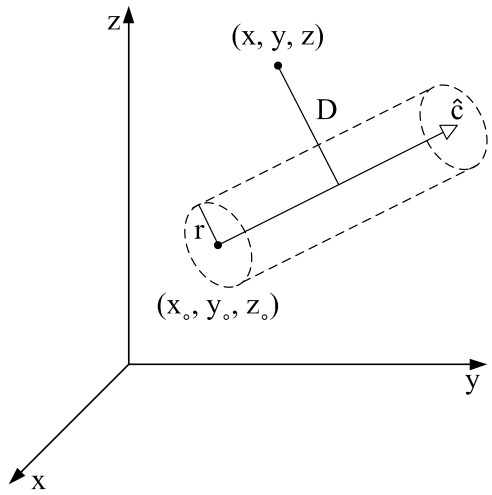

Figure 3.1: Schematic of an arbitrary cylinder of radius r in the direction of $\hat{C}$ that passes through the point (x_o, y_o, z_o). The distance, D, between the closest point on the cylinder axis to the point (x, y, z) determines if a point is contained within the cylinder.

3.2.2 GDL Binder and PTFE

The carbonaceous binder in the final GDL material is added as a thermoset resin in the manufacturing process to allow for flexibility in the final GDL thickness and density [9]. The thermoset resin acts a wetting fluid prior to carbonization as evident in the confocal laser scanning microscope (CLSM) images of Toray TGP-H-060 without PTFE treatment in Fig. 3.2. The image shows the binder material has a relatively low static contact angle on the fibers and generally accumulates at fiber intersections. This process can be mimicked digitally using morphological image processing on the fiber skeleton. This newly developed method of adding the binder material to the fiber skeleton is representative of current manufacturing techniques providing a digital representation of the physical interaction of the binder materials with fibrous substrate.

3.2.2.1 Morphological Image Processing

The area of morphological image processing uses mathematical morphology as a tool to extract regions of interest within images as well as to pre- and post-process images [209].

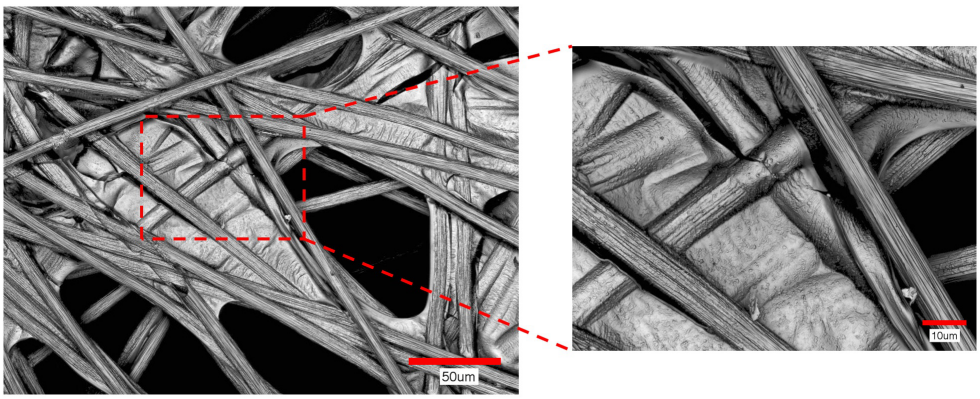

Figure 3.2: Confocal laser microscope images of Toray TGP-H-060 with 0 wt.% PTFE showing the morphology of the carbonized binder.

The current work is concerned with binary images and thus the discussion will be limited to such but for the interested reader is referred to [209] for application to grayscale images. Fundamental to morphological image processing are two basic operations, erosion and dilation, which are the foundation for many morphological processing algorithms.

Morphological erosion, $\ominus$, of an image A using structuring element (SE) B can be defined as [209]:

$$A \ominus B = \{z \mid (B)_z \cap A^c = \emptyset\} \tag{3.3}$$

where z is a point in the image domain ($\mathbb{Z}^n$, $n = 3$ in current work), A^c is the complement of A, and $\emptyset$ is the empty set. Thus, the erosion of A by B is the set of all points z where the intersection of B with the complement of A is the empty set and has the effect of shrinking objects in the image. Similarly, morphological dilation, $A\oplus$ of A by B can be defined as [209]:

$$A \oplus B = \{z \mid (\hat{B})_z \cap A \neq \emptyset\} \tag{3.4}$$

where $\hat{B}$ is the reflection of B about its origin. Dilation has the effect of thickening the objects in the image proportional to the size and shape of the SE. These two fundamental

morphological operations can be combined in series using the same structuring element to perform an opening (erosion followed by an erosion, denoted $\circ$) and a closing (dilation followed by erosion, denoted $\bullet$):

$$A \circ B = (A \ominus B) \oplus B \tag{3.5}$$

$$A \bullet B = (A \oplus B) \ominus B \tag{3.6}$$

Example images of each erosion, dilation, opening, and closing of image are shown in Fig. 3.3 and Fig. 3.4 using structuring elements of a disk of radius 10 and a 20 x 10 rectangle, respectively.

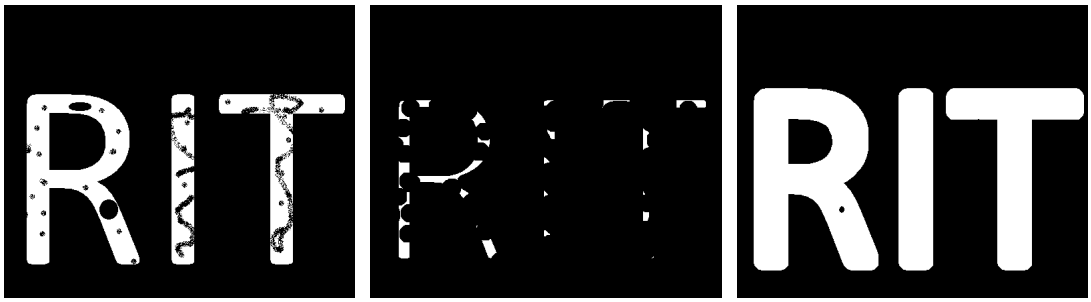

(a) Original (b) Eroded (c) Dilated

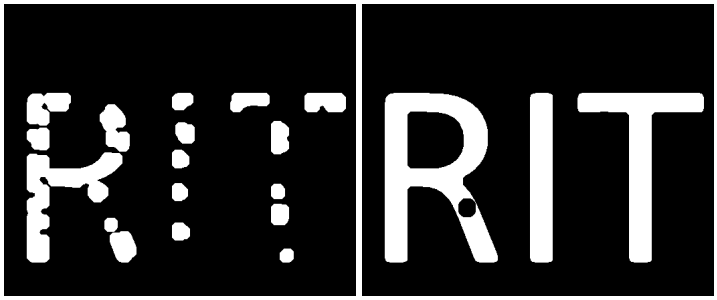

(d) Opened (e) Closed

Figure 3.3: Morphological processing example images using a circular structuring element of radius 10.

The shape and size of the structuring element will have a profound effect on the output image and will depend on application and desired outcome. The three-dimensional closing

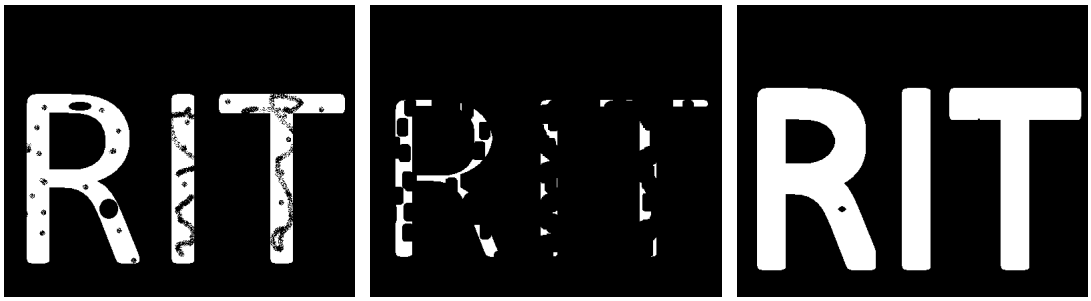

(a) Original (b) Eroded (c) Dilated

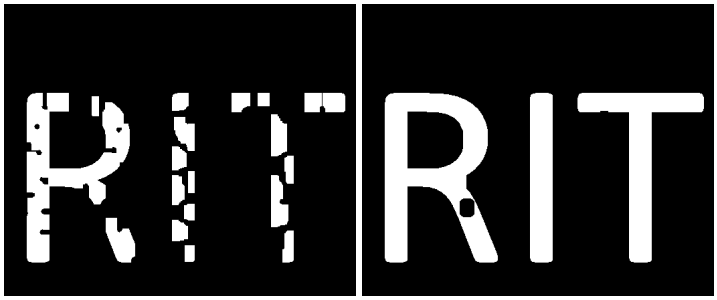

(d) Opened (e) Closed

Figure 3.4: Morphological processing example images using a 20 x 10 rectangular structuring element.

of the fiber substrate with a spherical SE was chosen to mimic the wicking thermoset resin to the fiber substrate in the GDL manufacturing process. This morphological closing of the fibrous skeleton will three-dimensionally add binder material to the substrate in regions of small crevasses such as the intersection of fibers. The amount of binder material added to the fibrous skeleton is proportional to the structuring elements radius with precision controlled by the voxel size. To allow for an intuitive input from the user, a correlation between percent binder added and structuring element radius was computed for cubic voxel size of 1/3 μm and 1/2 μm.

The percent binder as a function of sphere radius was computed by taking the ratio of the binder voxels (obtained by subtracting the initial image from its closing, i.e. a Bottom-hat transformation) to the entire binder plus fiber voxels. The resulting correlation for the 1/3 μm cubic voxel structure with 7 μm fiber diameter and 189 μm thickness is shown in Fig. 3.5 where the spherical SE radius was varied from 0 to 20 and resulted in binder solid

volume fraction spading 0 to 40 %. The correlation for the 1/2 μm voxel structure with a 7 μm fiber diameter and 189 μm thickness is shown in Fig. 3.6 where the spherical SE radius was varied from 0 to 25 and resulted in binder solid volume fraction from 0 to about 70 %. Note from the plots in Figs. 3.5 & 3.6 the 1/3 μm voxels allows for more precise control over the addition of binder. This effect will also propagate the PTFE generation and needs careful consideration for the trade-off between computation time/resources and precision of the target structures generated.

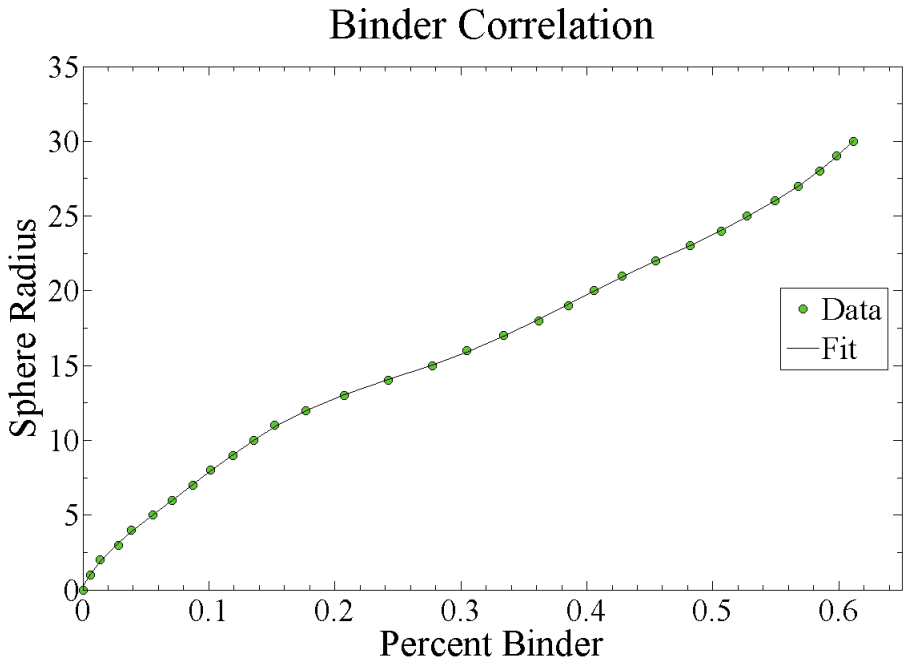

Figure 3.5: Binder correlation using 1/3 μm voxels.

Polytetrafluoroethylene is generally added to GDL materials to increase hydrophobicity and reduce water holdup allowing for more reactant pathways to the CL. Figure 3.7 shows a CLSM image of Toray TGP-H-060 with 10 wt.% PTFE treatment. Notice the addition of very small dark regions that do not appear in Toray samples without PTFE treatment (Fig. 3.2). A high magnification CLSM image of Toray TGP-H-060 with 40 wt.% PTFE and 0 wt.% PTFE are shown in Fig. 3.8 for comparison. Notice that the darker regions that are absent without PTFE treatment appear to be comprised of very small ($<$0.5 μm)

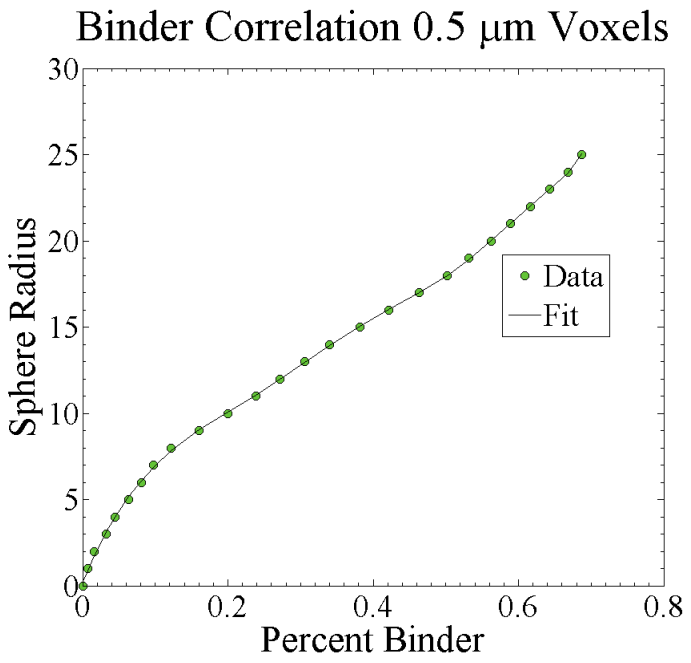

Figure 3.6: Binder correlation using 1/2 μm voxels.

particles. This finding is consistent with PTFE resin particles used in aqueous dispersions for impregnation porous woven goods such as Teflon®PTFE TE-3836 from DuPont™.

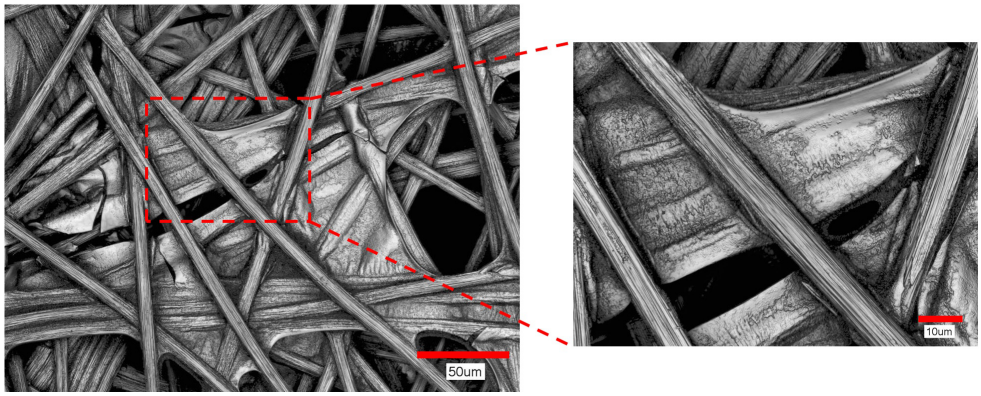

Figure 3.7: CLSM images of Toray TGP-H-060 with 10 wt.% PTFE. Note the dark regions concentrated in small crevasses not present in TGP-H-060 without PTFE (Fig. 3.2).

An additional morphological closing was conducted for the addition of the commonly used PTFE. This PTFE closing step was accomplished by using a closing with a spherical structuring element of a larger radius than the binder step. The weight percent PTFE added

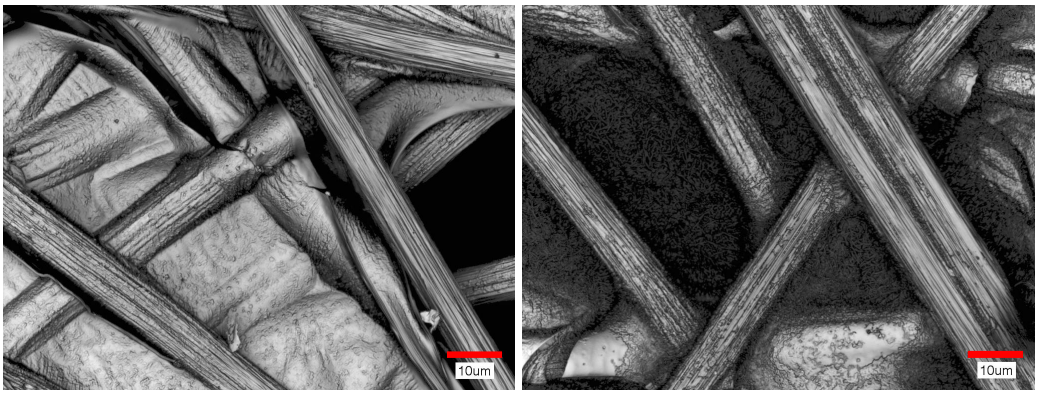

(a) Toray TGP-H-060 with 0 wt.% PTFE (b) Toray TGP-H-060 with 40 wt.% PTFE

Figure 3.8: CLSM images of Toray TGP-H-060 with and without PTFE. Note the accumulation of small (<0.5 μm) dark particles percent in (b) that could be attributed to the addition of PTFE.

to the GDL is controlled by the difference in radii (of the structuring elements) between the binder and PTFE steps. A correlation of structuring element radius versus volume fraction PTFE when using 27 wt.% binder in the 1/3 μm voxel structure is shown in Fig. 3.9. A similar correlation for the 1/2 μm voxel structure with 30 wt.% binder is shown in Fig. 3.10. Note the correlation using 1/3 μm voxels provides more control over the PTFE addition compared to the 1/2 μm voxel. The 1/3 μm structure generation requires more memory and computation time to generate the same GDL volume and depending on application, may provide unnecessary detail.

3.3 Generation Algorithm

The algorithm used in the current work for GDL generation was programmed in MATLAB with a flexible architecture and graphical user interface. The algorithm uses the following input parameters:

- Substrate (fibers and binder) porosity
- Fiber radius

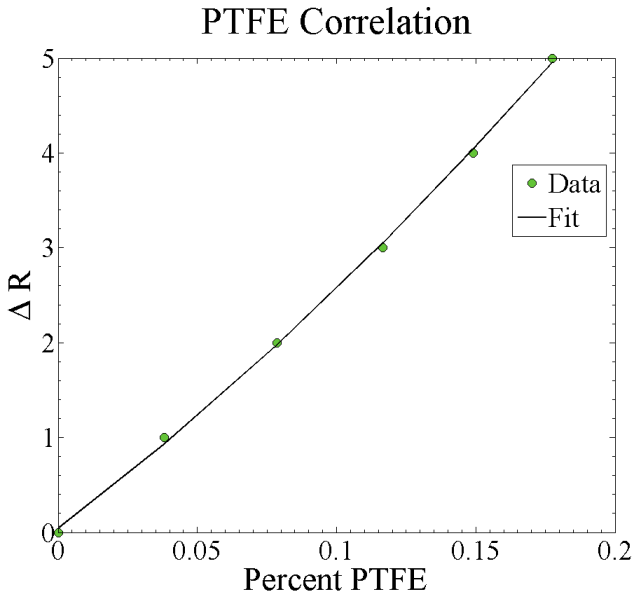

Figure 3.9: Correlation between percent PTFE added and difference in structuring element radius for 27 wt.% binder with 1/3 μm voxels.

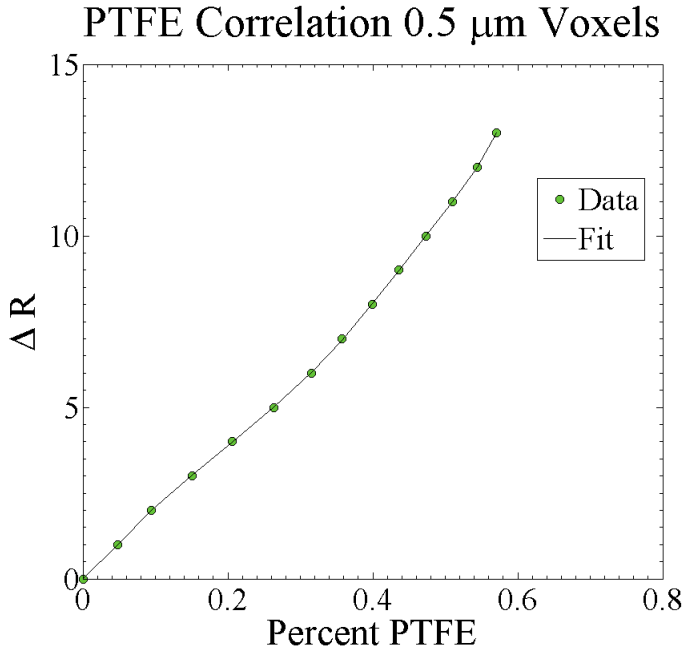

Figure 3.10: Correlation between PTFE addition and difference in structuring element radius for 30 wt.% binder with 1/2 μm voxels.

- Substrate thickness
- Volume fraction of binder
- Voxel physical size
- Domain size
- Volume fraction of PTFE

and the digital GDL was generated using the following algorithm:

1. Initiate the state of the pseudo-random number generator
2. Estimate the number of fibers required per layer from porosity and binder VF inputs
3. Randomly generate the point for the fiber to pass through (x_o, y_o) for two layers
4. Randomly generate the fiber orientation $\hat{C}_1$, $\hat{C}_2$ and normalize for two layers
5. Construct two layers using Eq. 3.1
6. Add binder VF using correlation in Fig. 3.5
7. Compute porosity
8. If necessary: adjust number of fibers and iterate steps 1 &3-7 until porosity converges
9. Generate all layers
10. Add PTFE VF using correlation in Fig. 3.9

Figure 3.11 shows a block diagram of the processing steps used to create digital GDLs with binder and PTFE used in this work. The overall functionally of the generation algorithm was used through a graphical user interface for simple interfacing.

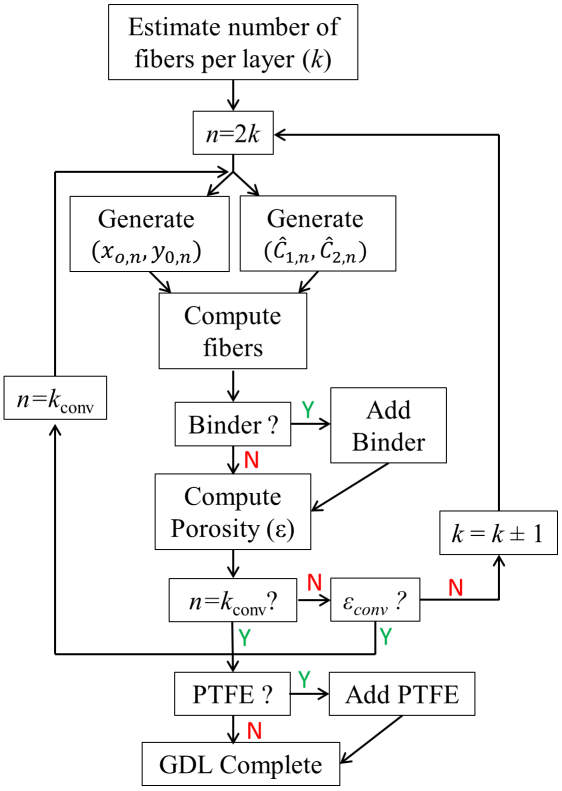

Figure 3.11: Block diagram outlining processing steps used in the generation algorithm.

3.3.1 GUI Design

The digital generation algorithm was implemented through the use of a user-friendly graphical user interface (GUI). A screen shot of the GUI is should in Fig. 3.12 with input and output parameters on the upper and lower left hand side, respectively. The GUI allows the user to visually examine the generated structure from the three perpendicular 2D views in one voxel steps. The displayed colors of each solid phase can be adjusted to the user's preference using the color map box in the lower right. Red, green, and blue inputs for each phase must be values between 0 and 255. The converged porosity, binder and PTFE volume fractions are also displayed on the lower left. The resulting structure can be saved as a multi-paged tiff and/or stored as a 3D array in the main MATLAB workspace. This GUI allows for simple operation of the overall algorithm without the need to call individual functions.

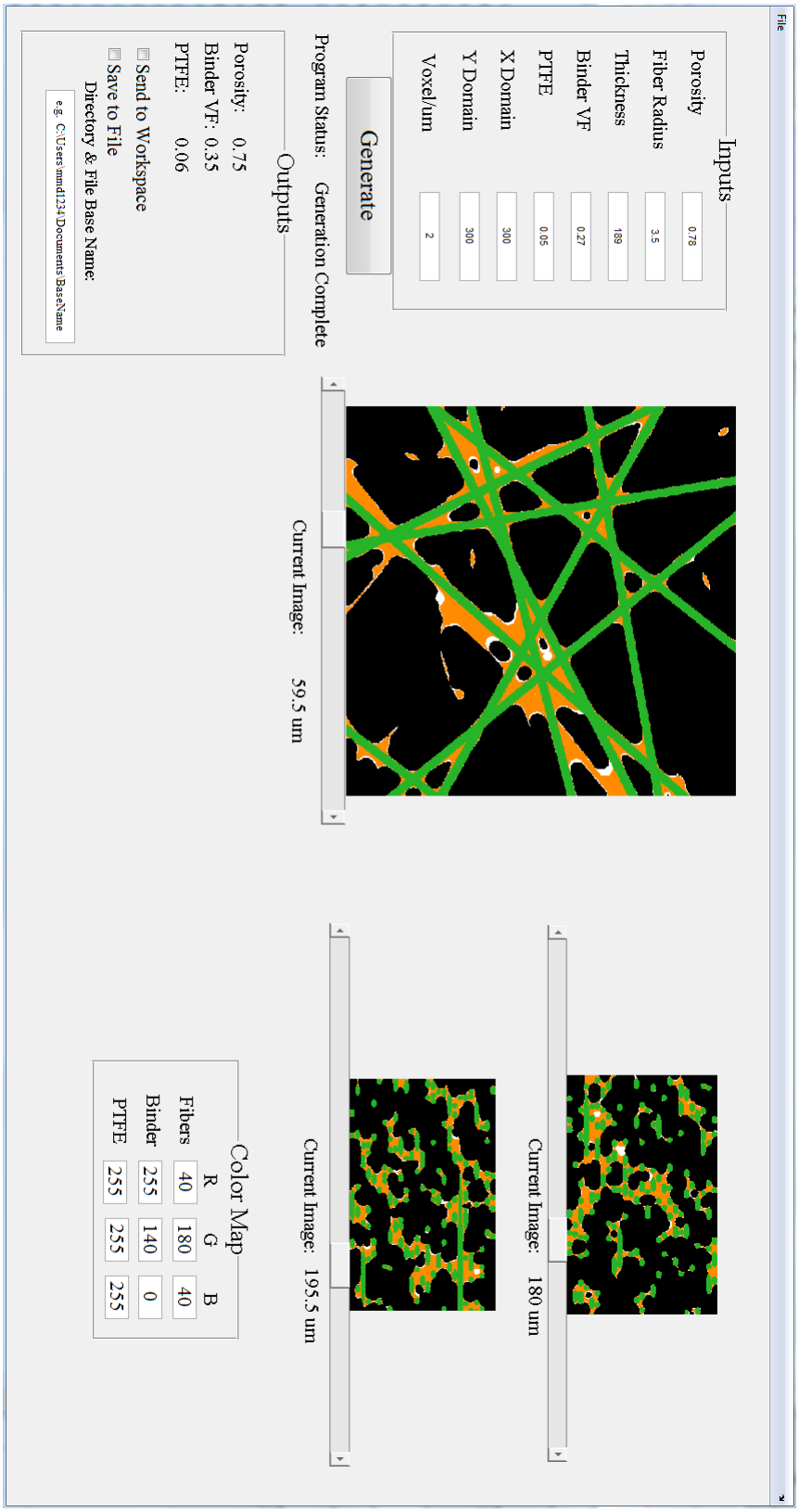

Figure 3.12: Graphical user interface for GDL digital generation.

3.4 Microstructure Characterization

3.4.1 Global Porosity

The fiber and binder are considered in calculation of the global porosity during the generation algorithm outlined in §3.3 for comparison to manufacturer data. After the completed GDL structure is generated (with or without PTFE), the global porosity is computed again for material characterization and comparison to literature data. The generated microstructure is three-dimensional phase indexed image which facilitates global porosity computation. The global porosity is computed by searching for and counting the number of void voxels and taking their ratio with the total number of voxels. This computation is used in two ways in the generation algorithm. Firstly, it is used when generating the initial two layers for convergence on the number of fibers needed for each layer. After the entire microstructure is generated, the global porosity is computed again to reveal the resulting porosity.

3.4.2 Local Porosity Distribution

Local porosity variations throughout the GDL have a strong influence on the local mass transport phenomena and needs to be well characterized for modeling efforts. Determination of local porosity has conventionally been unattainable using porosimetry techniques used for global porosity measurements (such as mercury intrusion) but recently has been explored [37]] using advanced imaging techniques. Utilizing the three dimensional nature of the GDLs generated in this work, local variations with arbitrary resolution is implemented in a similar manner as global porosity with sliding computation domain.

3.5 Results

A digital GDL that with binder and PTFE was generated using the algorithm detailed in §3.3. A single layer of the GDL was extracted from the 3D structure to exemplify each step of the generation process. The initial step of generating the fibrous skeleton of the GDL is shown in Fig. 3.13 where the fibers were arbitrarily colored green. The crimp of the fibers was assumed negligible and this assumption can clearly be seen in Fig. 3.13 with intersecting fibers. The second step in generating the digital GDL was to add the carbonaceous binder material used in the manufacturing process. The result of the method described in section 3.2.2 on the single layer of fiber is shown in Fig. 3.14 where the binder material is colored orange. Notice from the image that the added binder material behaved like a wetting fluid as discussed in §3.2.2. The last step in the generation algorithm was to add PTFE to the GDL 3D microstructure as is commonly done for GDL used in PEMFCs. The result of this last processing step is shown in Fig. 3.15 where the PTFE is colored cyan. Note that the PTFE in this processing step also filled in small crevasses and somewhat reduced the porosity of the overall sample.

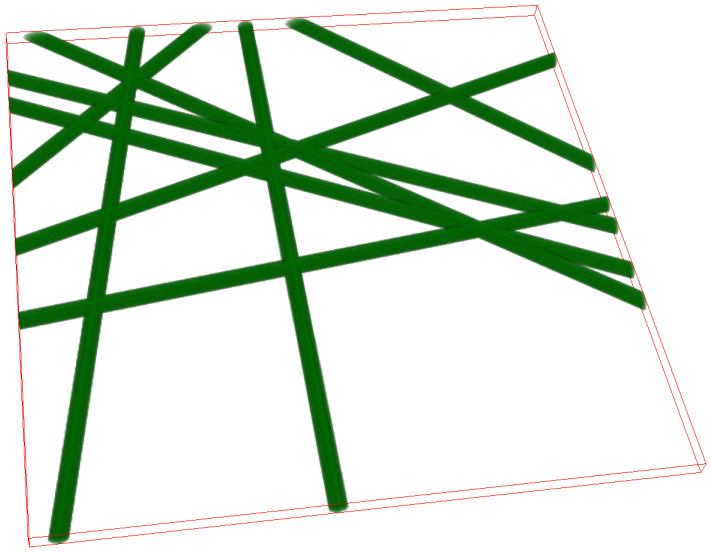

Figure 3.13: Single layer of the fibrous skeleton of the GDL microstructure.

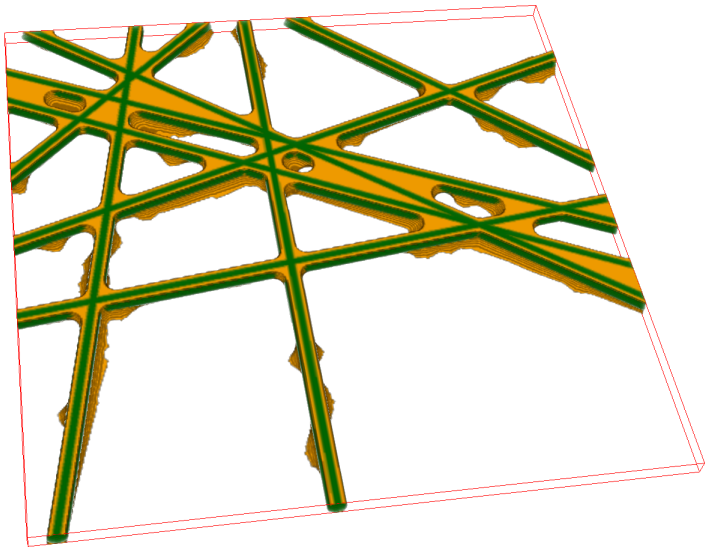

Figure 3.14: Single layer of the GDL fibers complete with carbonized binder (Fiber = green and Binder = orange).

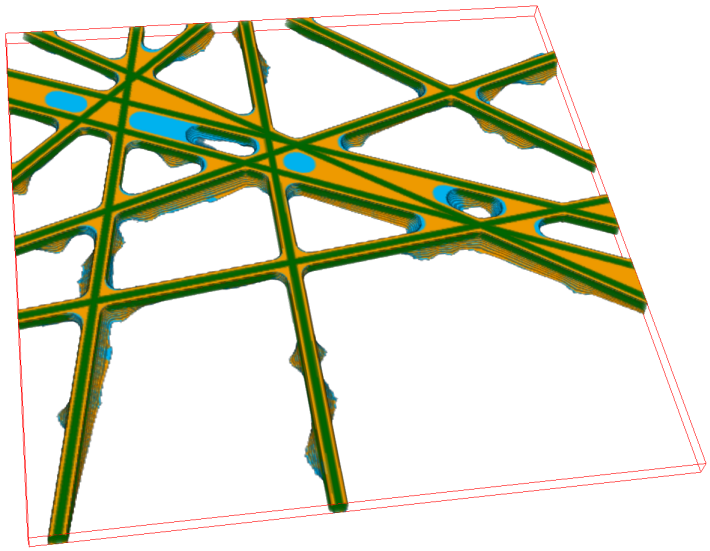

Figure 3.15: Single layer of a generated GDL including wet-proofing treatment (Fiber = green, Binder = orange, and PTFE = cyan).

3.5.1 Toray TGP-H-060 Generation

The motivation for the digital generation of the 3D microstructure of GDL materials was to obtain the 3D geometry and solid phase distribution of commercial GDLs for transport

modeling. Toray TGP-H-060 was chosen as a commonly used and commercially available GDL to test the generation algorithm. Toray TGP-H-060 has 7 μm fiber diameters, thickness of 190 μm, and is composed of $\approx$ 27 % solid fraction carbonaceous binder [210]. These values were used as input parameters in the generation algorithm combined with a Δr = 2 for the SE radius for the PTFE step for direct comparison to experimental data. Figure 3.16 shows the three dimensional view of the generated structure with 1/3 μm voxels (250 x 250 x 189 μm) with fibers, binder, and PTFE colored green, orange, and cyan, respectively. The resulting porosity of the GDL without PTFE treatment was determined to be 75 % with a 27 % solid volume fraction of binder both of which are in good agreement with literature and manufacturer data.

The microstructure of Toray TGP-H-060 was also generated using cubic voxels of 1/2 μm with the associated correlations given in section 3.2.2. This structure requiring less computational time and memory compared to the 1/3 μm voxel structure was generated using input put parameter of 27 % binder and a target porosity of 78 %. The resulting digital GDL substrate was subsequently processed to add PTFE with a Δr = 1 for the SE to obtain a lower PTFE loading than the structure shown in Fig. 3.16. The resulting structure domain was 500 x 500 x 189 μm and is shown in Fig. 3.17. The resulting structure had a global porosity of 81 % with 30 % binder solid volume fraction prior to the addition of PTFE.

The generated structure with 1/3 μm voxels is shown from the top view in Fig. 3.18 using a linear decrease of intensity as a function of depth (maximum of 50 μm from top surface) into the substrate. Note from Fig. 3.18 how the binder and PTFE accumulate at the intersection of fibers throughout. This effect of the generation algorithm is also observed for the structure with 1/2 μm voxels with the larger domain of 500 x 500 x 189 μm shown in Fig. 3.19.

A more direct qualitative comparison to Toray TGP-H-060 is shown in Fig. 3.20 where a CLSM image of Toray TGP-H-060 is shown in Fig. 3.20(a) with a grayscale image of the

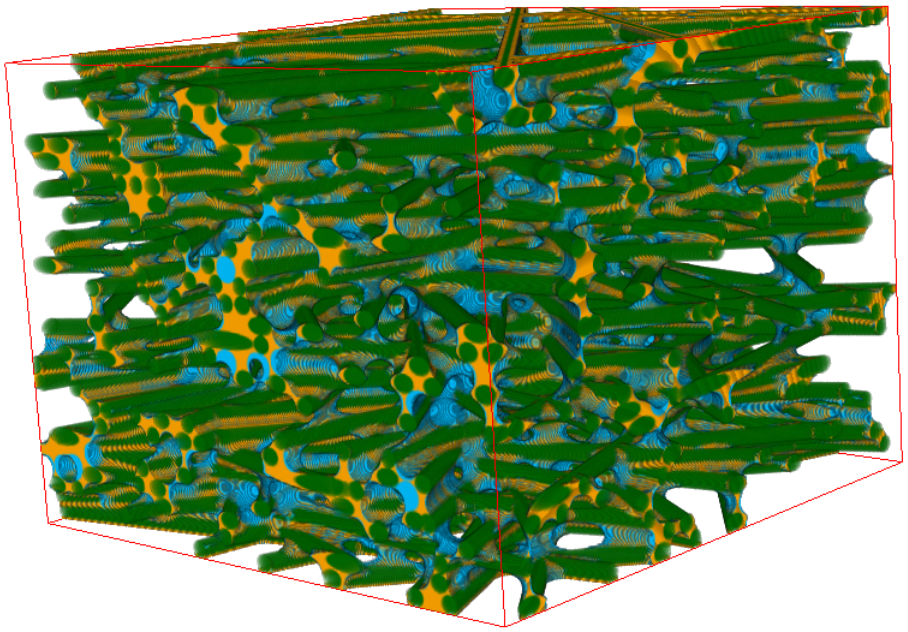

Figure 3.16: Three dimensional view of simulated Toray TGP-H-060 with 9 wt.% PTFE (Fiber = green, Binder = orange, and PTFE = cyan).

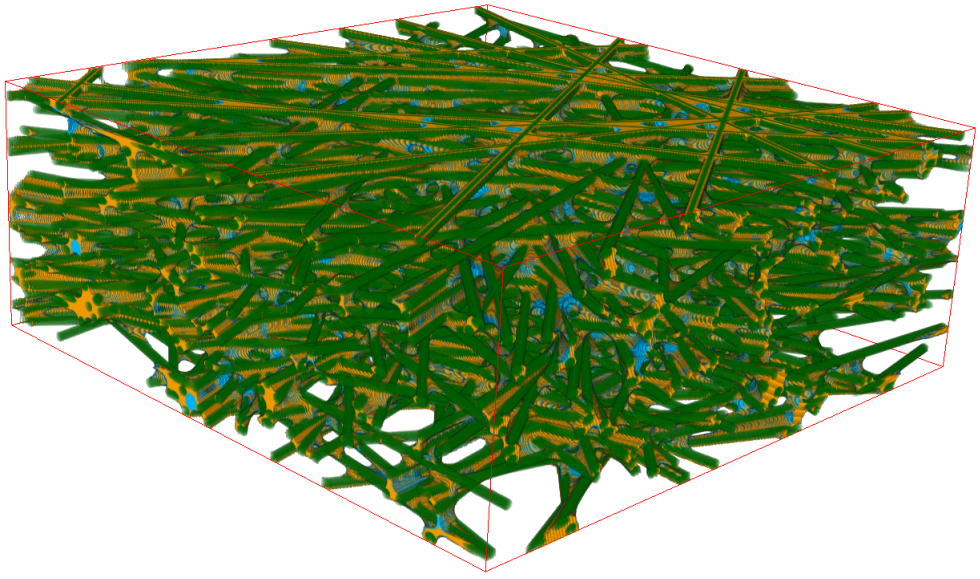

Figure 3.17: Three dimensional view of simulated Toray TGP-H-060 with 5 wt.% PTFE (Fiber = green, Binder = orange, and PTFE = cyan).

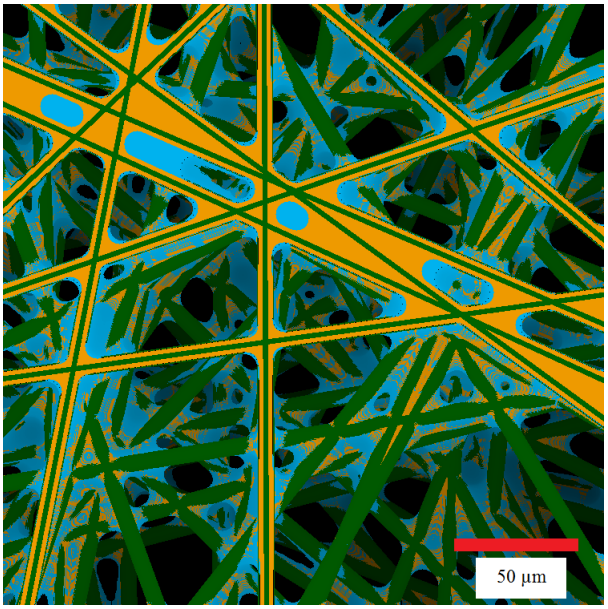

Figure 3.18: In-plane view (250 x 250 μm) of simulated Toray TGP-H-060 with 9 wt.% PTFE with intensity linearly decreasing as a function of depth (Fiber = green, Binder = orange, and PTFE = cyan).

modeled GDL with the phase color scheme removed shown in Fig. 3.20(b). The grayscale in Fig. 3.20(b) is representative of depth with a maximum distance of 50 μm. Figure 3.21 shows the comparable image from the 1/2 μm voxel structure with the larger domain of 500 x 500 μm. Notice from the image the larger scale changes in the in the fiber and binder clustering that wasn't available in the smaller domain (Fig. 3.20).

The generated 3D phase-labeled microstructure allows for material characterization on any part or whole that may be unavailable otherwise. A 1/3 μm slice in the central region of the structure reveals how the specific phases are distributed (Fig. 3.22). Although the binder and the PTFE make up a significant proportion of the overall mass of the GDL, the void (black) regions remain fairly open in this section. This implies that the interconnected pore structure remains fairly well open in the presence of PTFE. Notice from the image in Fig. 3.22 that all four edges remain mainly clear of obstructions allowing for many pathways for transport of reactants and product water. This local 2D examination of the microstructure changes quite quickly as shown in Fig. 3.23 which is only 20 μm from the

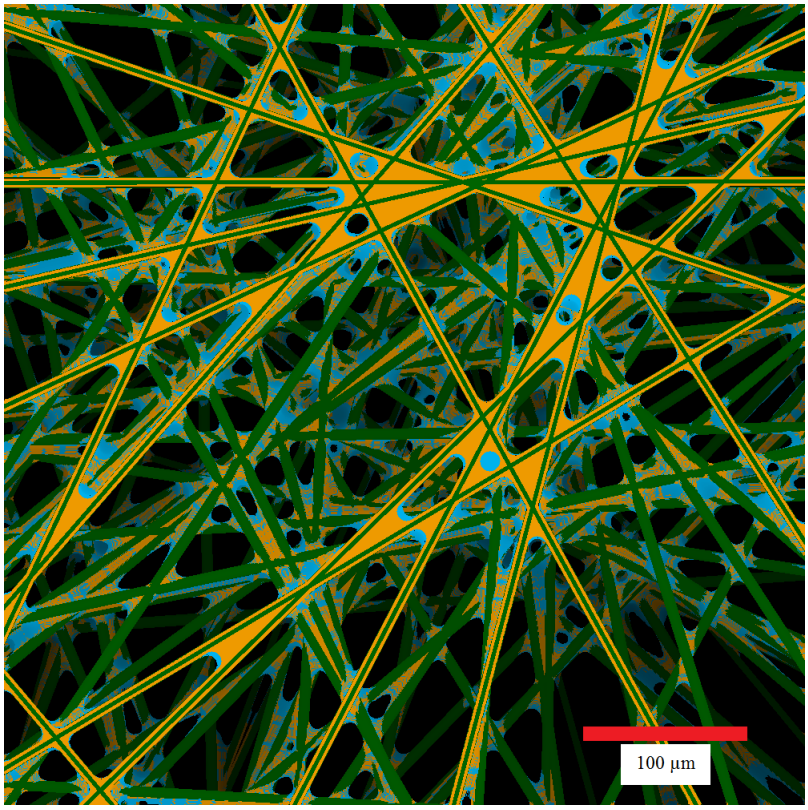

Figure 3.19: In-plane view (500 x 500 μm) of simulated Toray TGP-H-060 with 5 wt.% PTFE with intensity linearly decreasing as a function of depth (Fiber = green, Binder = orange, and PTFE = cyan).

the section in Fig. 3.22. Notice along the bottom edge of the image that the solid phases are interconnected almost to the edge of the domain. This configuration would severely limit access to and from the catalyst layer in a PEMFC. Furthermore, comparing the local porosities of these central through-plane images reveal that the section in Fig.3.22 is less porous (69 %) than the section in Fig.3.23 (72 %). This exemplifies the need to consider local variations of material properties such as porosity and tortuosity three-dimensionally.

The larger domain size of the 1/2 μm voxel structure reveals larger scale through-plane distributions of the solid phases as shown in Fig. 3.24 of a 1/2 μm central slice. The pore structure shown in Fig. 3.24 is very interconnected and the decrease in PTFE content compared to Fig. 3.22 is also apparent (5 % vs. 9 %). The global porosity of this central slice is somewhat greater (78 % vs. 69 %) than the central slice from the 1/3 μm structure and

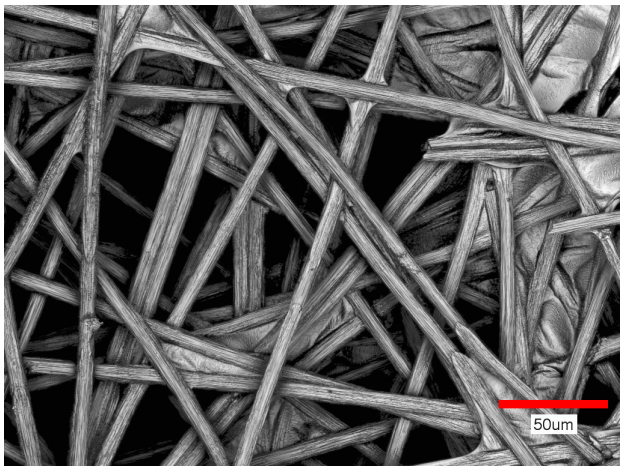

(a) Toray TGP-H-060 with 0 wt.% PTFE

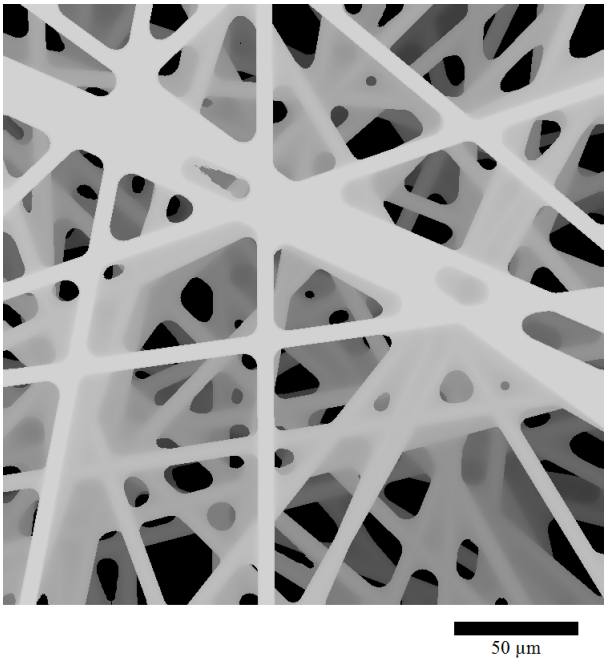

(b) Generated GDL without phases differentiated and depth shown in grayscale

Figure 3.20: Comparison to CLSM image of Toray TGP-H-060 0 wt.% PTFE to digital generation.

is reflected in the pore connectivity. Additionally, from visual inspection alone, the local tortuosity of the central slice appears to be lower but detailed analysis would be required for confirmation. Nonetheless, small changes in global parameters such as porosity (75 % vs. 81 %) and binder solid volume fraction (27 % vs. 30 %) can significantly affect local

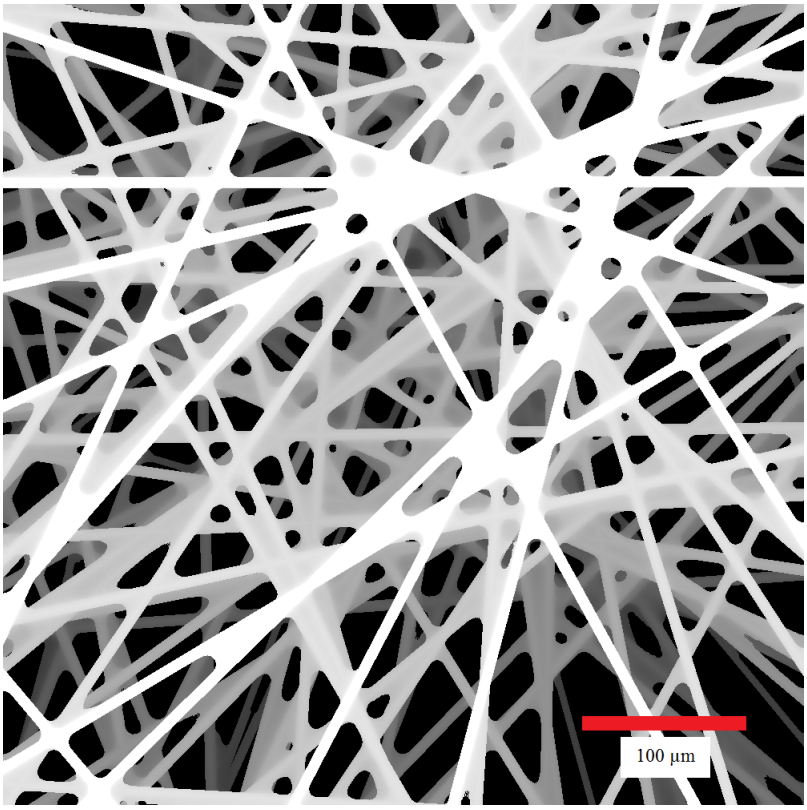

Figure 3.21: In-plane view (500 x 500 μm) of simulated Toray TGP-H-060 with 5 wt.% PTFE with depth shown in grayscale.

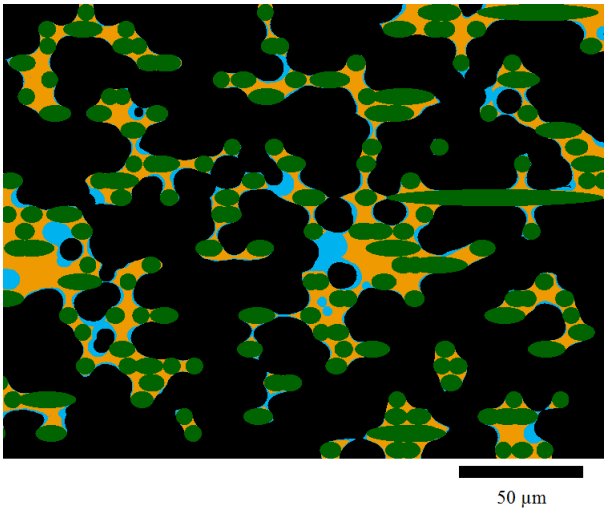

Figure 3.22: Through-plane 1/3 μm section of simulated Toray TGP-H-060 with 9 wt.% PTFE. Note the open pore structure throughout to the end of the domain (Fiber = green, Binder = orange, and PTFE = cyan).

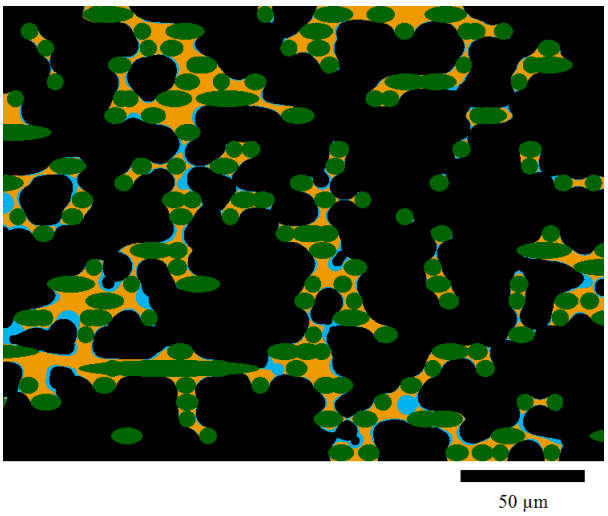

Figure 3.23: Through-plane 1/3 μm section of simulated Toray TGP-H-060 with 9 wt.% PTFE 20 μm from the section shown in Fig. 3.22. Note the open pore structure throughout with significant solid barrier near the bottom edge of the domain (Fiber = green, Binder = orange, and PTFE = cyan).

transport properties. These changes in local properties are very sensitive to the volume and location sampled as exemplified by the 1/2 μm cross-sectional slice shown in Fig. 3.25 which was sampled only 25 μm from the image shown in Fig. 3.24. The local porosity of this slice is about the same as that of the previous slice (79 % vs. 78%) but the physical distributions and associated restrictions to mass, heat, and electronic transport are different. These small changes in the physical arrangement of the fiber, binder, and PTFE in relation to the channel and land configuration in an actual PEMFC could have a strong effect on the local current density, water saturation, and temperature distribution and should be accounted for in modeling efforts.

3.5.1.1 Local Porosity

Local porosity variations can have a strong effect on the local transport properties and thus influence local current density. To further evaluate the generated GDL, the local porosity distribution was calculated as described in §3.4.2 using a 25 μm x 25 μm x 189 μm averaging box. The result is shown in Fig. 3.26 with the color scale representative of porosity and

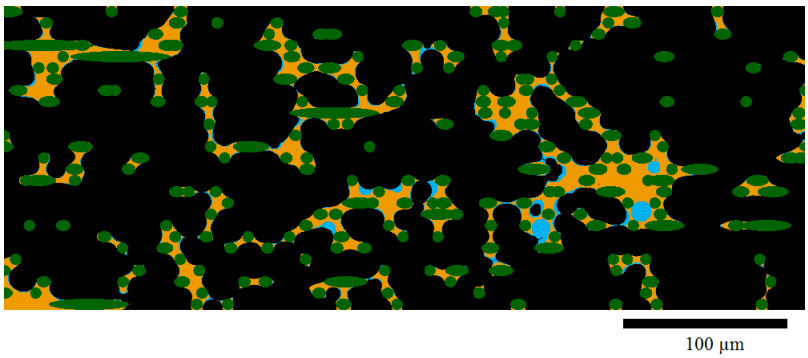

Figure 3.24: Through-plane 1/2 μm section of simulated Toray TGP-H-060 with 5 wt.% PTFE extracted from the central region of the generation domain (500 x 500 μm). Note the open interconnected pore structure throughout with a local porosity of 79 % (Fiber = green, Binder = orange, and PTFE = cyan).

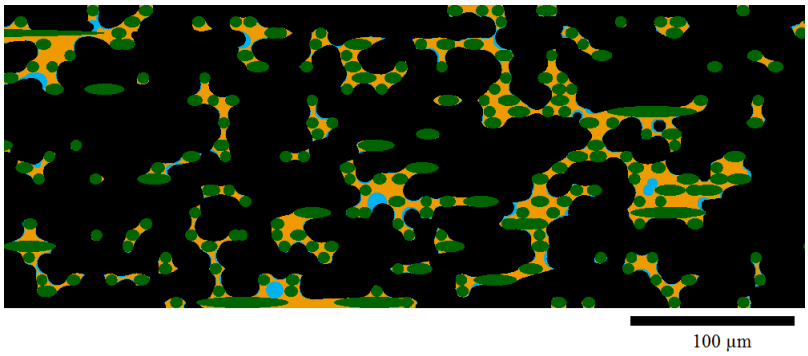

Figure 3.25: Through-plane 1/2 μm section of simulated Toray TGP-H-060 with 5 wt.% PTFE extracted from the central region of the generation domain (500 x 500 μm) 25 μm from the central slice shown in Fig. 3.24. Note the significant difference in the local distribution of fibers, binder, and PTFE compared to Fig. 3.24 even with a similar porosity of 79 % (Fiber = green, Binder = orange, and PTFE = cyan).

each square representing 625 μm^2 area in the in-plane direction through the entire GDL thickness. Note from the figure that porosity has significant variation (Shown in a color spectrum from blue representing the lowest to red representing the highest porosity) at this scale. Local changes in the porosity was also observed for the structure with 1/2 μm voxels and are shown using the same 25 μm x 25 μm x 189 μm averaging window in Fig. 3.27. Local porosity variation on the order of channel separation (1 mm) in actual PEMFCs is revealed in Fig. 3.27 that could have a strong influence on local performance depending

on channel and land configuration directly above (or below) the GDL structure. Regions of high porosity (e.g. see lower right of Fig. 3.27) may have a negative impact on the location performance in the presence of a land. Higher porosity in the through-plane direction implies less fiber to fiber interaction and binder material and thus would result in lower thermal and electrical conductivity with the latter decreasing performance. Additionally, if the surface of the GDL also has high porosity, the contact resistance would be greater due to lack of GDL material to make intimate contact with the lands. These localized regions of high porosity may also provide regions for water to accumulate increasing water saturation and reducing available reactant flow paths. Thus it is clear that these local variations have a complex effect on the overall performance and should be carefully considered for improved modeling efforts over the typically used assumption of homogeneous porosity.

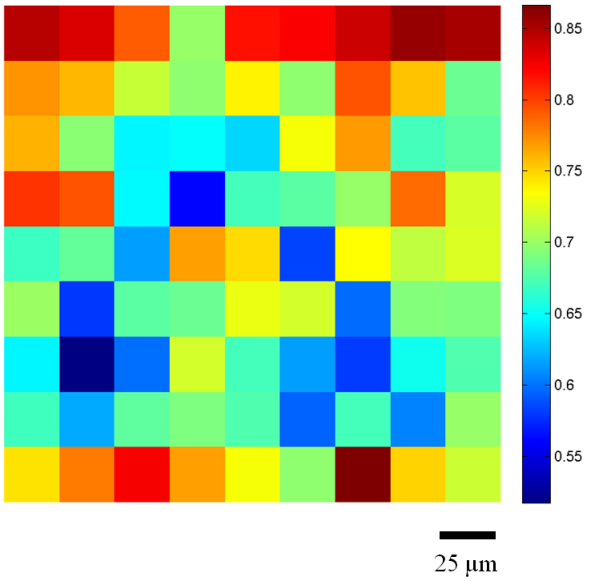

Figure 3.26: Local porosity variation mapped to a color spectrum of simulated GDL (1/3 μm voxels) with 9 wt.% PTFE averaged in the through-plane direction (189 μm) with 25 μm x 25 μm bins in the in-plane direction.

The through-plane direction of GDL materials controls the direct path from the gas distribution channels where reactants are supplied to the catalyst layers where water is generated. Thus the transport properties in the through-plane direction should be well charac-

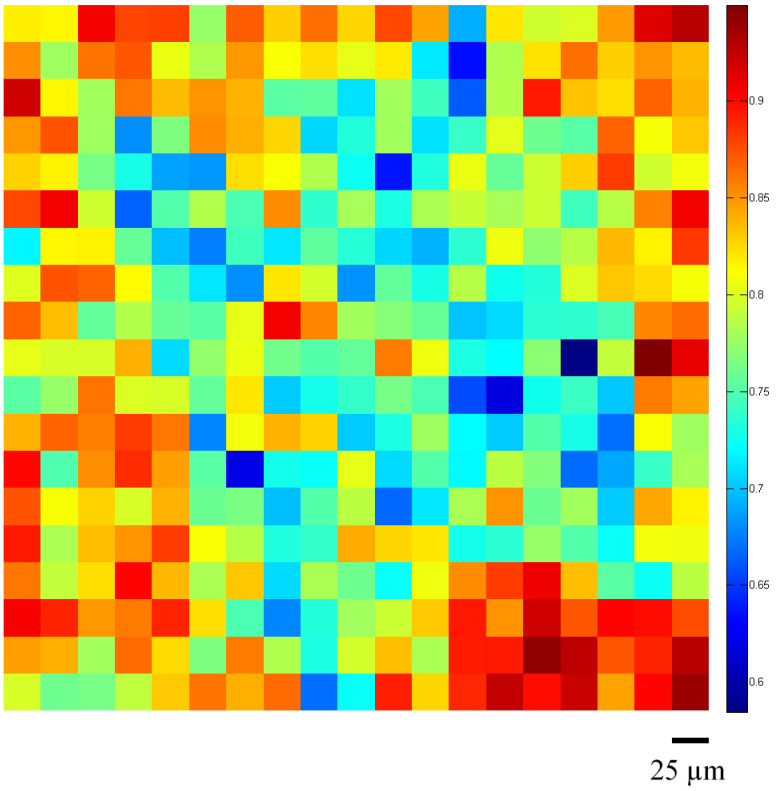

Figure 3.27: Local porosity variation of simulated GDL (1/2 μm voxels) with 5 wt.% PTFE averaged in the through-plane direction (189 μm) with 25 μm x 25 μm bins in the in-plane direction.

terized for material evaluation. The anisotropic nature of GDL materials results in different (for some parameters drastic) values of material properties such as porosity. The through-plane distribution of porosity for the simulated Toray TGP-H-060 with 5 wt.% PTFE is shown in Fig. 3.28. Note from the plot that the porosity changes significantly through the thickness of the GDL. The period of the variations shown in Fig. 3.28 are a result of the layered skeleton of Toray GDLs. The intersection of two layers is where the fibers from both layers are the thinnest (in-plane) and contribute less to the over solid volume. However, the intersection of the fiber layers is also where there is a significant amount of fiber-fiber interaction for the 3D application of binder and PTFE materials. The dominant factor affecting this cyclic pattern was the volume contribution from the fibers and

the contributions from binder and PTFE was not sufficient to compensate. The associated through-plane distributions of binder and PTFE will discussed in section 3.5.1.2.

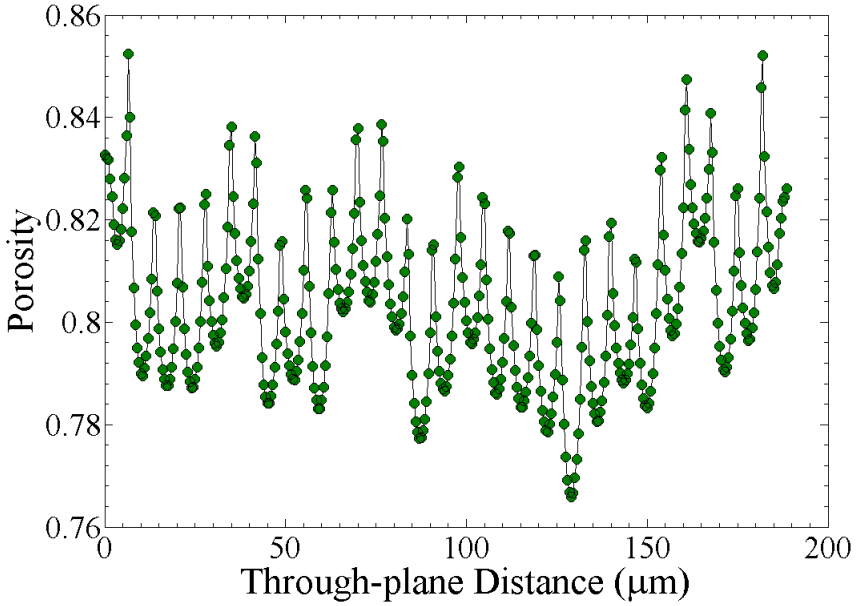

Figure 3.28: Through-plane porosity distribution of simulated GDL (1/2 μm voxels) with 5 wt.% PTFE. Note the cyclic pattern with maximum porosity at layer intersections (every fiber diameter (7 μm)).

3.5.1.2 Through-plane Binder and PTFE Distributions

Due to the established importance of the through-plane properties on water management, the distributions of binder and PTFE were analyzed. The through-plane distribution of binder material was calculated by computing the volume of binder in each 1/2 μm slice through the simulated structure of Toray TGP-H-060 with 5 wt.% PTFE. The volume of binder was then divided by the total volume of binder throughout the structure (and multiplied by 100) to obtain the percent binder in each slice. The resulting plot is shown in Fig. 3.29. Notice from the plot the cyclic pattern in the amount of binder throughout the thickness of the GDL. The period of the oscillation is in agreement with the thickness of a fiber layer and diameter of 7 μm. This was an expected result of interaction of the fiber layers.

The layer-to-layer interactions will provide more regions for binder to accumulate and thus the percent binder is a local maximum at these locations. Furthermore, note that the phase of these oscillations is π out of phase with the oscillation in the porosity reported in Fig. 3.28. Thus, the increase in binder at layer interfaces does not counteract the decrease of volume from the reduced contribution of the fibers.

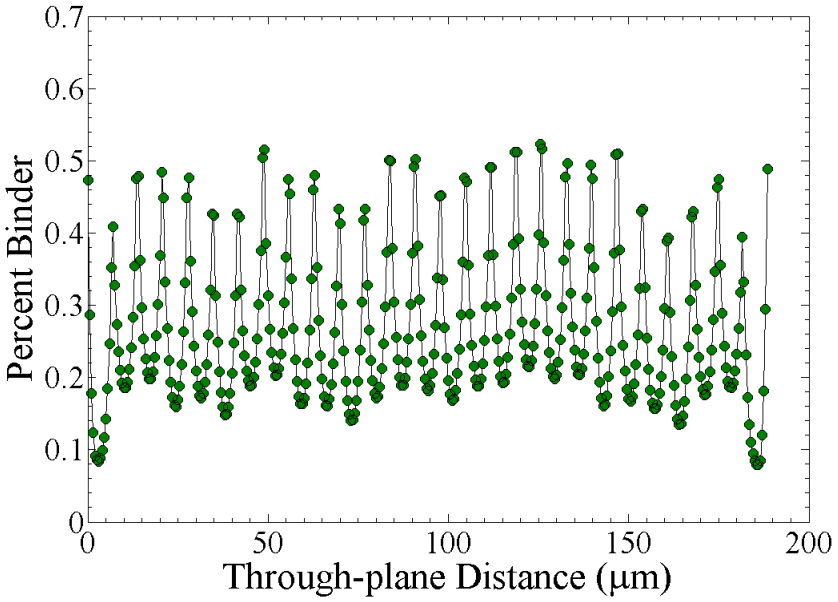

Figure 3.29: Through-plane binder distribution of simulated GDL (1/2 μm voxels) with 5 wt.% PTFE. Note the cyclic pattern with maximums at layer intersections (every fiber diameter (7 μm)).

The through-plane distribution of PTFE for the simulated Toray TGP-H-060 with 5 wt.% PTFE was calculated using a method analogous to that used for the binder distribution. The result is shown in Fig. 3.30. The same cyclic pattern observed for the binder is clearly present with a period of the layer thickness and in phase with maximum binder volume at layer interfaces. This was an expected result of the PTFE generation method which was based on the binder step. Although binder and PTFE both have maximum contributions to the solid volume at interfaces, the volume of the fibers dominates the solid volume.

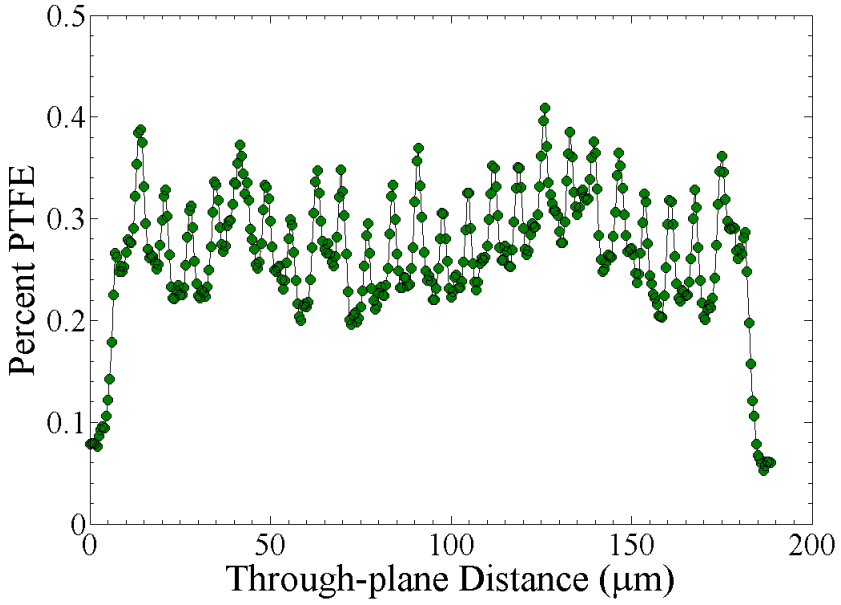

Figure 3.30: Through-plane PTFE distribution of simulated GDL (1/2 μm voxels) with 5 wt.% PTFE. Note the cyclic pattern with maximum at layer intersections (every fiber diameter (7 μm)).

3.5.1.3 Comparison to Actual GDL

The actual 3D structure of Toray TGP-H-060 without PTFE was obtained by Becker et al. using synchrotron-based phase contrast X-ray tomographic microscopy and can used to directly compare the generated GDL with PTFE removed [32]. Since the generated GDL is phase indexed 3D image, only a simple logic step is required to remove the PTFE for the comparison. A 3D view of the generated GDL is shown in Fig. 3.31(a) with a 3D view of actual Toray TGP-H-060 without PTFE shown in Fig. 3.31(b). Note from these images that the generation algorithm performed fairly well generating a digital realistic GDL. A more direct comparison of the generated structure to the actual structure as imaged by Becker et al. [32] is shown in Fig. 3.32 utilizing the larger domain of the 1/2 μm voxel generation to obtain a similar field of view as that achieved by Becker et al. [32]. The image in Fig. 3.32 is also in good agreement with the image of the actual GDL shown in Fig. 3.31(b).

The addition of binder in the generation algorithm was an attempt to mimic manufac-

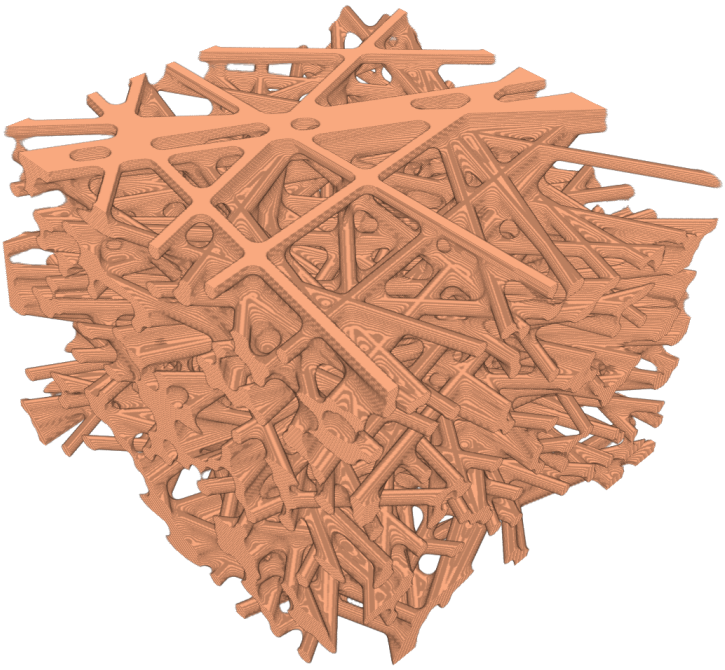

(a) Simulated Toray TGP-H-060 with 0 wt.% PTFE

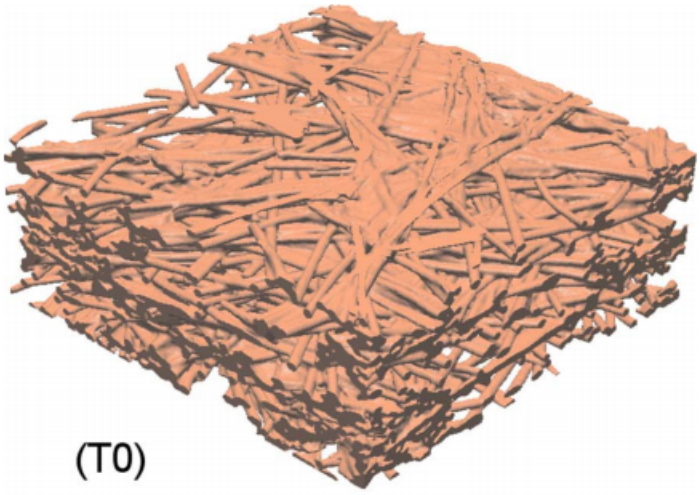

(b) Actual Toray TGP-H-060 with 0 wt.% PTFE [32]. Reprinted with permission from *J. Electrochem. Soc.* **156** (10) B1175-B1181 (2009). Copyright 2009, The Electrochemical Society.

Figure 3.31: 3D Comparison of the generation algorithm to actual GDL.

turing techniques and the result were in agreement to top view CLSM images in Fig. 3.20. Further comparison of the through-plane distribution and binder interaction with the fiber skeleton can be made from Becker et al. results [32]. Figure 3.33(a) shows a cross-sectional

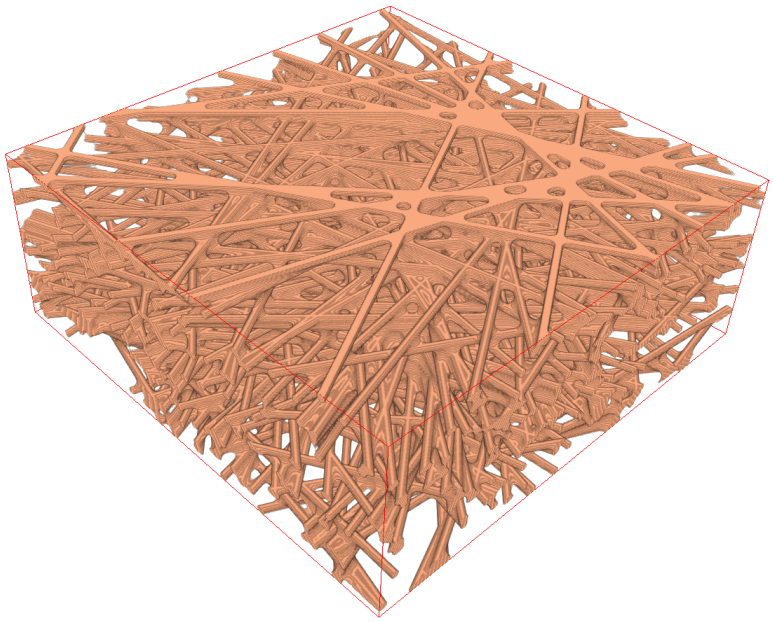

Figure 3.32: Simulated Toray TGP-H-060 with 0 wt.% PTFE (500 x 500 x 189 μm).

slice of the generated model of Toray TGP-H-060 0 wt.% PTFE and Fig. 3.33(b) shows a similar cross-sectional slice of actual Toray TGP-H-060 0 wt.% PTFE obtained through X-ray tomography. The quantity and interaction of the binder with fibers in these images are in close agreement indicating the model of the binder is representative of actual GDL materials. This agreement is also observed for the structure with 1/2 μm voxels shown in Fig. 3.34.

3.5.1.4 Effect of PTFE

The generated structure contains 9 % solid volume fraction PTFE and is in the generally accepted range for useful PTFE loadings. Additional loadings only further reduce porosity without the benefit from reduction in saturation as is observed for initial loadings. The porosity of the PTFE treated GDL was calculated directly from the model as described in §3.4.1 to be 72.8 % yielding a reduction of 2.5 %. The change in porosity as a function of PTFE wt.% loading can be written as:

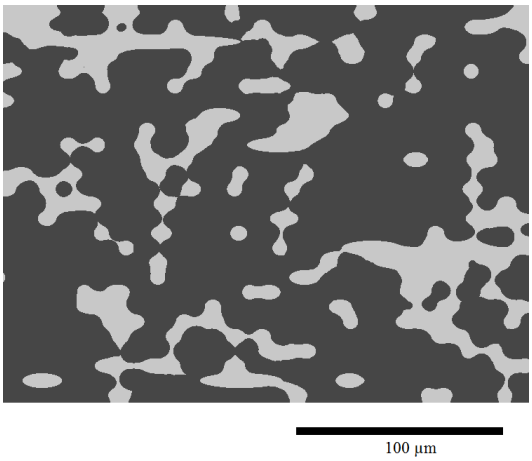

(a) Simulated Toray TGP-H-060 with 0 wt.% PTFE

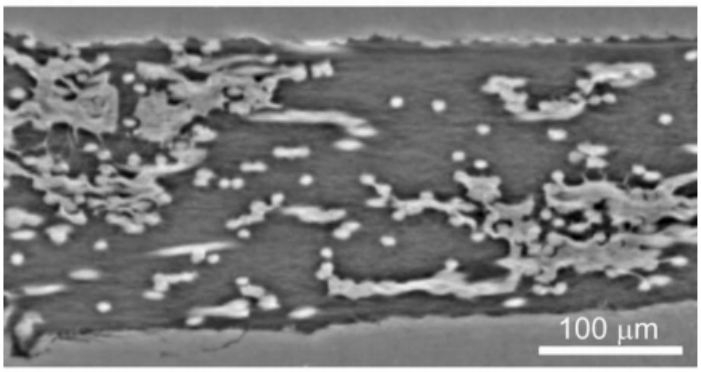

(b) Actual Toray TGP-H-060 with 0 wt.% PTFE [32]. Reprinted with permission from *J. Electrochem. Soc.* **156** (10) B1175-B1181 (2009). Copyright 2009, The Electrochemical Society.

Figure 3.33: 2D Comparison of the binder distribution of the generation algorithm to actual GDL.

$$\Delta\epsilon = \frac{wt.\,\%\,\text{PTFE}}{1 - wt.\,\%\,\text{PTFE}} \cdot (1 - \epsilon_o) \cdot \frac{\rho_{carbon}}{\rho_{PTFE}} \tag{3.7}$$

where ϵ_o is the original (untreated) GDL porosity, ρ_{carbon} is the density of the carbon, and ρ_{PTFE}. Equation 3.7 does incorporate the reasonable assumption that the carbonized binder and graphitized fibers have equal densities ($\rho_{carbonbinder}$ = 1.7 g/cm^3 $\approx$ $\rho_{graphitefibers}$ = 1.9-2.0 g/cm^3 [9]. Assuming the density of the carbon and the PTFE in the GDL are nearly equivalent, 9 wt.% PTFE treatment would reduce the original porosity of 75.3 % to 72.9

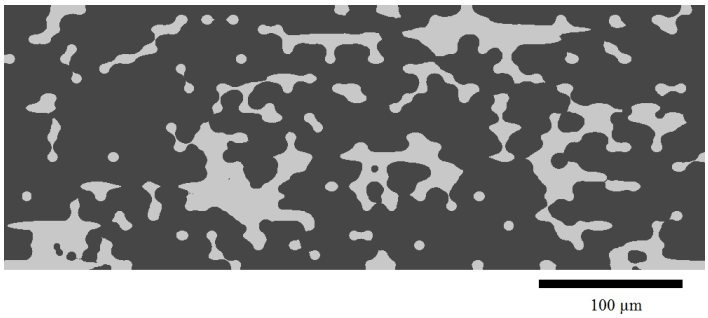

Figure 3.34: Simulated Toray TGP-H-060 with 0 wt.% PTFE showing the fiber and binder distributions similar to an actual GDL shown in Fig. 3.33(b).

% yielding a reduction of 2.4 % which is in agreement with the 2.5 % reduction calculated directly from the model. Experimental measurements of porosity using the method of mercury intrusion porosimetry also found a reduction of porosity 2.4 % for untreated and 10 wt.% PTFE treated GDLs [211]. The reduction of porosity for the structure with 5 wt.% PTFE (1/2 μm voxels) was computed to be 1.03 % from the digital models. This is in agreement with the expected value of 0.98 % from Eq. 3.7 using an initial porosity of 81.34 % prior to the PTFE loading.

3.6 Summary

A numerical simulation tool was developed that provides the 3D geometry of GDL materials with localized binder and PTFE distributions. This tool was developed using a new model and framework for the digital generation of GDL materials and was successful in producing realistic GDL geometries using 3D morphological image processing. The 3D morphological processing mimicked manufacturing processes of the addition of binder material and subsequent PTFE treatments. The overall generation algorithm allows for intuitive user inputs of the desired physical GDL materials (e.g. fiber radius, porosity, etc.) through a GUI developed in MATLAB. The outputs from the generation algorithm were the global porosity, volume fraction of binder, volume fraction of PTFE, and a 3D phase-

differentiated image. The output 3D image was an indexed image where void, fiber, binder, and PTFE were represented by 0, 1, 2, and 3, respectively. This phase-differentiated image could be written to the MATLAB workspace as a 3D array or as a multi-page tiff image saved to the local disk. The 3D geometry can then be used in commercial CFD software packages for transport simulation studies. The generated GDL materials were also characterized by the local porosity variations throughout the structure through an additional function of the toolbox. The local porosity function allowed for examination at any user-defined scale throughout the generated GDL structure. The generation algorithm was in agreement with CLSM images and X-ray characterization of commercial GDL (Toray TGP-H-060) using input parameters from manufacturer data. This generation algorithm implemented in a MATLAB toolbox framework will provide 3D geometries of commercial or hypothetical GDL materials in a cost- and time-effective manner for modeling efforts.

Chapter 4

Through-plane Visible and IR Imaging of a PEMFC

4.1 Infrared Imaging

Infrared (IR) radiation is a regime of the electromagnetic (EM) spectrum that approximately spans from λ = 780 nm to λ = 1 mm. This IR regime is routinely divided into smaller regimes such as: near infrared (0.78 μm $\leq \lambda \leq$ 1.0 μm), short-wave infrared (1.0 μm $\leq \lambda \leq$ 3.0 μm), mid-wave infrared (3.0 μm $\leq \lambda \leq$ 5.0 μm), long-wave infrared (7.0 μm $\leq \lambda \leq$ 14.0 μm), and very-long wave infrared (15.0 μm $\leq \lambda \leq$ 1 mm). There is not a universally accepted breakdown of these bands and subtle changes to the classifications are made based on the particular discussion. In this work, mid-wave infrared imaging was conducted and will be defined as wavelengths between 3.0 μm and 5.0 μm and will be exclusively used for IR imaging. This EM radiation was collected, focused with a microscope lens, and quantified with an IR camera to obtain high resolution non-invasive temperature measurements across GDLs in a PEMFC.

4.1.1 Blackbody Radiation

It is well-known that all matter above absolute zero emits IR radiation with intensity and wavelength dependent on temperature. Planck's Radiation Law describes this spectral EM emission or exitance for idealized surfaces that perfectly absorb and re-emits all incident EM radiation [212]. The spectral exitance from ideal surfaces referred to as blackbody or Planck radiation can be written as:

$$M(\lambda) = \frac{2\pi hc^2}{\lambda^5(e^{\frac{hc}{\lambda kT}} - 1)} \tag{4.1}$$

where h is Planck's constant (6.63 x 10^{-34} J·s), c is the speed of light (3.0 x 10^8 m/s), k is Boltzmann's Constant (1.381 x 10^{-23} J/K), and T is absolute temperature. Integration of Eq. 4.1 over all wavelengths results in the only closed form solution for the total exitance and is given by the Stefan-Boltzmann equation:

$$M = \sigma T^4 \tag{4.2}$$

where σ is the Stefan-Boltzmann Constant (5.67 x 10^{-8} $\mathrm{Wm}^{-2}K^{-4}$). It is the blackbody emission from the cross-section of the GDL that will be used to measure the temperature gradient in the through-plane direction.

4.1.2 Radiometric Definitions

To facilitate the development of an expression to describe the total irradiance on the sensor of the IR camera, some radiometry definitions will be introduced and were adopted from Schott 2007 [213]. Since ideal blackbodies do not exist, the concept of emissivity is used to describe the ratio of the energy emitted by an object ($M_\lambda(T)$ to the energy emitted by a blackbody $M_{\lambda,BB}(T)$ at the same temperature and is defined as:

$$\epsilon(\lambda) = \frac{M_\lambda(T)}{M_{\lambda,BB}(T)} \tag{4.3}$$

In addition to the emitted light from a surface due to non-zero absolute temperature, the total amount of light leaving the surface is a function of the amount absorbed (α), reflected (ρ), and transmitted (τ) from the surrounds. Absorption can be defined as the unitless ratio of the amount of EM flux absorbed (M_α) (i.e. converted into another form of energy) to the amount of EM flux incident on the surface (E_i) and is given as:

$$\alpha = \frac{M_\alpha}{E_i} \tag{4.4}$$

The reflectivity of a surface is defined as the unitless ratio of the amount of EM flux leaving the surface to the amount of EM flux incident on the surface:

$$\rho = \frac{M_\rho}{E_i} \tag{4.5}$$

The transmission of a surface is defined as the unitless ratio of the amount of EM flux incident leaving surface to the amount of EM flux incident on the back of the sample:

$$\tau = \frac{M_\tau}{E_i} \tag{4.6}$$

Using the above definitions of optical properties of a material, conservation of energy can be written as:

$$\alpha + \rho + \tau = 1 \tag{4.7}$$

This form of conservation of energy can be related to the object's emissivity through Kirchhoff's Law which states that the emissivity of an object must be numerically equivalent to its absorbance when in thermodynamic equilibrium. Combining Kirchhoff's law with conservation of energy we have:

$$\epsilon + \rho + \tau = 1 \tag{4.8}$$

4.1.3 IR Imaging for Temperature Measurement

Infrared cameras measure the irradiance on the sensor at each pixel location to build a two-dimensional image of the radiant EM energy captured. These digital counts are first converted to radiance values using a radiometric calibration typically conducted by the manufacturer in a calibration laboratory. In order to obtain temperature measurements from the radiance values, a radiometric model of the imaged scene is needed. The total irradiance on the sensor can be written as:

$$M_{Total}(\lambda) = \epsilon_{Object}\tau_{Atm}M_{Object}(\lambda) + \rho_{Object}\tau_{Atm}M_{Ambient}(\lambda) + \epsilon_{Atm}M_{Atm}(\lambda) \tag{4.9}$$

where the first term is due to emission of the object, the second term is due to the object's reflection from ambient sources, the last term is the emission of the atmosphere, and each are attenuated by the atmosphere. Using Eq. 4.8 and assuming that τ = 0 for an opaque material, the reflectance of the object can be written as: $\rho = 1 - \epsilon$. Furthermore, the emissivity of the atmosphere can be written as $\epsilon_{Atm} = 1 - \tau_{Atm}$ through Eq. 4.8 and assuming ρ_{Atm}= 0. The total energy incident on the sensor can now be written as:

$$M_{Total}(\lambda) = \epsilon_{Object}\tau_{Atm}M_{Object}(\lambda)+(1-\epsilon)\tau_{Atm}M_{Ambient}(\lambda)+(1-\tau_{Atm})M_{Atm}(\lambda) \tag{4.10}$$

Thus, the radiant energy measured by the sensor can be described by the object emissivity, atmosphere transmission and temperature, and the temperature of the surroundings. These parameters can be obtained through preliminary measurements and real-time atmospheric conditions during image capture and are discussed in §4.5.1.1. Using this model,

the object temperature can be determined. When an IR transparent window is used, an additional attenuation (τ_{Window}) and emission (1-τ_{Window}) terms are added Eq. 4.10 and can also be measured in preliminary measurements and real-time temperature measurements (§4.5.1.1). This radiometric model is typically incorporated into IR camera software such a FLIR ExaminIR^{TM}Max for thermography studies.

4.2 Transparent PEMFC Design

A PEMFC was designed to allow for simultaneous visible and mid-wave infrared (3.0 μm $\leq \lambda \leq$ 5.0 μm) transmission through an observation window to reveal the cross-sections of the cathode and anode GDLs and channels. As shown in Fig. 4.1, the graphite flow field of a commercial 50 cm^2 fuel cell hardware was modified to accommodate the window. The cathode channels were triple serpentine channels, each 0.7 mm deep and 0.9 mm wide with 0.7 mm lands, and the anode channels were double serpentine channels, each 1.0 mm deep and 0.8 mm wide with 0.7 mm lands. In order to reveal the GDL cross-sections, the cathode and anode lands were recessed by 180 μm to represent the compressed thickness of the GDLs used in this study. Sapphire was chosen as the window material for its high transmittance of visible (0.4 μm $\leq \lambda \leq$ 0.7 μm) as well as mid-wave infrared light. A pocket was machined into the side of the flow fields to hold the sapphire window flush with the unmodified flow field perimeter. The modifications were mirrored onto the anode flow field allowing for simultaneous observation of cathode and anode water flow structures. The endplates were machined to match the modified flow fields and to allow for the short working distance of the infrared microscope lens. A schematic of the assembled visualization cell with a close-up of the expected microscopic view shown in Fig. 4.2.

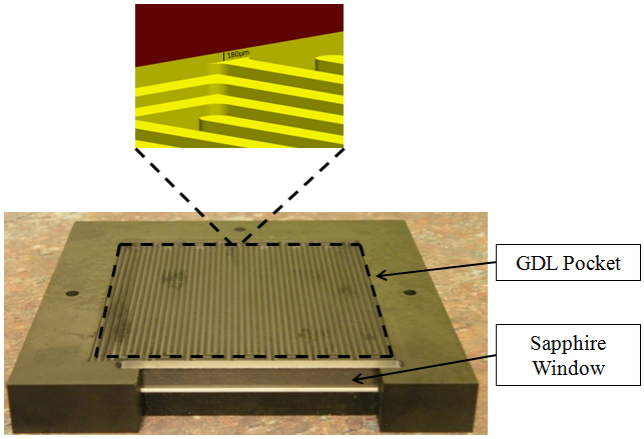

Figure 4.1: Modified cathode flow field to accommodate the compressed thickness of the GDL and placement of sapphire window. Reprinted with permission from *Electrochem. Solid St.* **14** (6) B51-B54 (2011). Copyright 2011, The Electrochemical Society.

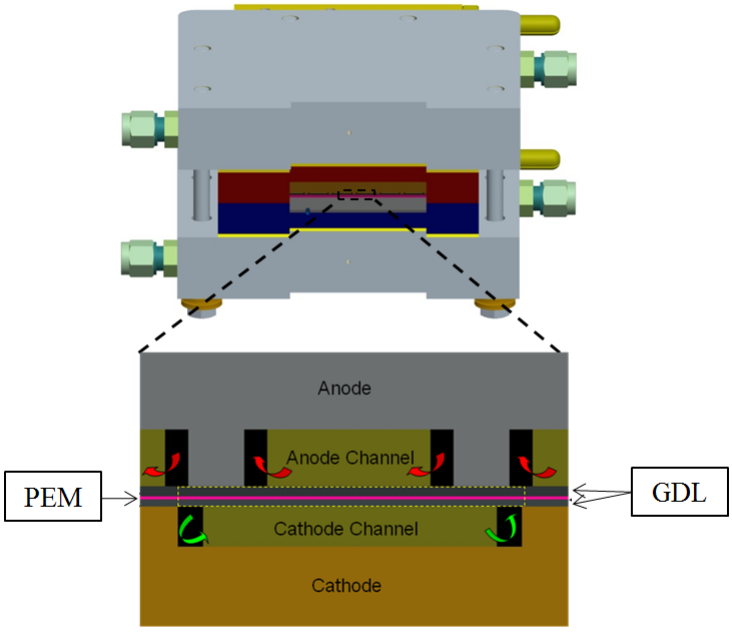

Figure 4.2: Schematic of assembled PEMFC with the expected view of the cathode and anode cross-sections. Reprinted with permission from *Electrochem. Solid St.* **14** (6) B51-B54 (2011). Copyright 2011, The Electrochemical Society.

4.3 Imaging Systems

The visualization systems consisted of a Keyence VHX-500 digital microscope and a FLIR SC 6000 infrared camera. The Keyence VHX-500 uses a 1600 x 1200 color CCD focal plane array and is capable of frame rates of 15 and 28 fps. A long working distance (85 mm) lens with an adjustable magnification ranging from 50-500x (based on displaying images on a 15 inch monitor) was used with the digital microscope for all experiments. The FLIR SC 6000 infrared camera uses a 640 x 512 InSb focal plane array with a pixel pitch of 25 μm and is sensitive to mid-wave infrared (3.0 μm $\leq \lambda \leq$ 5.0 μm). The FLIR SC 6000 infrared camera was equipped with infrared microscope lenses with magnifications ranging from 1x-5x (based on image magnification) and capable of full frame rate up to 126 fps and higher at reduced resolutions. An infrared microscope lens with a 5x image magnification yielding a 5 μm pixel resolution was used for all infrared observations.

4.4 Through-plane Visible Imaging in a PEMFC

4.4.1 PEMFC Materials and Testing Conditions

The catalyst coated membrane was based on an 18 μm thick Gore membrane and had a Pt loading of 0.3 mg/cm^2 in both anode and cathode catalyst layers. The GDL material was MRC (Mitsubishi Rayon Co.) 105 treated with PTFE and coated with an in-house MPL by General Motors. In all experiments, dry clean hydrogen and air produced on-site from Parker Balston hydrogen and zero grade air generators were supplied to anode and cathode channels in a counter flow configuration: no external humidification was provided for either the hydrogen or air flows. The fuel cell was operated at ambient temperature and pressure under a constant stoichiometric ratio of An/Ca = 2.0/3.0. The preliminary test revealed a comparable performance (IV curve) to the standard 50 cm^2 cell, indicating that the addition of the sapphire windows had little influence on the overall performance.

4.4.2 MRC (Mitsubishi Rayon Co.) 105 Results and Discussion

4.4.2.1 Simultaneous Anode and Cathode Channel Visualization

Although fuel cell cathode and anode flow channels have been visualized previously, this is typically done in separate experiments [76, 214]. In this work, simultaneous visualization of anode and cathode channels at various magnifications was obtained for the first time. Figure 4.3 shows the cross-section of the PEMFC under loads of 0.05 A/cm^2, 0.30 A/cm^2, 0.70 A/cm^2, and 1.10 A/cm^2. Cross-section images at higher current densities were excluded due to the increased cell temperature and the change of the phase transition into the channels. Several important observations can be made from this figure. First, under lower current densities, only a small amount of water accumulated in the cathode channels, while there was a significantly greater amount of water in the form of water films along the flow channels on the anode side. This is in agreement with the neutron radiography studies of Owejan et al. [5]. At a given current density, the greatest amount of condensation in the anode channels occurred towards the anode inlet. Note that for all current densities the air and hydrogen inlet streams had no external humidification. Therefore, the water that was observed in the cell anode was product water from the cathode catalyst layer that traversed the CCM. The water that transported from the cathode to anode appeared as condensation on the sapphire window and under no operating conditions were droplets observed to emerge from the anode GDL as was routinely observed in the cathode. The greater concentration of condensation in the anode toward anode inlet was a result of the reactant counter flow configuration and reactant inlet RH. A dry air stream begins to pick up product water in the vapor phase as it travels through the cell until saturation, where the vapor will begin to condense. The amount of water in the cathode channel increases as a function of the distance from the cathode inlet with the greatest accumulation occurring near the cathode outlet. Thus, the greatest concentration of water on the cathode to transport to the anode will occur towards the anode inlet (in a counter flow configuration). The location where

the anode condensation was observed migrated toward the anode outlet as a function of current density, further implicating this mechanism. The migration of the condensation toward the anode outlet was due to the increased water production in the cathode which provided a greater amount of water activity in the cathode at locations further upstream which then could traverse the CCM. The condensed water in the anode accumulated on the window and was periodically removed by water films and slugs on the graphite and sapphire surfaces (See Fig. 4.3(c)).

Secondly, liquid water appears in anode channels mostly via condensation mechanism instead of liquid water transport through the anode GDL. A similar phenomenon has been reported at a higher temperature of 80°C [87]. This finding indicates that water flooding and the consequent mass transport resistance in the anode is not as serious as in the cathode because liquid water does not accumulate inside the porous GDL and block the hydrogen pathways. In contrast, liquid water in cathode channel appears through both condensation mechanism and liquid water transport through GDL.

4.4.2.2 GDL Cross-section Observation

The primary objective visible imaging portion of this work was to observe the GDL cross-section in an operating PEMFC. Therefore, the anode and cathode GDLs were visualized at higher magnification with a digital microscope. The higher magnification imaging routinely revealed water droplets on the GDL cross-section for current densities above 0.85 A/cm^2. For example, a droplet near the cathode inlet maintained its size and location at lower current densities but increased in size with increasing current density and was occasionally wicked to the sapphire window. The droplet ceased to emerge from the GDL at current densities above 1.8 A/cm^2, due to increased gas shear and vapor transport of the gas stream. Since condensation was not observed in the droplet formation area, the water droplet was apparently not formed from vapor condensation. Instead, it had emerged as liquid water transported from inside the GDL, indicating that water was condensed in the

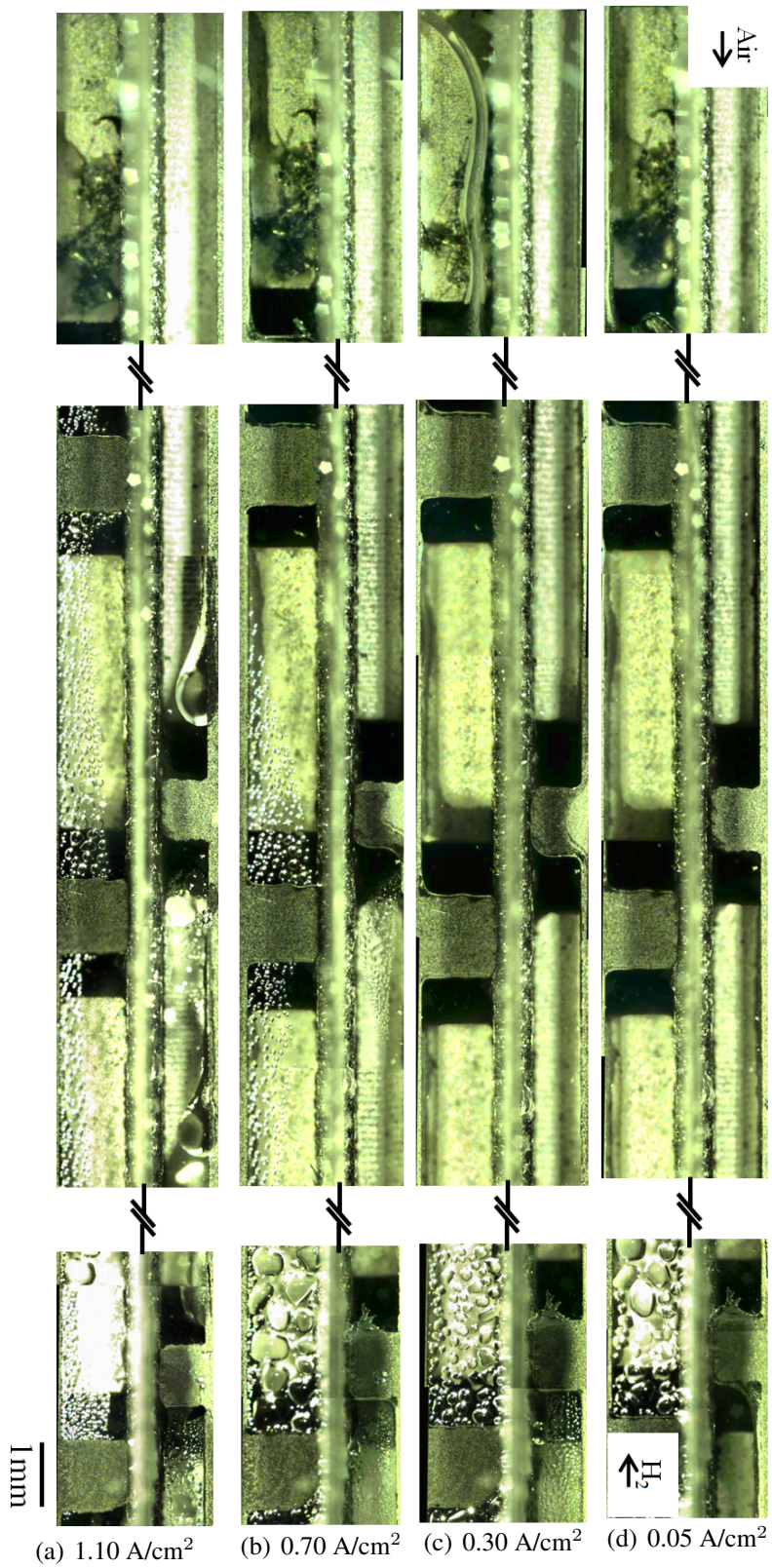

Figure 4.3: Cross-section of transparent PEMFC as a function of current density. Reprinted with permission from *Electrochem. Solid St.* **14** (6) B51-B54 (2011). Copyright 2011, The Electrochemical Society.

GDL and transported out via capillary flow.

In another experiment, in order to increase the cross-section of the observed GDL, an additional layer of Toray TGP-H-060 10 wt.% PTFE was used on the channel side of the cathode MRC GDL. At a current density of 0.4 A/cm^2, water droplets emerged from the GDL and wicked onto the window and channel walls where they were removed by the gas shear. At one droplet formation site, small droplets appeared to be condensing on the GDL cross-section. To isolate the small droplets, the cell was returned to OCV and the cell was purged on the cathode until all water was removed. The load was then returned to 0.4 A/cm^2 and the cross-section was continuously monitored. The condensing small droplets returned to the site within a minute. In order to isolate the condensation, the video was processed using image subtraction and subsequent thresholding. An initial color image of the dry GDL cross-section (Fig. 4.4(a), obtained after purge) was subtracted from each subsequent frame (e.g. see Fig. 4.4(b)), resulting in a difference sequence. A minimum change in intensity (threshold) was applied to the difference sequence to identify potential water detection locations. These pixels were defined as water detection locations (Fig. 4.4(c)) if potential detection occurred independently on at least two color planes. Finally, to give spatial reference (w.r.t. the GDL cross-section) to the binary water detection frames, the initial dry grayscale image was added to the water detection frames (Fig. 4.4(d)). Example images of dry, wet, water detection, and water detection with the GDL cross-section are shown in Fig. 4.4, respectively. These results demonstrate that the water droplets and transport on the cross-section of the GDL can be captured with a digital microscope and quantified with video processing. More interesting is that water condensation inside GDL is implied. However, in current design, the MPL and catalyst layer could not be observed, and thus no implicit conclusions on the location of the condensation site or the consequent condensation front were obtained. The design of a new setup allowing the observation of the MPL at higher magnification is recommended for future work.

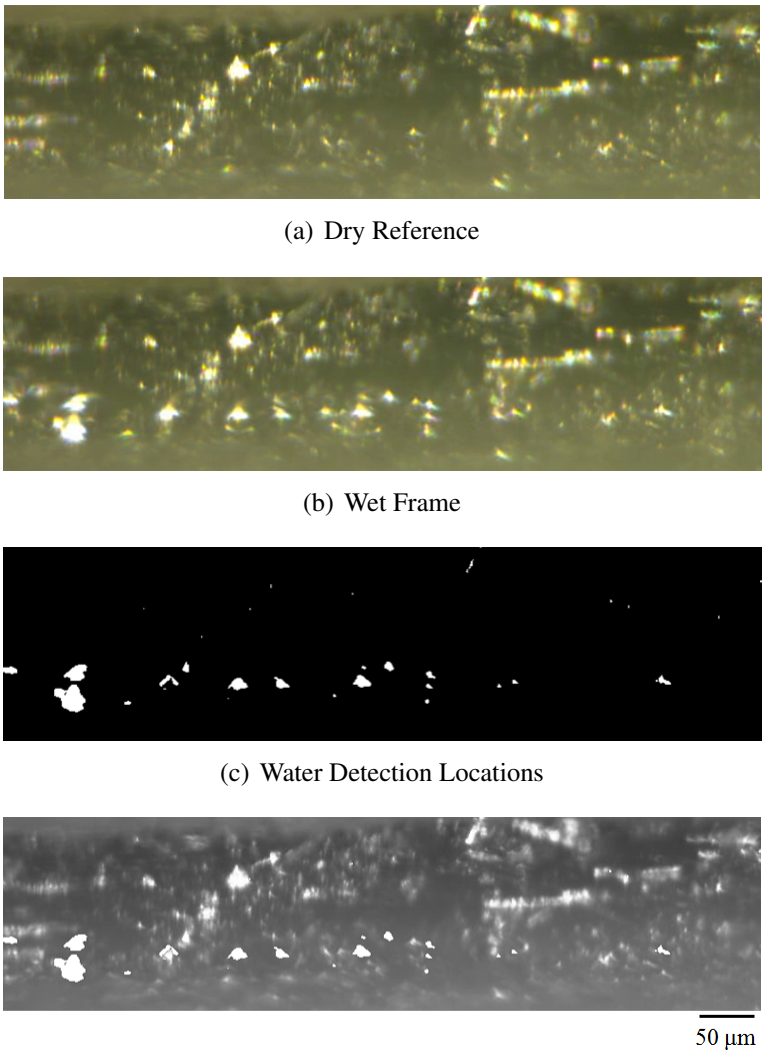

(a) Dry Reference

(b) Wet Frame

(c) Water Detection Locations

(d) Water Detection with GDL

Figure 4.4: Visualization of water on the cathode GDL cross-section at j=0.4 A/cm^2 revealed using digital video processing. Reprinted with permission from *Electrochem. Solid St.* **14** (6) B51-B54 (2011). Copyright 2011, The Electrochemical Society.

4.5 Through-plane Infrared Imaging in a PEMFC

4.5.1 Infrared Calibration

The infrared camera used in this study was a FLIR SC 6000 and has custom manufacturer calibrations for each lens and specific temperature ranges to correlate the digital counts captured by the InSb focal plane array to temperature measurements. In addition to the camera general calibration, material and test section specific calibrations must be conducted for reliable temperature measurements. Specifically, the material emissivity and window transmittance need to be measured. This measurement or "calibration" was conducted with two ex situ test setups: (1) the GDL cross-section without the sapphire window and (2) the GDL cross-section with sapphire window. The GDL emissivity was first determined in the absence of the window and then the transmittance of the window was determined by placing the window between the lens and the GDL.

4.5.1.1 Experimental Setup and Procedure

A general schematic to the experimental setup is shown in Fig. 4.6 where the GDL sample was sandwiched by two pieces of graphite with heaters on opposite sides. The heaters were used to raise the GDL temperature above ambient to mitigate influence of IR reflections from the surroundings. The heaters were Watlow flexible silicone heaters and power supplied was controlled by a four zone proportional-integral-derivative controller (Omega CN1504-TC). Each graphite block had a thermocouple port for a K-Type thermocouple that used for the setpoint for the respective controller. The accepted GDL temperature was measured using a T-Type micro-thermocouple (RTD Company PN12454-3, 200 μm bead including insulation) labeled TC3 in Fig. 4.6) and was read with Omega HH23A digital thermocouple reader. Once steady-state ($\Delta T \leq 0.1^{\circ}$C) of TC3 was achieved, the GDL was imaged with a 5X lens. Significant variations in the temperature measured by the IR camera were observed due to changes in emissivity (heterogeneous GDL material) and geometry.

The in-plane temperature variation at room temperature without the PEMFC running was examined by extracting the temperatures from the center of the GDL cross-section. The resulting plot of a single pixel width (5 μm) across the field of view is shown in Fig. 4.5. The plot in Fig. 4.5 shows the significant effect of geometry and emissivity can have temperature measurements. This issue was resolved by using an averaging technique to determine the effective emissivity. An area of 6.8 mm^2 was used for averaging at two locations for each set point temperature. Using the FLIR ExaminIR^{TM}Max software, the emissivity of the GDL was determined by estimating the effective emissivity and evaluating the resulting temperature. The effective emissivity was changed until the resulting temperature was consistent with the thermocouple temperature. This procedure was repeated for 43, 53, and 60°C set points at both locations for each GDL. Once the GDL emissivity was measured, the window was placed in the experimental setup between the lens and GDL to measure its transmittance.

Similar to the procedure used to measure the GDL emissivity was used to measure the transmittance of the window utilizing the ExaminIR^{TM}Max software. The transmittance of the window was estimated and the resulting temperature (Possible with the effective emissivity of the GDL sample) was compared to the thermocouple reading. The transmittance of the window was adjusted such that GDL temperature was consistent with the thermocouple. This was repeated for the set point temperatures of 43, 53, and 60°C.

4.5.1.2 Results

The emissivities of Toray TGP-H-120 treated with PTFE and coated with an in-house MPL by General Motors and commercially available Sigracet SGL 10BC were measured at two locations, three temperatures, and averaged. Example images from the 43° set point are shown in Fig. 4.7 with the microthermocouple labeled (TC3) and the averaging area for emissivity and transmittance measurements outlined in red. The effective emissivities were found to be 0.84 and 0.86 for Toray TGP-H-120 and SGL 10BC, respectively. Following

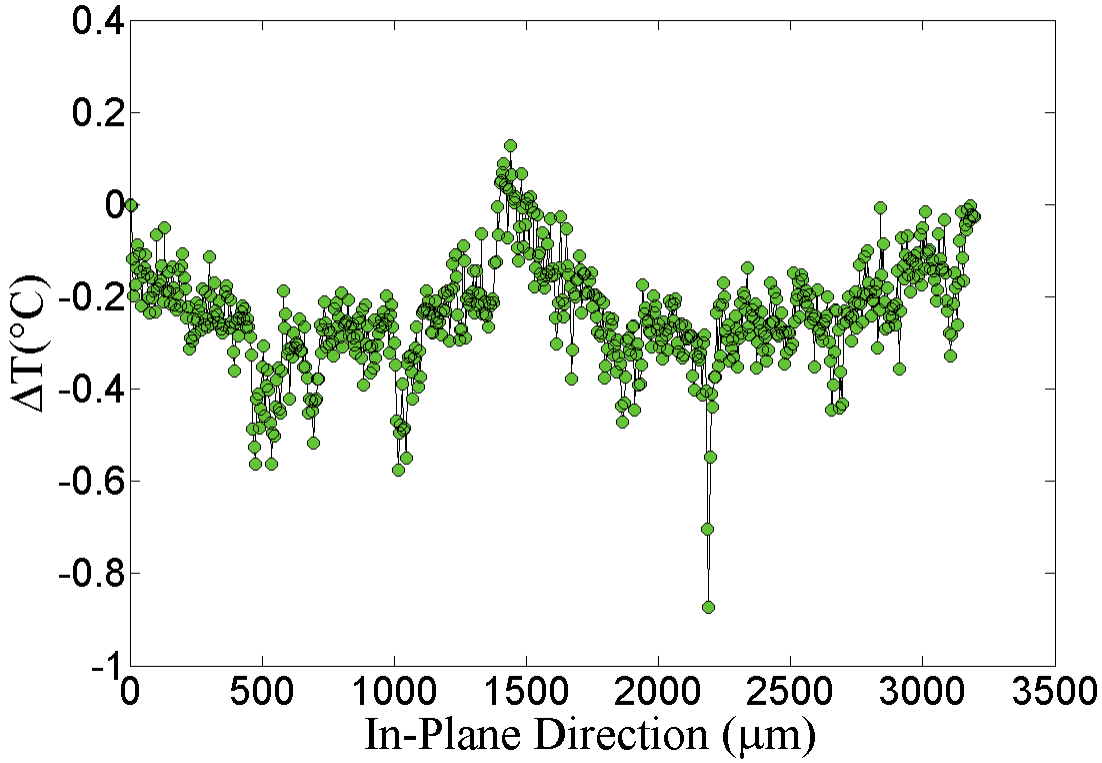

Figure 4.5: In-plane temperature variation across the center of the cathode GDL at room temperature due to changes in emissivity and geometry.

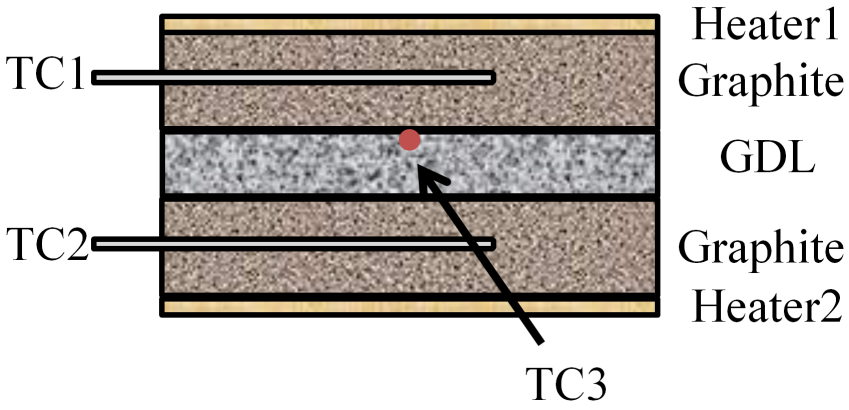

Figure 4.6: Schematic of emissivity and window transmittance measurement test section. Not to scale.

the emissivity calculation, the average window transmittance was measured to be 0.77.

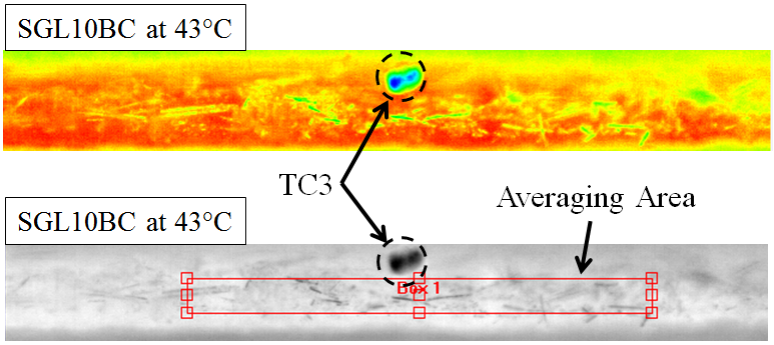

Figure 4.7: Example calibration images showing microthermocouple (TC3) and averaging area (Box 1).

4.5.2 PEMFC Materials and Testing Conditions

Two gas diffusion layers, Toray TGP-H-120 with an in-house MPL by General Motors and commercially available Sigracet GDL 10BC were studied in this work. Both GDLs were carbon paper based and treated with PTFE. The CCM used for both GDLs was based on an 18 μm thick Gore membrane with 0.3 mg/cm^2 Pt loading on both the anode and cathode. In all experiments, dry, clean hydrogen and air were supplied in a counter flow configuration. The fuel cell was operated at 60°C at ambient pressure under a constant stoichiometric ratio of An/Ca = 2.0/3.0.

4.5.3 Ex Situ Temperature Distribution Validation

The main objective of this in situ work was to measure the temperature gradient across the GDL in an operating PEMFC. To validate the temperature gradients measured during cell operation, ex situ experiments were conducted with the assembled PEMFC to measure the gradients in the absence of a heat flux and with an imposed gradient. In addition to the measurements of material emissivity and window transmittance, consideration for imperfections in window fabrication were taken. The manual grinding process used to machine the sapphire to the size of the pocket in the graphite flow field created cracks (and chips on the outer surfaces) that created significant reflection surfaces. An example image of the

cracks as viewed from the surface can be seen in Fig. 4.8(a). The central white region of uniform thickness in Fig. 4.8 is where the membrane comes out between the windows to separate the anode from the cathode. This membrane region is shown in white because it is out of focus and is thus an invalid area for temperature measurement. The influence of both the cracked/chipped region and membrane were accounted for by restricting all temperature measurements outside of this region and is shown with horizontal black lines in Fig. 4.8(b). The anode and cathode GDLs were isolated by locating their surfaces in the gas distribution channels and is shown in Fig. 4.8(d) with white horizontal lines.

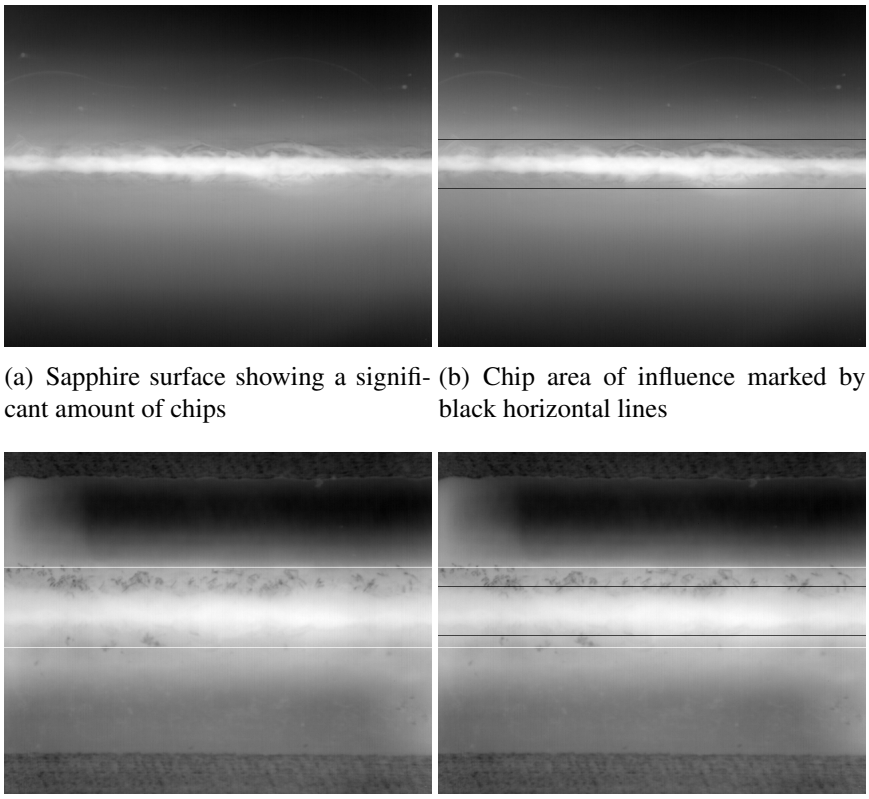

(a) Sapphire surface showing a significant amount of chips

(b) Chip area of influence marked by black horizontal lines

(c) Cross-section of PEMFC with GDL surfaces marked by white horizontal lines

(d) Cross-section of PEMFC with valid temperature measurement area bounded by GDL surface and chips

Figure 4.8: Preprocessing steps required to isolate GDL cross-section from the influence from sapphire imperfections.

4.5.3.1 Room Temperature Results

The temperature measurements in the IR images are dependent on a factory calibration (lens dependent) to map the digital counts to radiance and a "calibration" of the object in terms of object and scene specific properties such as emissivity and transmittance. Furthermore, the factory calibration is dependent on exposure time and using the ExaminIR^{TM}Max software this cannot be adjusted if the FLIR software is to be used for thermography. As a solution to this software limitation, frame averaging was used to increase the signal to noise ratio in the acquired images. This improvement is apparent by visual inspection at room temperature because the peak emission of blackbody radiation (about λ = 10 μm) is outside of the camera's sensitivity. This effect is exemplified in Fig. 4.9 where the image in Fig. 4.9(a) is a single image and the image in Fig. 4.9(b) is the result of averaging 100 frames (captured at 30 fps) with the same exposure time (0.345 ms) as Fig. 4.9(a). This preprocessing step was conducted on all video data collected and is stated as such in the respective sections.

The temperature measurements in the running PEMFC were validated against measured gradients across the cathode GDL prior to fuel cell operation. Two locations where more than 100 micrometers of the GDL cross-section were identified as reliable and example images of location 1 and 2 are shown in Fig. 4.10(a) and 4.10(b), respectively. To mitigate temperature variation due to changes in geometry and to compute the average gradient in the through-plane direction, the temperatures within the GDL cross-section region were averaged in the in-plane direction. These temperatures were made relative by subtracting the initial temperature at the GDL channel surface from every averaged in-plane temperature. The result shown in Fig. 4.11 shows that the temperature variation without the PEMFC running is about 0.1 °C.

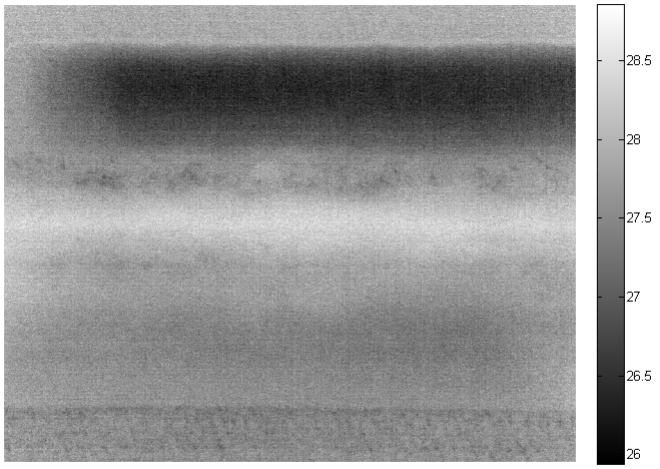

(a) Single frame of PEMFC cross-section at room temperature

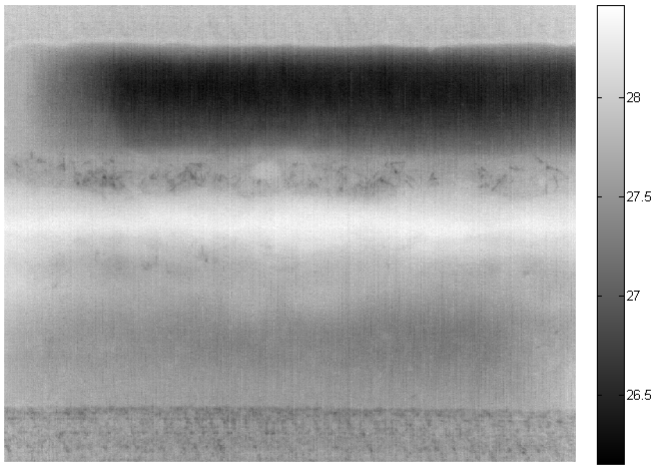

(b) Averaged frame of PEMFC cross-section at room temperature

Figure 4.9: Effect of frame averaging to increase signal-to-noise ratio.

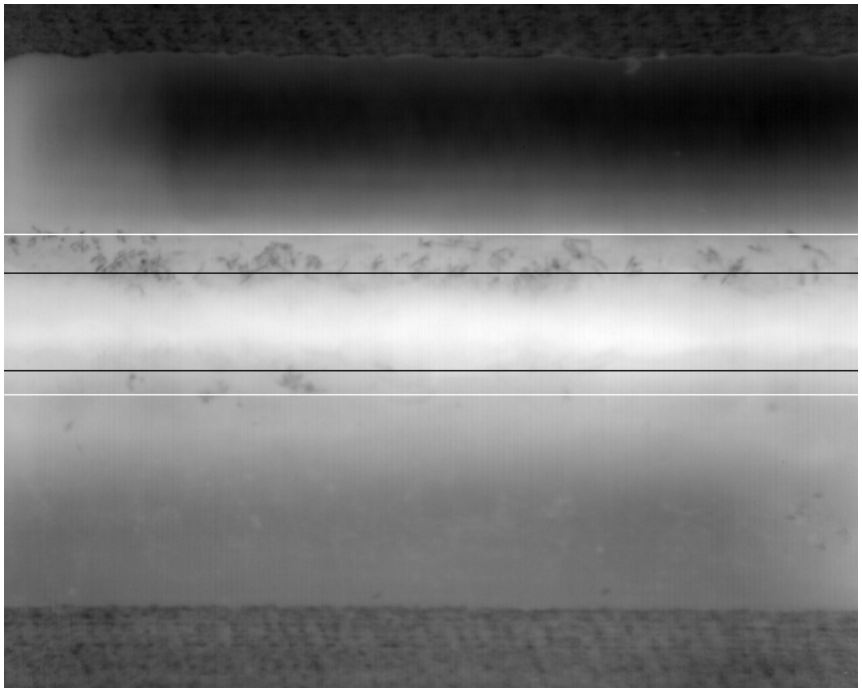

(a) Example (j=0.20 A/cm^2) image of location 1 (L1)

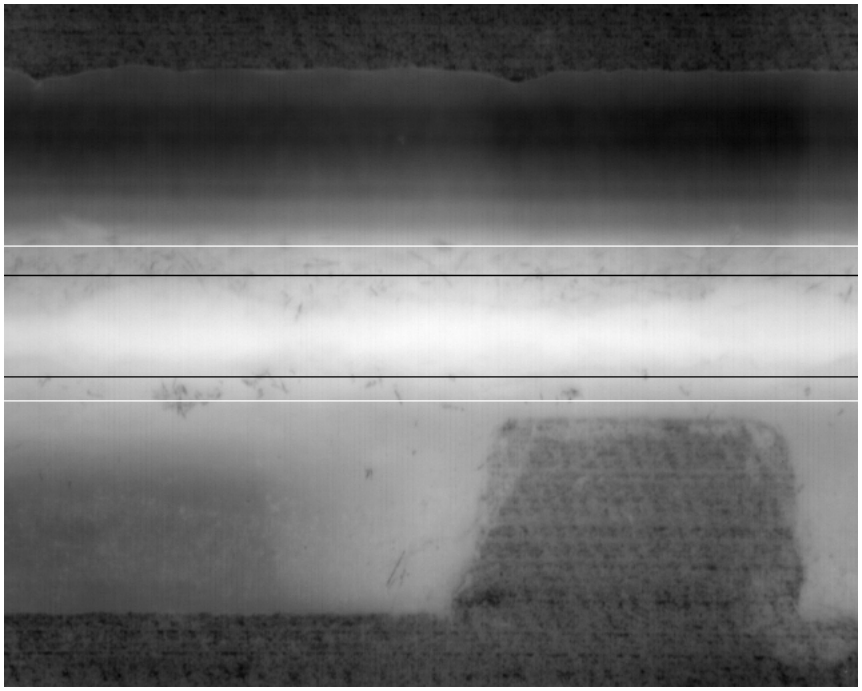

(b) Example (j=0.20 A/cm^2) image of location 2 (L2)

Figure 4.10: Reliable locations revealing significant cathode GDL cross-section between the GDL channel surface (white line) and the influence of the sapphire chips (black line).

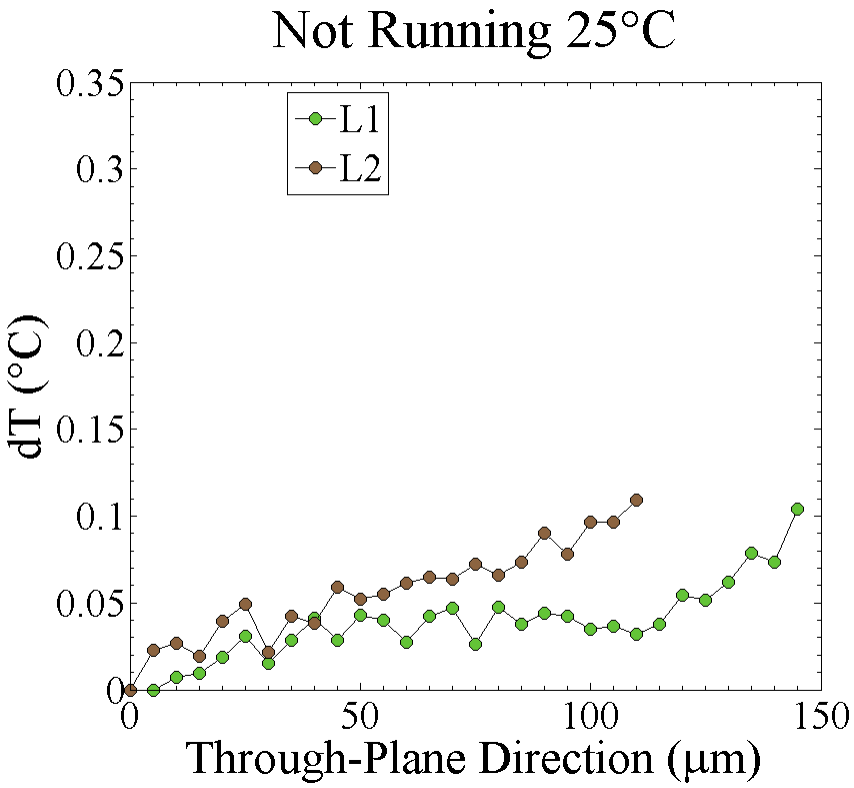

Figure 4.11: Temperature gradient across the cathode GDL (SGL 10BC) prior to running the PEMFC. Note the temperature gradient is about 0.1°C.

4.5.4 In Situ Temperature Gradient

4.5.4.1 SGL10 BC Results and Discussion

The transparent PEMFC was operated at a temperature of 60°C and infrared videos were taken at current density set points of 0.20, 0.30, 0.4, 0.50, and 0.60 A/cm^2. The polarization curve is shown in Fig. 4.12 and note that the high frequency resistance (HFR) remained constant at 0.09 Ωcm^2 through the test. Infrared videos were captured for about 3 sec at 30 fps (100 frames) with an integration time of 0.345 ms (factory set) and averaged to increase the signal to noise ratio. As with the validation testing discussed in section 4.5.3, to mitigate temperature fluctuation due to changes in geometry on the GDL cross-section, the temperatures were averaged in the in-plane direction across the entire 3.2 mm field of view in each pixel row (5 μm in the through-plane direction). The temperature gradient

across the GDL was obtained by subtracting the average GDL surface temperature from each mean through-plane temperature. The results of the temperature gradient vs. through-plane distance for location 1 across the cathode GDL are shown in Fig. 4.13. The zero through-plane distance represents the GDL channel surface. Notice the expected result of a linear increase in temperature as a function distance toward the catalyst layer. The PEMFC local geometry relative the cathode and anode lands of Location 1 is shown in Fig. 4.10(b) and it is worth noting that neither the cathode nor anode had a land present.

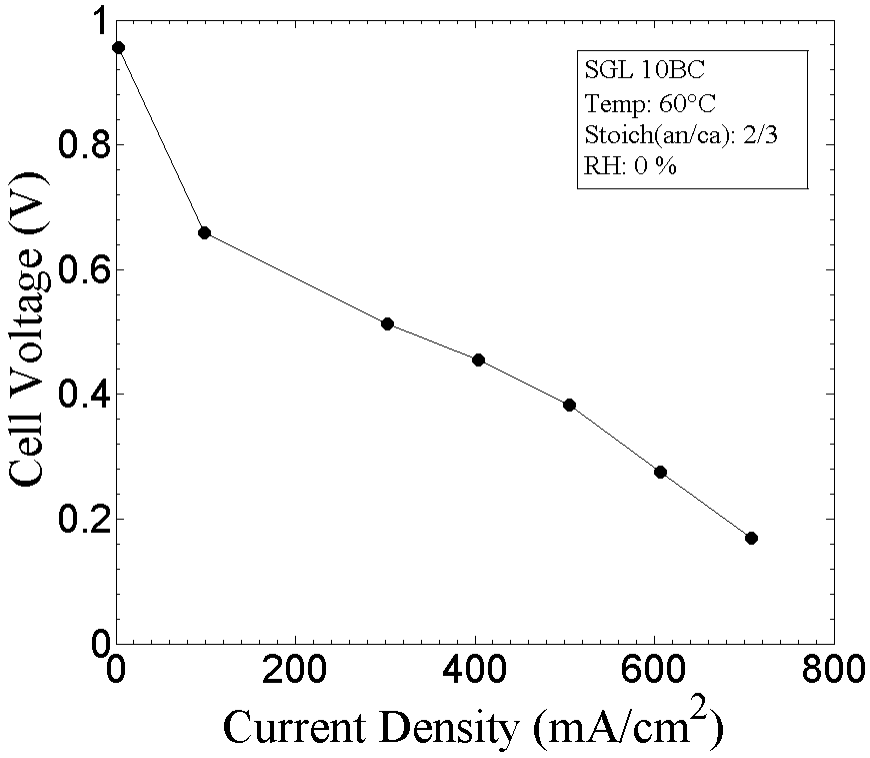

Figure 4.12: Polarization curve of transparent PEMFC with SGL 10BC at 60°C. Note the HFR remained constant at 0.09 Ωcm^2.

The PEMFC local geometry for location 2 was significantly different from the cell geometry of location 1. Note from Fig. 4.10(b) that there is an anode land toward the right side of the image. This attribute will have an effect on the local heat transfer by providing a conduction path of the generated heat to be removed from the CCM. Additionally, location 2 was about 21 mm from location 1 in the direction of the cathode outlet and anode inlet.

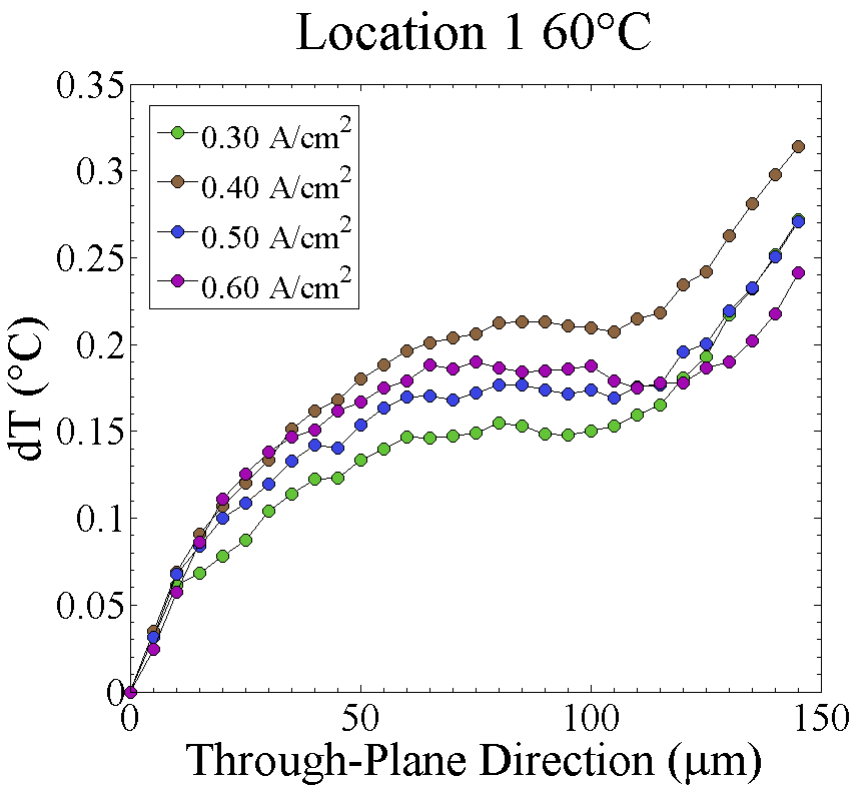

Figure 4.13: Average temperature gradient in the through-plane direction in the absence of lands for SGL 10BC at 60°C. Note distance zero corresponds to the GDL surface in the cathode channel.

The temperature gradient vs. through-plane direction across the cathode GDL for location 2 are shown in Fig. 4.14 with zero through-plane direction representative of the GDL surface. As expected, the temperature gradient is positive with the highest temperatures toward the catalysts layer. However, similar to the data measured from location 1, the current densities do not reveal any clear tread and thus warrant further analysis.

The heat generation in a PEMFC can be written as a function of the operating cell voltage and the ideal voltage:

$$q = j(E_{ideal} - E_{actual}) \tag{4.11}$$

where j is the current density, E_{ideal} is the ideal voltage (1.2 V), and E_{actual} is the cell voltage at current density j. Since heat transfer through the GDL materials is dominated by

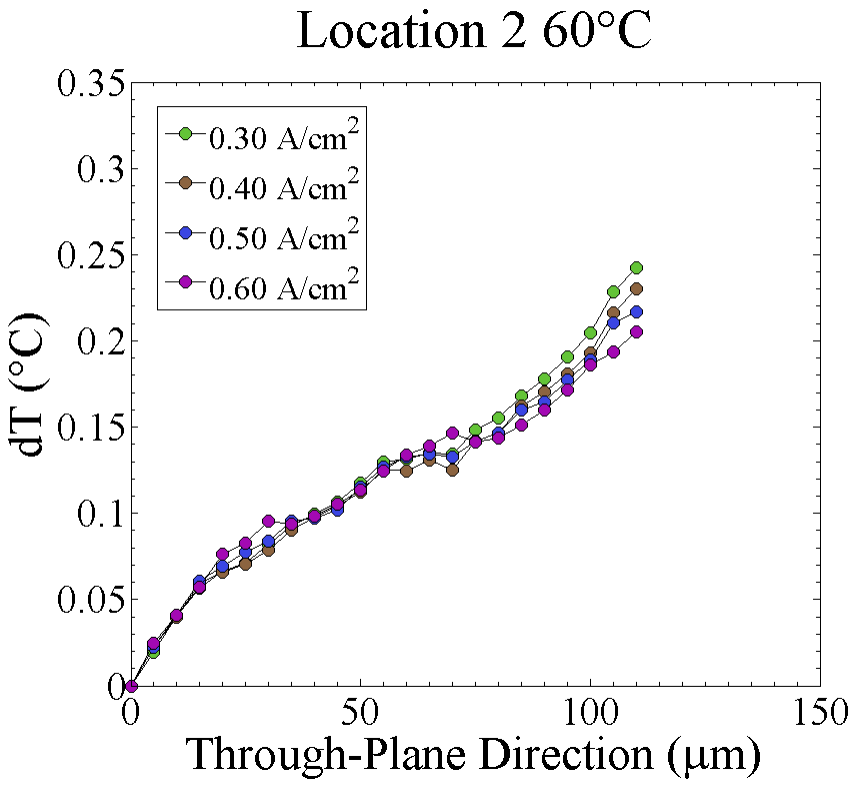

Figure 4.14: Average temperature gradient in the through-plane direction in the presence of an anode land for SGL 10BC at 60°C. Note distance zero corresponds to the GDL surface in the cathode channel.

conduction a simple 1D analysis is sufficient to estimate the temperature gradient across a GDL and thus we have:

$$q_x = -k_{gdl,x}\frac{dT}{dx}$$
$$\Delta T = q_x\frac{\Delta x}{k_{gdl,x}} \tag{4.12}$$

where $k_{gdl,x}$ is the thermal conductive of the GDL, T is temperature, and x is distance. Using Eq. 4.12 and the polarization data in Fig. 4.12 the heat generation was estimated. The temperature gradient across the cathode GDL was then predicted using the reported value of 0.65 W/mK for SGL 10BC [215] and assuming that heat was conducted away from

the cathode CL equally in both through-plane directions toward the cathode and anode. A linear regression was applied to the raw data shown in Figs. 4.13 & 4.14 to compare to the predicted gradients and was slightly extrapolated to increase the overall temperature difference. The results for location 1 are shown in Fig. 4.15 with the measured data shown as data points and the predicted gradients as solid lines. The predicted gradients show the expected tread of increasing as a function of current density due to the characteristic decrease in voltage (increased waste heat generation) of the polarization curve shown in Fig. 4.12. It is worth noting that were no lands in either the anode or cathode at location 1, as shown in the IR image of Fig. 4.10(a). The presence (or absence) of lands will significantly affect the localized heat transfer due to the direct conduction path into the flow field material. Note from the plot in Fig. 4.15 that the measured gradients are significantly less than expected from the 1D analysis. Similar results were obtained for location 2 and are shown in Fig. 4.16.

There are several important features of the plots shown in Figs. 4.15 & 4.16 of the measured and predicted temperature gradients. Firstly, both plots show a significant reduction in the measured temperature gradient compared to predicted values. The predicted temperature gradients assume a thermal conductivity of 0.65 W/mK as measured by Radhakrishnan which was for a dry and compressed SGL sample. In a running PEMFC, the cathode GDL transports water from the CL to the gas channels and if the water was present near the surface of the GDL cross-section, if would affect the GDL effective emissivity (ϵ_{water}=0.96) and therefore the IR temperature measurements. Furthermore, the distribution of water in the through-plane direction has been a significant challenge to predict or measure. The second feature of the measured temperature gradients was the effect of the sapphire window in contact with the GDL on the localized heat transfer. The thermal conductivity of sapphire is significantly higher than the through-plane conductive of GDL materials, e.g. 25 W/mK compared to around 1 W/mK. This effect further complicates the thermal analysis requiring a second dimension to the analysis that was not considered in

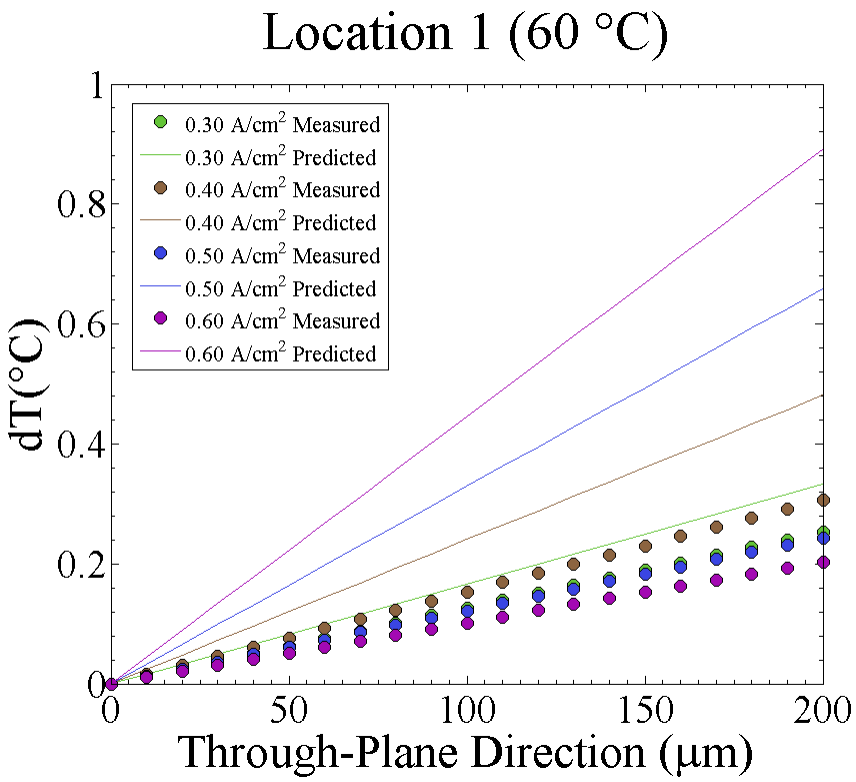

Figure 4.15: Linear regressions of the measured temperature gradients and predicted gradients for the cathode GDL (SGL 10BC) at location 1.

the 1D assumption. The heat that was transferred through the window would reduce the heat flux in the through-plane direction of the GDL and thus reduce the expected gradient. The last conclusion from the measured temperature gradients was the effect of the land regions on local heat transfer. It was assumed in the predicted temperature gradients that the generated heat flux was split equally between the anode and cathode of the cell which implies the thermal resistance in each direction was equal. A land in direct contact with the GDL surface provides significantly less thermal resistance than a channel region due to the thermal contact resistance of the GDL-land interface compared to the heat transfer coefficient of the GDL surface for typical gas temperatures and flow rates in operating PEMFCs. Thus when a land region is present on the anode side (location 2) and if the thermal conductivity of the GDL was uniform, more heat would be transferred to the anode side compared to the cathode. This would reduce the heat flux in the cathode direction

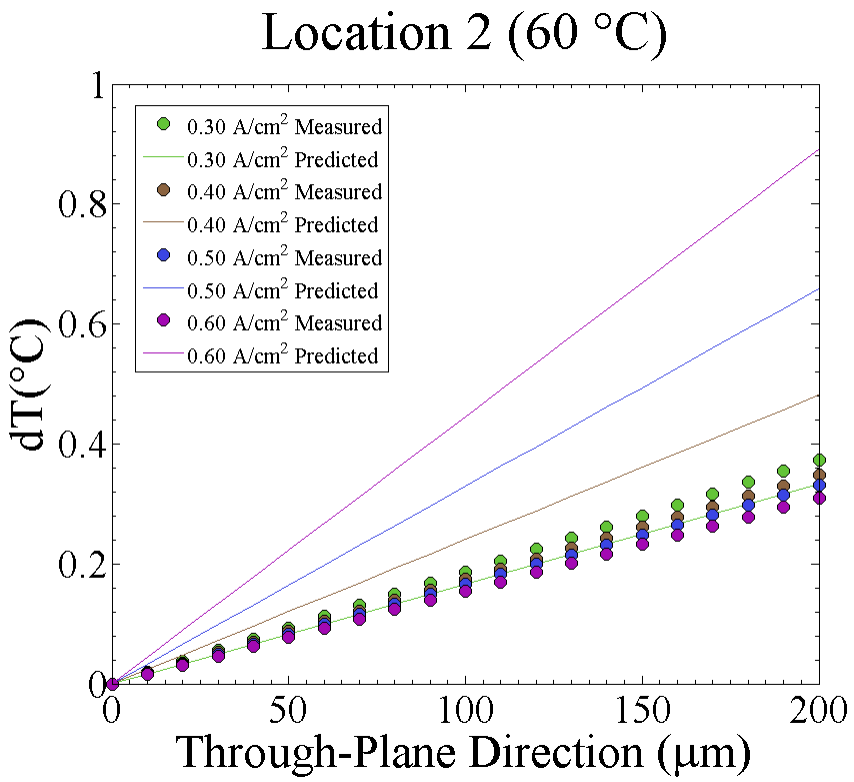

Figure 4.16: Linear regressions of the measured temperature gradients and predicted gradients for the cathode GDL (SGL 10BC) at location 2.

and thus the temperature gradient across the cathode GDL would be less than without the anode land. However, the opposite was observed comparing plots in Fig. 4.15 and 4.16. This discrepancy could be explained by the non-uniformity of the in-plane water saturation in the GDL. Land regions provide a significant transport barrier to water transport into the channels resulting in non-uniformity in water saturation in the in-plane direction. This effect is further compounded by non-uniform water generation as a result of non-uniform current density. Furthermore, non-uniformity in current density results in significant in-plane temperature gradients. Through consideration of these aspects of local temperature distributions in a PEMFC it becomes clear that localized heat transfer throughout an operating PEMFC is very complex. Nonetheless, a reasonable temperature gradient across the cathode CL was measured across the cathode GDL in an operating PEMFC through non-invasive IR imaging and subsequent image processing.

4.5.4.2 Toray TGP-H-120 Results and Discussion

The same approach used on the SGL 10BC data described in section 4.5.3 for evaluating the locations for IR temperature measurements was applied to the data for Toray TGP-H-120 + MPL. In short, the temperature measurements on the GDL cross-section were restricted to regions unaffected by the chips in the windows (result of manufacturing process). Two regions were identified in the collected data as valid for evaluation. The images showing the region bounded by GDL surface in the channels and the location of the chips are shown in Figs. 4.17& 4.18 with the edge of the sapphire chips and GDL surface shown as black and white lines, respectively. These locations will be referred to as locations 1 (L1) and 2 (L2) hereafter but note that location 1 and 2 for the Toray TGP-H-120 + MPL were not the same physical flow channel locations as used in §4.5.4.1 for the SGL 10BC data. However, the physical arrangement (relative to the fuel cell inlets and outlets) of locations 1 and 2 were similar to the SGL 10BC data. Location 1 was near the center of the observable PEMFC cross-section and location 2 was about 14 mm toward the cathode inlet/anode outlet both from location 1.

The IR temperature data were collected at an operating temperature of 60° for current densities of 0.10, 0.20, 0.30, 0.40, 0.50, 0.60, and 0.70 A/cm^2. The polarization curve is shown in Fig. 4.19 and the HFR remained constant throughout testing at 0.08 Ωcm^2. Infrared video was captured for about 3 sec at 30 fps with an integration time of 0.345 ms (factory set) and averaged. To mitigate changes in geometry and emissivity on the GDL cross-section, the measured temperatures were averaged in the in-plane direction across the entire 3.2 mm field of view for each pixel row (5 μm). The initial temperature at the GDL surface was subtracted from each subsequent averaged in-plane temperature to obtain the temperature gradient in the through-plane direction. The results of the through-plane gradient obtained at location 1 is shown in Fig. 4.20 with the expected result of the general trend of linearly increasing toward the cathode CL. This trend was also observed at locations 2 and the results are shown in Fig. 4.21. Note from the images shown in Figs.

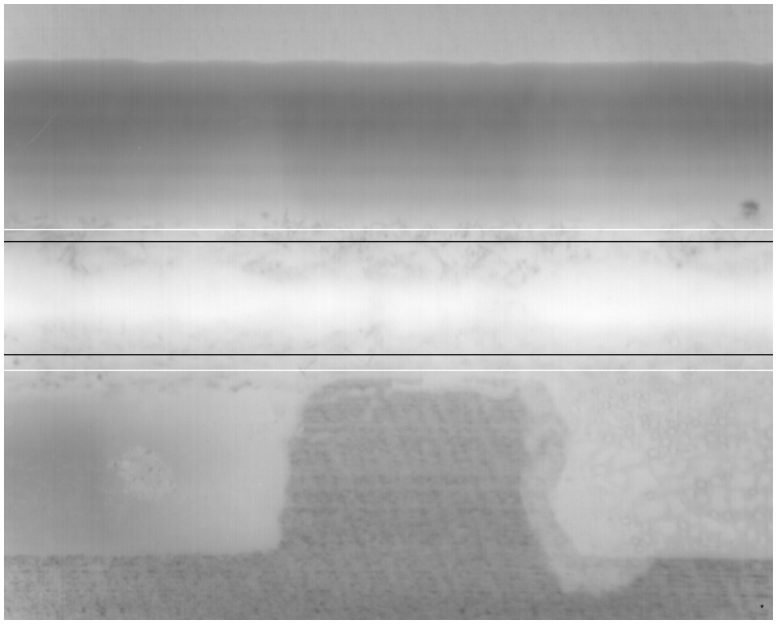

Figure 4.17: Example (j=0.10 A/cm^2) image at location 1 (L1) of the reliable locations revealing significant cathode GDL cross-section between the GDL channel surface (white line) and the influence of the sapphire chips (black line) for Toray TGP-H-120 + MPL.

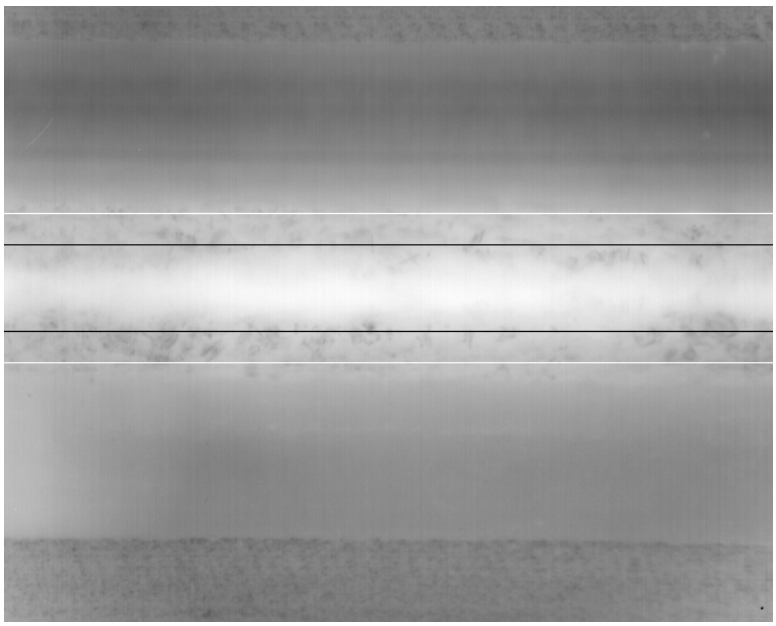

Figure 4.18: Example (j=0.10 A/cm^2) image at location 2 (L2) of the reliable locations revealing significant cathode GDL cross-section between the GDL channel surface (white line) and the influence of the sapphire chips (black line) for Toray TGP-H-120 + MPL.

4.17 & 4.18 that each location has a unique local heat transfer geometry with L1 having 1 anode land and L2 without any lands.

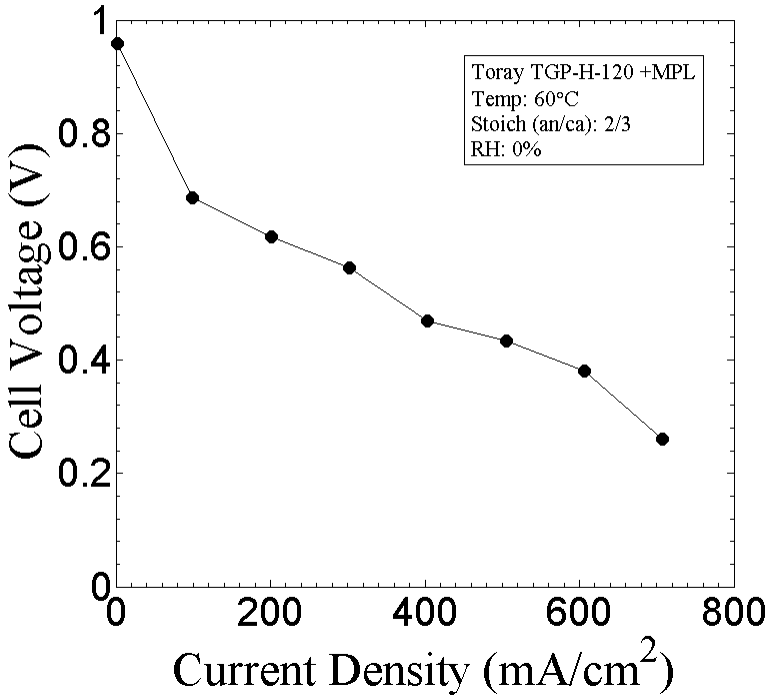

Figure 4.19: Polarization curve of the PEMFC with Toray TGP-H-120 + MPL at 60°. Note throughout testing HFR remained constant at 0.08 Ωcm^2.

Following the analysis used on the SGL 10BC data, the expected temperature gradients across the Toray TGP-H-120 + MPL were compared to linear regressions of the data shown in Figs. 4.20 and 4.21. The estimated expected gradients across the Toray TGP-H-120 + MPL were calculated using Eq. 4.11 with the polarization data given in Fig. 4.19, assumed thermal conductivity of 1.7 W/mK [210], and the assumption that the heat generated is equally divided between the anode and cathode sides. The results for L1 and L2 are shown in Figs. 4.22 and 4.23, respectively. In Figs. 4.20 and 4.21 the expected gradients are shown as solid lines and the linear regression of the measured data shown as data points. These results all show the general trend of under predicting the temperature gradient compared to the linear regression of the measured data.

Figures 4.22 and 4.23 reveal that the estimated expected gradients calculated from the

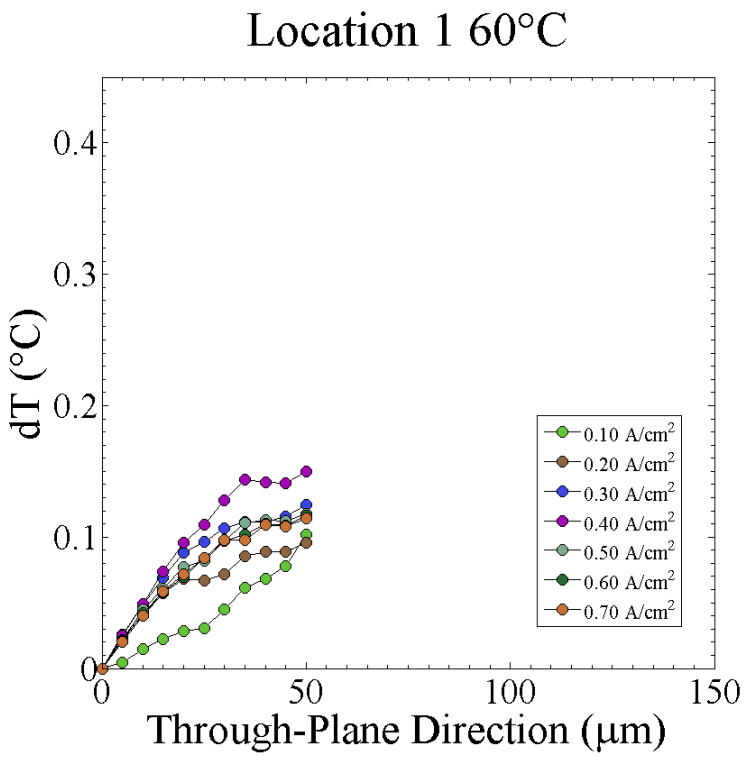

Figure 4.20: Average through-plane temperature gradient across the cathode GDL (Toray TGP-H-120 + MPL) at location 1.

heat generation consistently under predicts the gradients compared to the linear regressions of the measured data. The expected gradient calculation used the manufacturer data of the thermal conductivity which was for untreated Toray TGP-H-120 but the GDLs used where treated with PTFE (5 %) and coated with an in-house MPL by General Motors. The addition of PTFE (k about 0.3 W/mK) should have the effect of lowering the thermal conductivity of the substrate with a much higher initial conductivity of 1.7 W/mK. The lowering of the thermal conductivity would predict higher temperature gradients and thus would help to better predict the data. Additionally, the addition of the MPL coating (generally a mixture of carbon and a high loading of PTFE particles) may also decrease the thermal conductivity but should reduce the contact resistance between the CL and GDL substrate, increasing the effective conductivity. Similar to the SGL data, evaluation of the temperature gradients given in Figs. 4.22 and 4.23 is further compounded by the presence

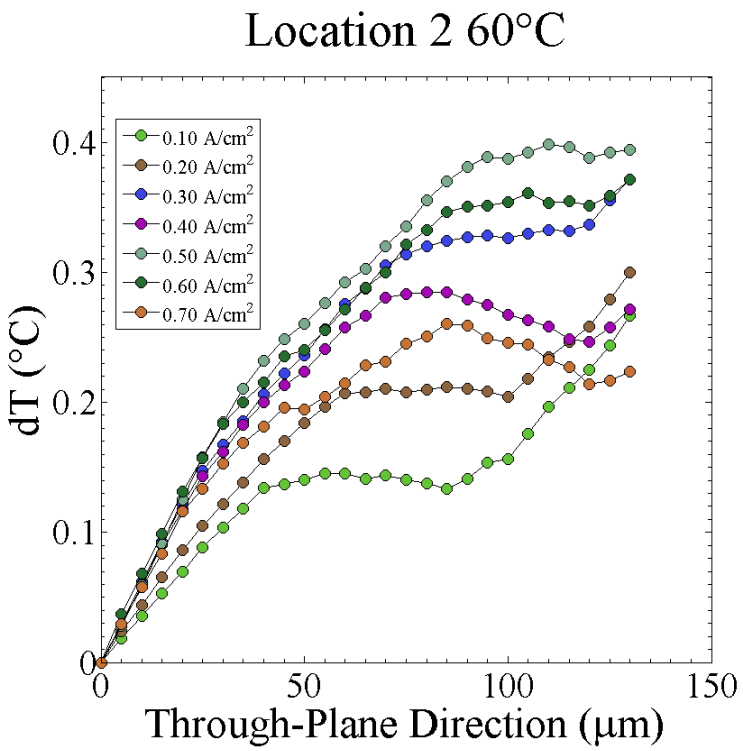

Figure 4.21: Average through-plane temperature gradient across the cathode GDL (Toray TGP-H-120 + MPL) at location 2.

of water within the GDL. Although local heat transfer in the GDL has been shown be very complex with a multitude of factors, the general trend of increasing temperature toward the cathode CL was observed for the Toray TGP-H120 + MPL and SGL 10BC GDLs. Recommendations for future study is given in §6.5.

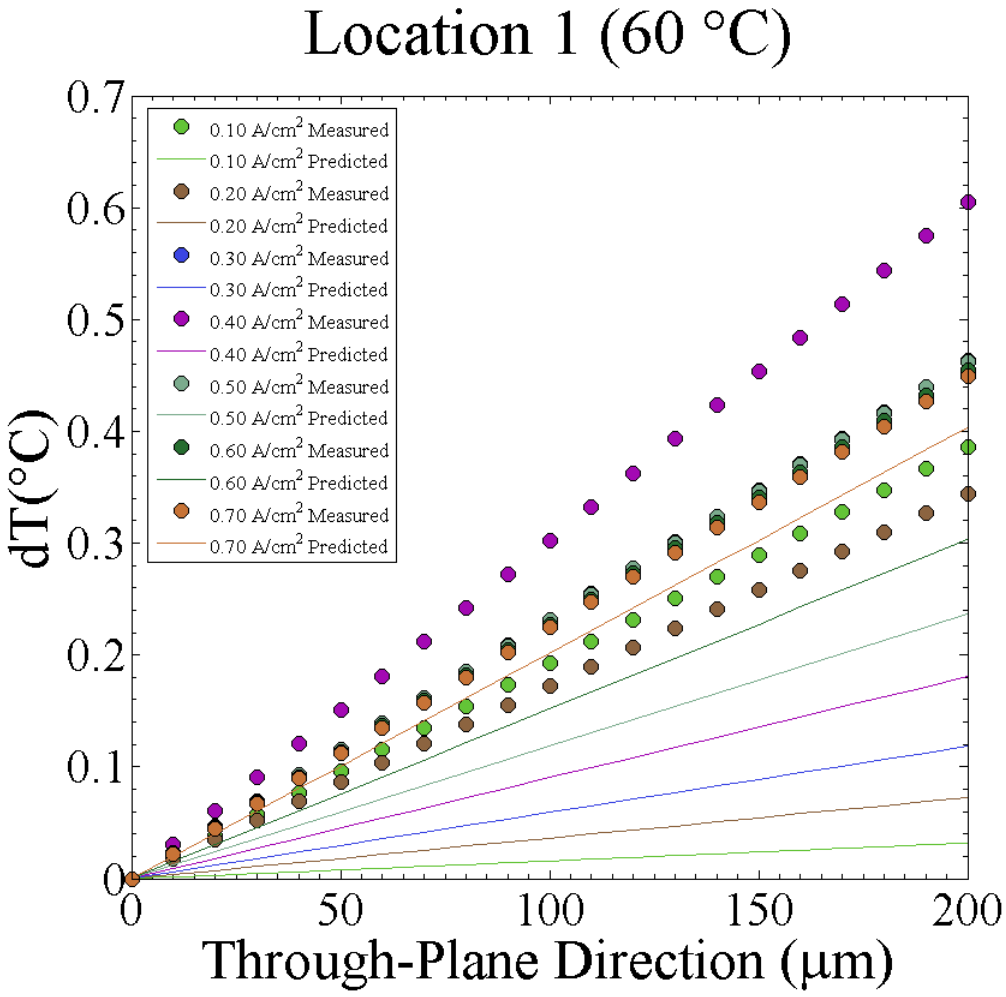

Figure 4.22: Linear regression of the measured and predicted temperature gradients for the cathode GDL (Toray TGP-H-120 + MPL) at location 1.

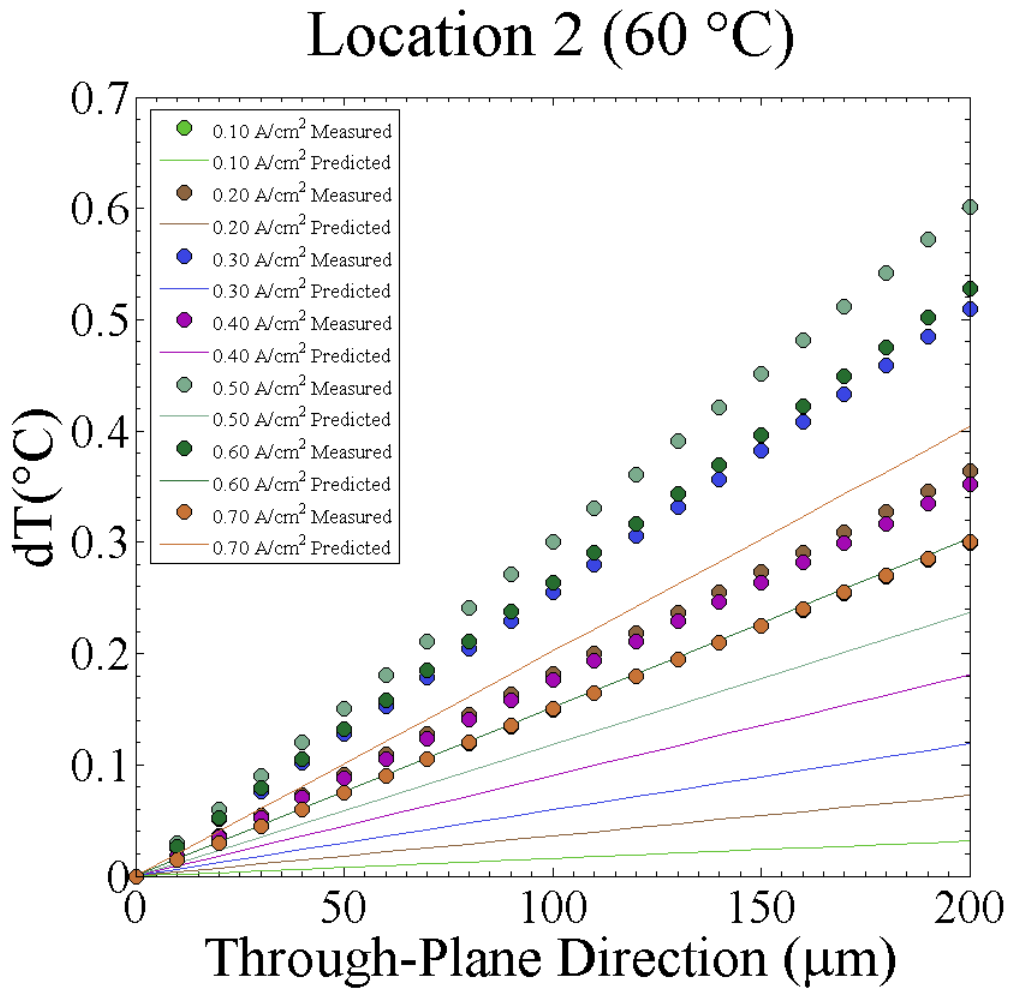

Figure 4.23: Linear regression of the measured and predicted temperature gradients for the cathode GDL (Toray TGP-H-120 + MPL) at location 2.

Chapter 5

Ex Situ GDL Dynamic Liquid Transport

5.1 Experimental

5.1.1 Test section design

An ex situ test section that was originally designed to study water transport dynamics through GDL materials and its effect on two-phase flow in fuel cell gas channels was modified and used in this study to investigate liquid water breakthrough dynamics in GDL materials with and without a MPL. The test section uniformly supplied water to the bottom surface (MPL side when present) through eight water channels 30 mm long, 0.7 mm wide, and 0.4 mm deep with 0.5 mm lands between adjacent channels. As shown in Fig. 5.1, these water channels were supplied with water from three uniformly spaced 0.7 mm water delivery holes connecting the channels to a water manifold which was supplied with water with a syringe pump (Harvard Apparatus 11 Plus). The water channel delivery portion of the test section was fabricated from polycarbonate (Lexan®) and bottom surface of the water manifold was sealed with a rubber gasket. A 50 μm polyurethane film was used to cover the GDL bottom surface at the periphery of the water channels in order to prevent water leakage. In order to visualize the water breakthrough locations, a layer of 0.7 mm thick Porex X-4588 wicking medium (Porex Technologies Corp., Fairburn, GA) was placed on

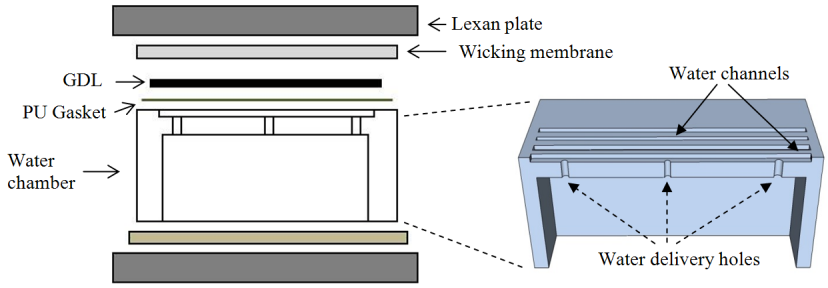

Figure 5.1: Schematic of the breakthrough experimental setup and a 3D view of the water manifold.

top of the GDL. This medium is a hydrophilic high-density polyethylene (HDPE) material manufactured with uniformly distributed pores of size 80-120 mm. The Porex X-4588 material is permeable to water, thus allowing for the uptake of the emerging water and preventing it from expanding along and re-entering into the GDL. This hydrophilic medium has negligible effect on the determination of the GDL breakthrough pressure due to its negative capillary pressure. This test section was compressed between two Lexan plates with bolts. The transparent top Lexan plate and Porex X-4588 material allowed visualization of the breakthrough locations. A Nikon CCD camera (Coolpix P80, Tokyo, Japan) was used to collect the images during the experiments.

5.1.2 Experimental procedure

Deionized water (Millipore Direct-Q®3 (18.2 MΩ)) was supplied to the water manifold at a rate of 10 μL/min, unless otherwise stated. This flow rate was chosen to correspond to the equivalent water production rate of a real fuel cell operating near peak power of a current density of around 1.2 A/cm^2 and a capillary number on the order of 10^{-6}. This equivalent water flow rate does not consider the condensation from the humidified gas streams and the water transport between the anode and cathode in a real operating fuel cell. The water pressure relative to ambient air pressure was measured just prior to entering the test section using a differential pressure transducer (Honeywell FDW2AR) and recorded with a DAQ

system (National Instruments) at 100 Hz. The pressure transducer had an operating range of 0-15 kPa with a precision of 0.2 % over the entire operating range. Assuming that the air in the GDL pore structure is in equilibrium with the surrounding environment, the pressure collected directly measured the capillary pressure across the water-air interface and can be written as:

$$P_c = P_{non-wetting} - P_{wetting} \tag{5.1}$$

where $P_{non-wetting}$ and $P_{wetting}$ are the pressures in the non-wetting and wetting phases across a meniscus, respectively. In GDL materials for PEMFCs water is the non-wetting phase and air is the wetting phase.

Preliminary experiments demonstrated that at a constant water injection rate a large initial breakthrough pressure was always observed. These large pressure spikes were also reported in literature [119, 121]. However, such initial pressure spikes complicate the accurate determination of the breakthrough pressure because it may coincide with the pulses of syringe pump itself (at very low flow rates the syringe pump does not operate in a truly continuous mode). Therefore, a stepwise water injection procedure was employed to avoid such effects. This procedure injected water at a constant flow for a set amount of time and then stopped for a set amount of time to allow for the water pressure to equilibrate. Experimentation revealed the combination of injecting for 2 min and a stop time of 1 min resulting in the best result. The transient response of the capillary pressure and water injection volume of the stepwise procedure is shown in Fig. 5.2. Once the initial breakthrough occurred, the stepwise procedure was unnecessary and water was injected at a constant flow rate. The experiment was run until a sufficient amount of breakthrough events occurred and the Porex X-4588 material was saturated.

Immediately following the breakthrough experiments, the GDL was quickly removed from the test section and the surface water wicked away using a hydrophilic tissue (Kimtech). The mass of the GDL sample was then measured (Ohaus Adventurer) and placed in a room

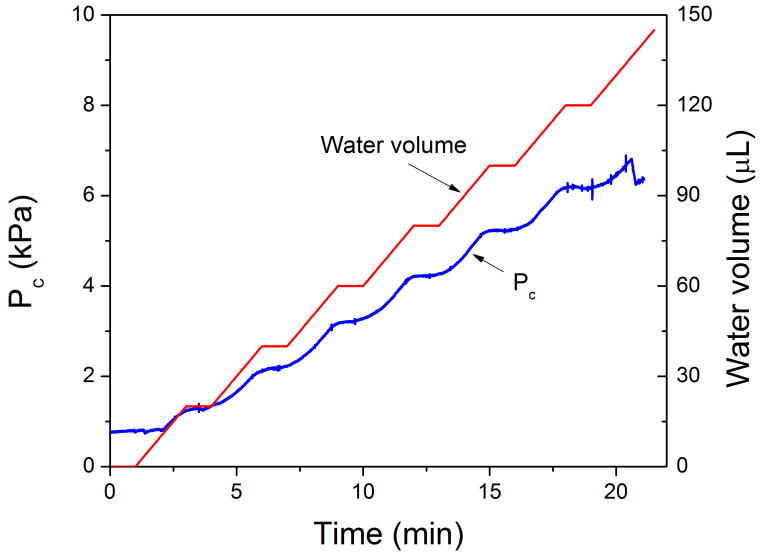

Figure 5.2: Typical transient response of capillary pressure to injected water volume using initial stepwise injection procedure (SGL 25BC).

temperature vacuum chamber to dry for several hours. The mass of the dried GDL sample was measured and the difference from the wet GDL was used to compute the water saturation using the following:

$$S_w = \frac{V_w}{V_p} = \frac{m_w \rho}{A \delta \epsilon} \tag{5.2}$$

where V_w is the volume of water in the sample, V_p is the GDL pore volume, m_w is the mass of the water in the GDL, ρ is the density of water, A is the cross-sectional area , δ is the GDL thickness, and ϵ is the GDL porosity. The thickness of the GDL was measured directly using a micrometer while the porosity was obtained from the manufacturer data. It should be noted that this method may underestimate the water saturation due to the drying procedure. However, the objective was not to precisely measure the water saturation but rather only for comparison between GDL materials tested.

5.1.3 GDL materials

Gas diffusion layer materials from two manufactures with and without MPL coatings were investigated, namely SGL 25 (SGL Carbon Group, Wiesbaden, Germany) and MRC 105 (Mitsubishi Rayon Crop., Otake City, Japan). The SGL samples were purchased from Ion Power (Delaware, USA) and MRC GDLs were provided by General Motors. All GDL samples were carbon fiber paper and treated with PTFE to increase hydrophobicity. SGL 25BC samples had a 30-50 μm thick MPL coating on one side and the MRC 105B had a 10 μm MPL. The fiber sides of these GDLs can be seen in CLSM images shown in Fig. 5.3. These particular GDLs were chosen because of their similar pore structure, thickness, and in situ fuel cell performance [5].

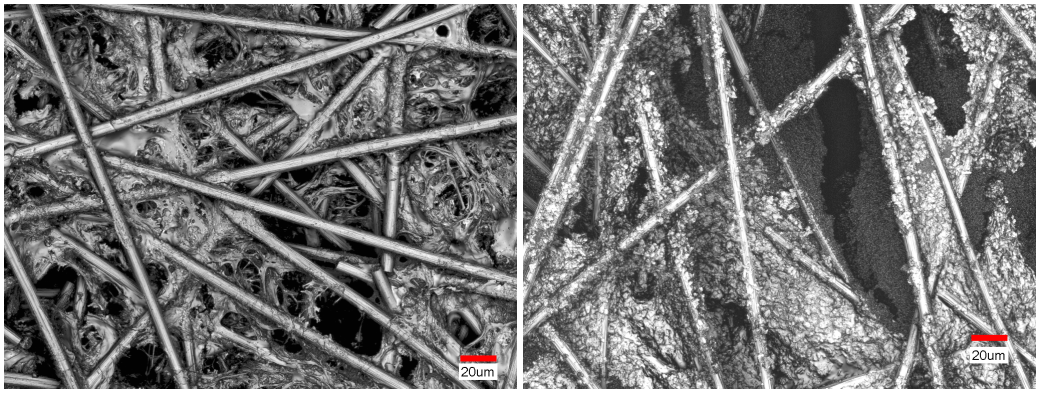

(a) Carbon fiber paper substrate of MRC 105B (b) Carbon fiber paper substrate of SGL 25BC

Figure 5.3: CLSM images of the fiber substrates of GDL materials investigated.

5.2 Results

5.2.1 GDL materials without MPL

Figure 5.4 shows a typical breakthrough behavior through an initially dry SGL 25BA sample. The capillary pressure characteristic of the stepwise injection procedure shown in Fig. 5.2 was omitted from the plot. The breakthrough capillary pressure of this sample was read

Table 5.1: GDL properties, water breakthrough pressures (P_b), water saturation at breakthrough ($S_{w,b}$), equivalent capillary radius corresponding to breakthrough (R_c), and occurrence of dynamic breakthrough locations.

GDL	Structure	Thickness[a] (μm)	PTFE[b] (wt.%)	Porosity (%)	V_{pore} (μL)	P_b (kPa)	$S_{w,b}$ (%)	Dynamic BT locations	R_c (μm)
MRC 105A	No MPL	202 ± 3	7	87	29	7.4 ± 1.1	4.7-12.2	Yes	9.7
MRC 105B	w/MPL	208 ± 3	7	80	28	12.7 ± 1.4	2.4 ± 0.2	No	5.7
SGL 25BA	No MPL	183 ± 3	5	88	27	1.7 ± 0.5	2.6-7.1	Yes	42.4
SGL 25BC	w/MPL	225 ± 3	5	80	30	6.7 ± 1.2	0.8 ± 0.2	No	10.7

[a] Measured with a micrometer.
[b] Manufacturer data.

from the first peak (1.78 kPa).

The most remarkable finding shown in Fig. 5.4 of capillary pressure plot and associated breakthrough images is that it reveals dynamic characteristics of GDL water breakthrough phenomena. The dynamics are exhibited in two aspects: (1) dynamic capillary pressure and (2) dynamic breakthrough locations. As expected, the capillary pressure continued to increase as water was constantly supplied at 10 μm/min (1.2 A/cm^2) until it fully traversed the GDL and emerged and was absorbed into the wicking material. However, instead of drop down to steady-state value, the pressure again built up until a second breakthrough (1.83 kPa) occurred at around 5 min and this fluctuation continued for many breakthrough events. A phenomenon of recurrent breakthroughs was observed for all GDL samples. This was a rather unexpected result as current pore-network models for water transport through GDL materials assume that once a continuous liquid path through the GDL is established (initial breakthrough), water will continuously flow through this continuous path. Contrary to the present findings, a continuous path for water flow would exhibit a constant pressure after the initial breakthrough [23]. The findings of recurrent breakthrough in Fig. 5.4 indicate that the water flow paths through the GDL breakdown due to water drainage on the GDL surface. This phenomenon is further discussed in section 5.3.

The second finding revealed in the testing of SGL 25BA was the dynamics of the water breakthrough locations. The locations on the surface of the GDL where water emerged

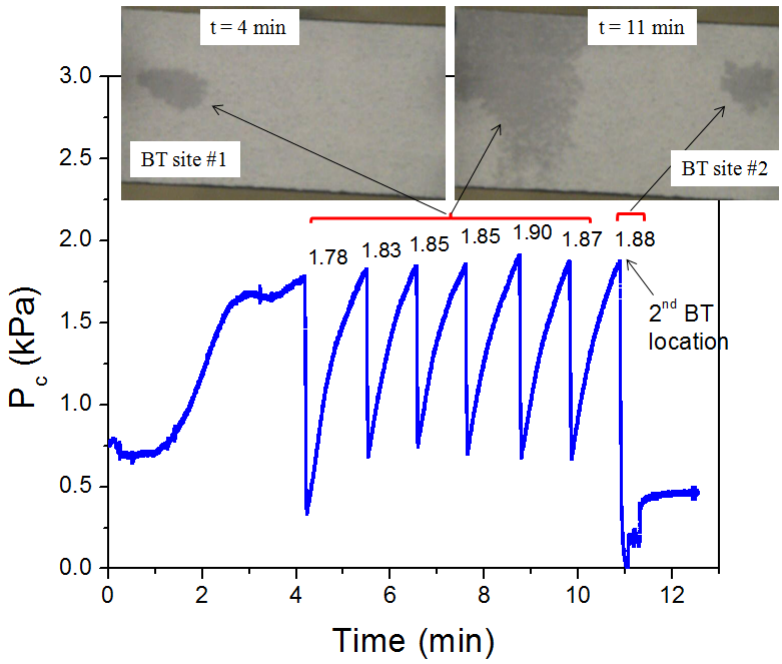

Figure 5.4: Water breakthrough characteristic of SGL 25BA. The inserted images show the wicking material on top of the GDL sample during the breakthrough experiment. The values in the plot indicate the peak breakthrough (BT) pressures.

significantly changed over time as illustrated in the images in Fig. 5.4. The darker regions in the images are locations where water emerged from the GDL surface and absorbed into the wicking material. Notice from the image that the water emerged just from a few preferential locations on the GDL surface. After the initial breakthrough at BT site # 1, five more distinct breakthrough events occurred at that site until a new breakthrough site was established 7 min after the initial breakthrough. This dynamic change in breakthrough location was commonly observed in other SGL 25BA samples as summarized in Table 5.2. A similar phenomenon was observed by Bazylak et al. [119] using fluorescence microscopy and was attributed to branching of the water pathways. However, the dynamic breakthrough locations observed in the present study is strongly related to the dynamic capillary pressure. A detailed analysis on these observations is given in §5.3 and it should be noted that dynamic water breakthrough locations phenomenon is also unaccounted for in current

pore-network models.

Table 5.2: Water breakthrough dynamics in SGL 25BA samples.

Sample No.	Breakthrough characteristics
1	Second breakthrough site after 3 consecutive bursts at the first site
2	Second breakthrough site after 6 consecutive bursts at the first site
3	Two new breakthrough sites after 4 consecutive bursts at the first site
4	Second breakthrough site after 4 consecutive bursts at the first site
5	Only one breakthrough site observed near the edge of water channels
6	Second breakthrough site after 5 consecutive bursts at the first site

The GDL water saturation was measured and the results are given in Table 5.1. Due to the dynamic water breakthrough behavior, a wide range, from 2.6 % to 7.1 %, was measured from sample to sample.

The water breakthrough behavior of MRC 105A samples (without MPL) was fairly similar to that of SGL 25BA. A typical capillary pressure characteristic with a breakthrough image is shown in Fig. 5.5. Recurrent breakthrough events are clearly present in the plot and dynamic breakthrough location was also observed. Although MRC 105A exhibited a similar dynamic behavior, significant differences were observed. The MRC 105A GDL displayed a significantly greater breakthrough pressure as well as greater water saturation at breakthrough than SGL 25 BA (Table 5.1).

It is generally accepted that the capillary pressure in porous media describes the throat diameters in the pore-network. The critical throat size is defined as the radius of an equivalent capillary exhibiting the same capillary pressure as the breakthrough pressure and can be calculated from the Young-Laplace equation:

$$P_c = \frac{2\sigma cos\theta}{R_c} \tag{5.3}$$

where σ (0.0072 N/m) is the surface tension of water, θ is the contact angle of water inside the GDL, taken as approximately the contact angle of water on PTFE (120°), and R_c is the equivalent capillary radius. Utilizing Eq. 5.3 the critical throat size of the GDL materials

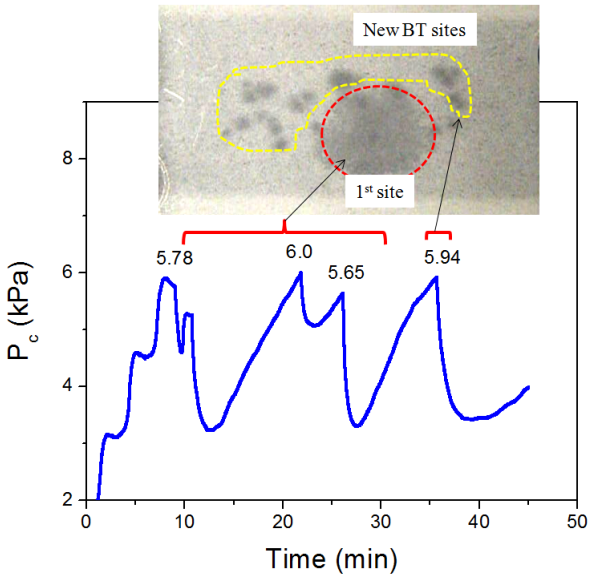

Figure 5.5: Water breakthrough characteristics of MRC 105A. The inserted image shows the wicking material during the experiment revealing multiple breakthrough locations. Note the contrast in the image was increased to highlight the wetted regions. The values in the plot indicate the peak breakthrough (BT) pressures.

were calculated and are shown in Table 5.1. The critical throat diameter for MRC 105A materials was found to be 19.5 μm which is close to the mean pore size of the GDL, but the critical throat diameter for SGL 25BA was found to be about 85 μm. This difference in critical throat size is related to both the GDL microstructure and the internal wettability. As shown in Fig. 5.3, MRC 105A has somewhat smaller surface pores than SGL 25BA. Furthermore, MRC 105A carbon binding material has a fine web structure that may further restrict water from emerging where the carbon binding material for SGL 25BA has a particle agglomerate structure concentrated on the fibers. The higher PTFE content of 7 wt.% in MRC 105A will also increase the breakthrough pressure and thus decrease the critical throat size compared to the 5 wt.% PTFE in GDL 25BA. Nonetheless, the critical throat size of 85 μm in SGL 25 BA is significantly larger than its mean pore size which may indicate the internal contact angle is much smaller than 120°.

5.2.2 GDL materials with MPL

GDLs used in fuel cell applications are normally coated with a MPL to improve performance at high current densities. The MPL helps to mitigate water flooding and severe mass transport losses that usually occur in the regime and is sometime referred to as the water management layer. The effects of the MPL on the breakthrough pressure characteristics and water saturation was investigated with the MPL facing the water distribution channels to mimic the configuration used in actual fuel cell (in contact with the catalyst layer). The case for which the MPL was on the opposite side of the water channels was not tested due to the fact that this configuration is rarely used in fuel cell applications.

Although MPL thicknesses were significantly different, both the MRC 105B (MPL 8 μm) and SGL 25BC (40 μm) materials had similar breakthrough characteristics. Figure 5.6 shows the typical capillary pressure characteristics of SGL 25BC exhibiting recurrent breakthrough events similarly to what observed for the case without a MPL (see Fig. 5.4) indicating the breakthrough phenomenon was dynamic. Similar recurrent breakthrough events were also observed for MRC 105B samples. However, the breakthrough location was not observed to shift for either SGL 25BC or MRC 105B suggesting that water flows in the same preferential paths inside the GDL and emerges at the same location on the GDL surface formed during the initial breakthrough. An example image of the single breakthrough location for SGL 25BC is shown in the inset image in Fig. 5.6. This finding of a stationary breakthrough location for GDLs with MPLs is in sharp contrast to the GDLs without a MPL (see Figs 5.4 & 5.5) for which dynamic breakthrough locations was commonly observed. This result indicates that the MPL plays a pivotal role in stabilizing the preferential water pathways.

The breakthrough pressures and water saturations for MRC 105B and SGL 25BC were measured and are shown in Table 5.1. In general, the GDL samples with a MPL had a higher breakthrough pressure than the corresponding GDL substrate without a MPL. This was an expected result of the much smaller pore size and PTFE loading of the MPL. Con-

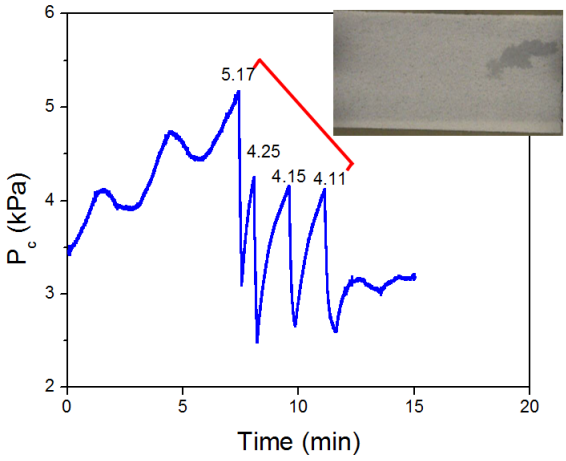

Figure 5.6: Water breakthrough characteristics of SGL 25BC. The inserted image shows the wicking material during the experiment revealing one a single breakthrough location. The values in the plot indicate the peak breakthrough (BT) pressures.

sidering a mean pore size of 0.5 μm for a typical MPL, the MPL could have breakthrough pressure of about 300 kPa from Eq. 5.3. However, the breakthrough pressure for both MRC 105B and SGL 25BC of nearly of the same order of magnitude as the fiber substrates without MPL, e.g. 12.7 kPa vs. 7.4 kPa for MRC samples and 6.7 kPa vs. 1.7 kPa for SGL samples. This indicates the MPL does not function as a uniform barrier because if it did much greater breakthrough pressures would have been measured given the sub-micrometer pore size hydrophobicity. Instead, water flows through defects in the MPLs as shown for both MRC and SGL GDLs in Fig. 5.7. The CLSM image of the MRC 105B MPL shown in Fig. 5.7(a) reveals its uniformity but is relatively thin (about 8 μm) and barely covers the fiber substrate. Locations where the fibers are not completely covered provide preferential pathways for water to penetrate into the substrate with a much smaller breakthrough pressure, e.g. 12.7 kPa compared to 300 kPa. Likewise, despite the greater thickness (about 40 μm) of the MPL of SGL 25BC it still provides many preferential pathways for water penetration through relatively large cracks on the order of tens of micrometers. These cracks would reduce the breakthrough through pressure drastically compared to a crack-free MPL

with pores two orders of magnitude smaller. These finds on the MPL may be specific to the GDL materials studied here but it is interesting to note that the 'defects' in the MPL may be beneficial to fuel cell water management. Furthermore, additional gains in water management could be made if the defects were precisely controlled.

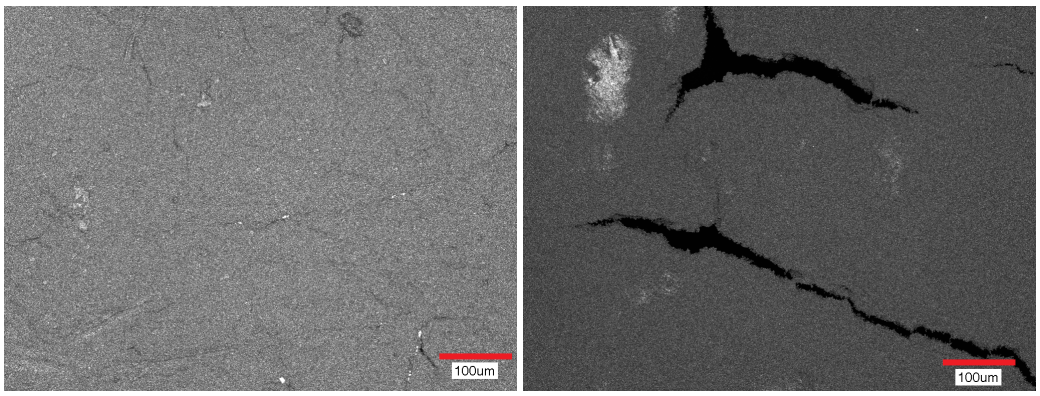

(a) MRC 105B MPL (8 μm). (b) SGL 25BC MPL (40 μm).

Figure 5.7: CLSM images of the MPL of GDL materials investigated. Note the preferential water pathways provided by a thin (8 μm) MPL coating for MRC and the relatively large cracks in SGL 25BC.

The water saturation at breakthrough for the GDL samples with a MPL was lower than the GDL samples without the MPL. The saturation of MRC 105B and SGL 25BC were measured to be 2.4 % and 0.8 %, respectively. The measured saturation for SGL 25BC was close to the reported value of 3 % for SGL 10BB obtained by Gostick et al. [208]. These saturation values were three to eight times lower than those of the corresponding sample without a MPL. This result implies that a MPL can greatly reduce water saturation in GDL. A similar result has been reported in literature and was explained by the limitation of water access to the GDL substrate by the MPL [191, 208].

5.3 Discussion

Water breakthrough in both MRC and SGL type GDLs was observed to occur at a few preferential locations while exhibiting a dynamic characteristic. The dynamic characteris-

tic was reflected in two aspects: (1) dynamic capillary pressure (or recurrent breakthroughs) and (2) dynamic breakthrough locations (or changing of breakthrough locations with time). The former was commonly observed in all GDLs tested while the latter was observed only in GDLs without a MPL. Generally, very small water saturations ($<$10 %) were observed at breakthrough for all GDLs tested. These low water saturations combined with the observations of preferential breakthrough locations implies an anisotropic heterogeneous flow process in GDL. Furthermore, if water did flow in an isotropic, homogeneous pattern, a much greater water saturation and significantly larger number of breakthrough locations would result. An anisotropic, heterogeneous water flow inside a GDL can form fast "water transport channels" which are more or less straight or column-like. These channels are essentially the "fingering and channeling" observed by Litster et al. [122], the "column flow" observed by Gao et al. [121], and the "eruptive mechanism" observed by Manke et al. [134, 167].

A possible interpretation of the observed phenomena can be explained in terms of Haines jumps, a description of discontinuous drainage displacement employed in geological disciplines [62, 196]. In slow drainage, when a non-wetting fluid (water in GDL) slowly displaces a wetting fluid (Air in GDL) in porous media, the displacement is controlled solely by the pressure difference between the two fluids. Restrictions in the pore-throat network of the porous medium hinder the flow from advancing linearly. The interfaces between the fluids may remain stationary even when the pressure in the displacing fluid is increased. Once the invading fluid pressure exceeds the capillary pressure at the largest restriction, the invading fluid will suddenly move into the adjacent pores and quite often through one or more of these restrictions simultaneously. This process is usually accompanied by a negative capillary pressure drop as a result of the readjustment of the interfaces between the fluids in the porous medium. This localized bursting of the advancing non-wetting fluid into the initially saturation porous medium is a stepwise process of drainage and has been called avalanches, Haines jumps, or bursts in literature [62, 196].

The transition (bursting) of water from the GDL substrate into the wicking material (or gas channels in an actual fuel cell) is triggered by the mechanism as within the GDL by considering the wicking material (gas channels) as a new porous medium with much larger pore size than the GDL. The droplet emerging from the GDL surface grows spontaneously and carries away water from the adjacent GDL pores. However, the supply of water to these adjacent pores is often not sufficient for the droplet to fill the larger pore (i.e. gas channel or to saturate the wicking material) and is "choked-off." This "choke-off" leads the pores adjacent to the GDL surface emptied by the departing droplet and results in the breakdown of the continuous water paths. These emptied pores can then be refilled if a constant supply of water is injected and the bursting process will occur again resulting in recurrent breakthrough events. After a breakdown of a continuous water path, the water within the GDL spontaneously readjusts its interfaces in a relaxation process and may result in a new breakthrough location. Figure 5.8 is a schematic of such a process. Thus, the proposed mechanism can explain both the dynamic capillary pressure behavior and the dynamic breakthrough location phenomena.

The MPL was observed to have two effects on the water breakthrough behavior in both GDLs studied. The first effect was the limiting of access to the GDL substrate limiting the number breakthrough locations. This function of the MPL to control breakthrough locations has also been observed in previous studies [191, 208]. The present measurements further indicate that the MPL reduces the water entries to the GDL mainly via defects, such as cracks and breakdowns of the MPL by GDL fibers. The second role of the MPL in water breakthrough observed was the stabilization of water paths/morphology through the GDL. These effects can also be accounted for by the transport mechanism previously proposed. Figure 5.9(a) shows how the water flow paths in a GDL without a MPL are interconnected and thus the changing of breakthrough location by the spontaneous redistribution of water configuration after a breakthrough event is probable. However, in the case of a GDL with a MPL, the water flow paths are not interconnected due to the limiting of access effect of the

MPL (see Fig. 5.9(b)). Therefore, it is much less likely that the localized bursting occurring at the end of one water flow path would affect the configuration of the other water flow paths, thus increasing the stability of the flow paths. This effect together with the limited number of water access to the GDL results in greatly reduced number of breakthrough locations compared to GDL without a MPL. As a natural consequence, MPLs greatly lower the water saturation because the saturation is proportional to the total number of water paths in a GDL.

In general, only a few breakthrough locations were observed in the ex situ experiments and the MPL further reduced this number. However, in situ observations in an operating PEMFC reveal a greater number of droplets (or breakthrough locations) on the GDL surface [82, 216]. This discrepancy may indicate the contribution of other water transport mechanisms. The transport of water vapor through the MPL and GDL is one such mechanism, especially for fuel cells operating at higher temperatures. Due to the temperature gradient across the GDL, water vapor transported from catalyst layers and MPL condenses and forms micro-droplets inside the GDL. These micro-droplets then agglomerate to form macro-droplets that eventually flow preferentially toward larger pores and finally breakthrough in the gas channels. This water transport mechanism was first proposed by Nam and Kaviney [192] in terms of an "inverted tree-like water transport". A feature of this transport mechanism is a large number of breakthrough locations from the large number of condensation sites in the GDL. At high fuel cell operating temperatures or a high temperature gradient across the GDL, the vapor condensation in the GDL is greatly increased and the contribution of the tree-like transport may eventually become dominate, producing many more breakthrough locations. This indicates that the liquid water transport through a GDL is very complicated and no single mechanism can fully describe it.

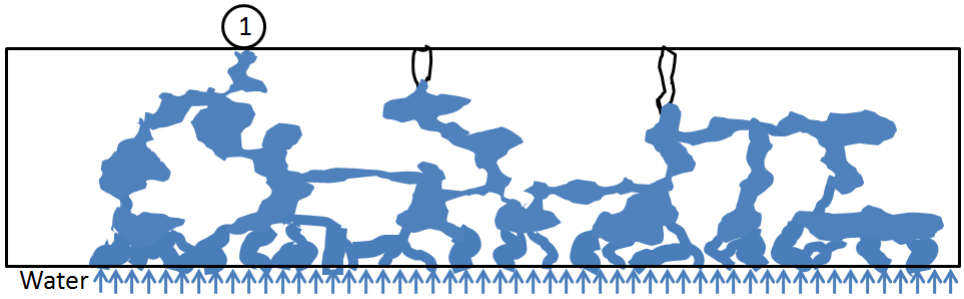

(a) Initial water breakthrough location

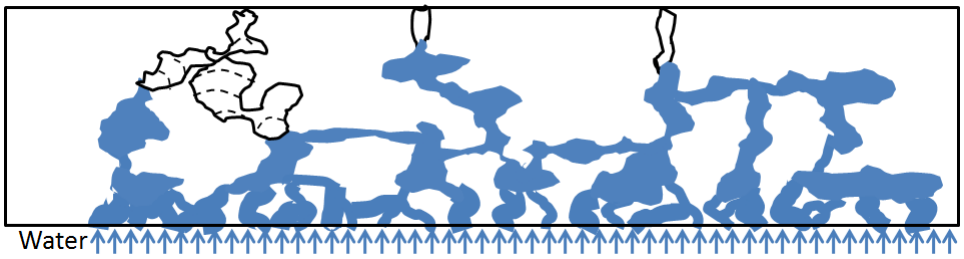

(b) The "choke-off" empties adjacent pores and breaks down the continuous water path

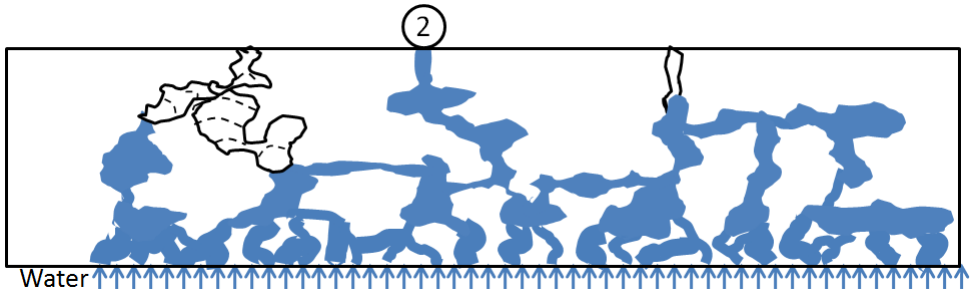

(c) Spontaneous redistribution of water within the GDL allowing for a possible second breakthrough location

Figure 5.8: Schematic depicting the dynamic breakthrough phenomena through GDL materials.

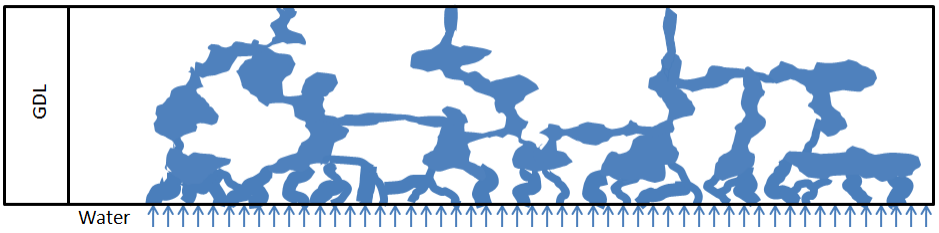

(a) Water drainage without a MPL showing many water entry points

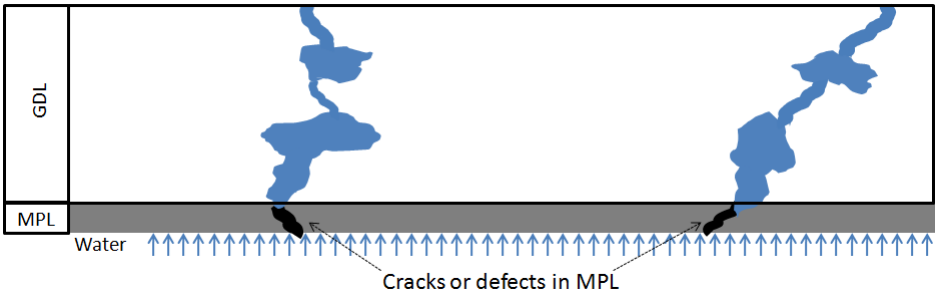

(b) Water drainage with a MPL restricting water entry into the GDL substrate to only crack/defect locations of the MPL

Figure 5.9: Schematic depicting the effect of the MPL on dynamic breakthrough phenomena through GDL materials.

Chapter 6

Conclusions

6.1 Summary

In this work, three interrelated studies were undertaken to improve understanding of water transport in PEMFC gas diffusion layers. The first objective focused on a new numerical simulation tool to digitally generate realistic 3D geometries of GDL microstructures including localized binder and PTFE distributions in a cost- and time-effective manner. The focus of the second objective was to investigate the through-plane transport processes in a PEMFC using visible and infrared imaging and subsequent image analysis. The last objective revealed fundamental liquid transport mechanism through GDL materials with and without MPLs. Specific conclusions resulting from this work and proposed future work are discussed in the following sections.

6.2 Digital GDL Microstructure Generation

A numerical simulation tool was developed to provide realistic 3D phase-differentiated geometries of GDL materials for modeling efforts. For the first time, localized binder and PTFE distributions were generated throughout the 3D structure which allows for mapping of hydrophobic and hydrophilic pathways in GDL materials. The generation algorithm was

implemented using a new framework and mimicked manufacturing processes by using 3D morphological image processing to incorporate both carbonaceous binder and PTFE. The fibrous skeleton was generated using a stochastic technique and subsequently processed to add carbonaceous binder in a manner that mimics the manufacturing processes. PTFE treatment of the digital GDL was accomplished through an additional morphological image processing step and was compared to confocal laser scanning microscope images of Toray TGP-H-060 with PTFE treatments. The digital GDL algorithm was implemented through a graphical user interface with intuitive input parameters of porosity, fiber radius, thickness, percent binder, percent PTFE, voxel size, and domain size. The results for the digital generation of Toray TGP-H-060 with 0 wt.% PTFE were in good agreement with CLSM images as well as 3D X-ray tomography studies. The resulting structure can be readily used for analyzing transport processes by using commercial CFD software packages. The proposed framework and algorithm provide for the first time a complete phase differentiated (fiber, binder, and PTFE) digital 3D microstructures in a cost- and time-effective manner.

6.3 Through-plane Visible and IR Imaging of a PEMFC

Through-plane transport in an operating PEMFC was investigated by developing and testing a transparent (visible and infrared) PEMFC. The new cell design allowed for simultaneous visualization of both the anode and cathode (including GDLs) in visible and mid-wave infrared wavelengths. Visible observations with a digital microscope revealed anode GDL water transport was dominantly in the vapor phase as opposed to the cathode GDL where liquid water was routinely observed. This result indicates that water flooding and the consequent mass transport resistance in the anode GDL may not be as serious as in the cathode because liquid water did not accumulate inside the porous GDL and block hydrogen pathways. High magnification observations of the cathode GDL and subsequent video processing revealed the condensation of microdroplets and implied the existence of condensation

within the GDL but confirmation could not be made due to current limits on test section design. Noninvasive temperature gradients across the cathode GDL with 5 μm pixel resolution were obtained using infrared imaging and subsequent image analysis. An averaging technique was implemented to determine an effective emissivity to account for the heterogeneous GDL cross-section. Temperature measurements on the cathode GDL exhibited the general trend of increasing temperature toward the cathode CL. Recommendations for further improvement of the noninvasive IR temperature measurements were made.

6.4 Ex Situ GDL Dynamic Liquid Transport

The liquid water breakthrough dynamics across GDLs with and without MPL were studied in an ex situ setup which closely simulates a real fuel cell configuration and operating conditions. The following conclusions were made from the results:

- The capillary pressure inside GDL materials was dynamic even after the initial breakthrough event. Recurrent water breakthroughs were always observed indicating the breakdown and re-build of water paths. Recurrent breakthrough events were caused by an intermittent water drainage process from the GDL surface.

- For GDL samples without a MPL, the location of breakthrough events was observed to be dynamic. However, for GDL samples with a MPL no such phenomenon was found. The water saturation for GDLs with MPL was significantly lower than the samples without MPL. These results suggest that the MPL not only limits the number of the water entries into the GDL (so that the water saturation is drastically reduced), but also stabilizes the water paths (morphology).

- A water transport mechanism, explained in terms of a Haines jump mechanism, was

proposed to account for the dynamic breakthrough behaviors through GDL materials.

6.5 Future Work

The work presented here forms the foundation for developing new models related to liquid water transport in a PEMFC GDL. Specific suggestions in the three areas are discussed in the following sections.

6.5.1 Digital GDL Microstructure Generation

The newly developed method of generating digital GDL microstructures represents the initial framework for an entire body of work that could be extended in many directions. The microstructure generation algorithm could be extended to include less anisotropic GDL materials such as those manufactured by SGL or MRC. This could be incorporated in the current model by removing the constraint on the fibers containing them within a plane and applying a through-plane distribution for associated component of the fibers' vectors. However, this approach would still not account for the curvature (or crimp) of the fibers but may provide a reasonable approximation to these actual hydroentangled GDLs materials. The curvature of the fibers could be incorporated into the current framework by simply replacing the definition of the fiber (unit vector, $\hat{C}$ and a point (x_o, y_o, z_o) with an expression for the desired curvature over the domain. The expressions could be as simple as a single sinusoid or for complete control over the shape throughout the domain, a spline could be implemented. A spline fitted to a distribution of points representative of the degree of entanglement of actual GDL materials may result in geometries very close to that of actual hydroentangled GDLs. Complete control over in-plane and through-plane components of the fibers would allow for a systematic study of fiber directional distribution on transport resistance and other transport properties. The directional distribution of the fibers may

also have an effect on GDL intrusion into the channels and should also be considered with transport properties for GDL optimization.

The generation algorithm could as be extended to incorporate more varieties of binder material such as those exhibited in SGL or MRC materials. The binder morphology of GDL materials significantly varies as shown in section 1.3. The morphology of SGL binder material appears to be comprised of small particles that accumulate on and around fiber intersections and not as thin films observed for Toray GDLs. These small binder particles could be incorporated into the generation algorithm by replacing the binder addition function in the MATLAB Toolbox with one that mimics this morphology. This could be accomplished through a variety of methods. One such method would be to randomly select void voxels to be potentially filled with binder. If the voxel selected is a neighbor of a fiber or previously assigned binder, then that voxel would be assigned as binder. Otherwise, the voxel would remain void. This caveat would eliminate "floating" binder voxels that would be physically unrealistic. However, this method may result in porous binder if additional considerations are not made and may generate unrealistic binder material. The binder morphology of MRC GDL materials would also be challenging to implement digitally but could be approached with a variety of methods. MRC binder material could be approached with a similar method to that used for Toray in this study (3D morphological closing with spherical SE) with an additional processing step. After the binder was added to the fiber skeleton using 3D morphological closing, an additional step of randomly removing binder in the shape of holes could be conducted. This could be implemented by first isolating the binder phase and placing it in an independent array. Then, binder material could be removed randomly in the shape of disks throughout the binder solid until the desired binder volume was achieved. The resulting binder array would then be re-combined with the GDL skeleton to produce the complete GDL structure. Equipped with multiple functions for the binder addition, the effect of the binder morphology on transport properties could also be studied with subsequent simulations.

The proposed method for simulating PTFE treatment results in a relatively uniform distribution with cyclic maximums located at layer intersections. Incorporation of a through-plane component of the fibers using the current method for PTFE addition would result in a more uniform PTFE distribution. The most common method of PTFE treatment for GDL materials results in varying degrees of nonuniformity in PTFE content and strongly depends on the drying process [9]. A fast drying method results in high concentrations of PTFE near the surfaces and a slow drying method results in more uniform coating. These different drying methods could be mimicked in the PTFE addition step by independently considering sections of the digital GDL. The first few layers towards the GDL outer surfaces could be isolated into their own independent arrays and subsequently treated with a higher loading than the bulk. The 3D structure can then be re-assembled into the final GDL material. Similarly, an arbitrary PTFE distribution could be digitally implemented to investigate the optimal PTFE distribution using in modeling efforts.

Characterization methods of the generated GDL structures could also be extended for further analysis. Material properties such as tortuosity, surface roughness, and pore size distribution could improve GDL evaluation. The tortuosity of the generated microstructures could be estimated through a variety of methods. Initially, the 3D phase-differentiated geometry would be reduced to a binary 3D structure containing only solid and void voxels. Then, a random walk method could be applied to one side of the GDL structure and the path of a virtual particle could be tracked until it reaches the other side. This process would need to be repeated for many iterations and starting points to obtain an average tortuosity. This method would allow for the tortuosity to be estimated for both the in-plane and through-plane directions. The surface roughness in terms of R_a could be implemented by using the relative dimensions of the voxels. The top most section of the digital GDL would be a reference height and at each row, the relative depth to the next solid voxel could be computed. This would be repeated across the domain for a particular row. This would provide the line roughness at that location and could be implemented for any row

(or column) of the digital model. Surface roughness would be a straightforward extension to the line roughness where each row and column would be considered in the computation. The pore size distribution of the fibers would also provide valuable information on the generated GDL samples. One method that could be used was implemented by Schulz et al. 2007 who used morphological opening with spherical structuring elements of increasing radius to determine the pore size distribution in their generated GDL samples [28].

The main objective of developing the proposed generation model was to provide realistic 3D geometries of GDL materials for future modeling efforts of transport processes. The transport modeling could be implemented in variety of methods including standard CFD methods, lattice Boltzmann, pore network modeling, or full morphology. A review of lattice Boltzmann, pore network, and full morphology methods are given and compared for liquid water transport through GDL materials by Sinha et al. [13]. The initial step in using commercial CFD software packages would be to successful mesh the generated geometry. Depending on the software used to generate the mesh, modification of the output 3D image might be necessary for the mesh to be properly applied. Pore network modeling using the generated GDLs would be require a methodology to reduce the complicated pore structure to a representative idealized pore network. One advantage of using the phase-differentiated digital GDLs would be the additional parameter of the hydrophobicity of the pores that could have a strong impact on the transport properties. These simulations could be conducted on the generation GDLs to provide insight on liquid water transport including Haines jump dynamics that are not accounted for in current pore network models. Utilizing the realistic complete phase differentiated 3D geometries, more accurate predictions of the liquid and heat transport could be made. These predictions coupled with the material properties from the characterization methods will allow for digital GDL optimization in a time- and cost-effective manner.

6.5.2 Through-plane Visible and IR Imaging of a PEMFC

The investigation of through-plane transport in an operating PEMFC using visible and infrared imaging can be extended through a variety of approaches. A new design of the transparent flow fields which allowed for direct observation of the MPL and CL would be a great improvement on the current design. A new design with the potential direct observation of the flow paths from water generation in the CL to removal in the channel will enable the study of transport within these layers as well as across the associated interfaces. Water hold-up due to interfacial transport resistance across these layers could also be studied. With each individual layer exposed for both visible and infrared imaging, confirmation of a condensation front within the GDL, MPL, and/or the CL could potentially be made. Infrared observations may allow for the measurement of the effect of condensation on the heat transfer across the GDL materials. The limiting factor in the current test section design that occluded the MPL and CL was mainly due to the fabrication of the sapphire windows. A new design should carefully consider the manufacturing process to mitigate chipping of the sapphire. The current work used a grinding process (with a diamond wheel) and resulted in chips on the order of 50 μm thick, occluding most of the MPL and the entire CL. A different manufacturing process for the windows is recommended for future work or a new window design that would eliminate this issue.

The test setup could also be improved with simultaneous visible and infrared observations. Equipped with both visible and infrared data from the through-plane direction, the effect of the presence of water saturation on the GDL could be studied. The presence of water on the cross-section of the GDL would affect the IR temperature measurements but could be accounted for using simultaneous visible observations. Additionally, image fusion techniques could be applied to the multi-spectral data. The high spatial resolution visible data could be fused with the lower spatial resolution IR data to produce higher spatial resolution temperature image than the IR camera could produce independently. An additional complication of this experimental setup would be the additional image processing required

for geometric mapping or registration of the images from two cameras. Simultaneous visible and infrared captures could be accomplished using a cold mirror such as silicon that reflects visible light but has a high transparency in infrared. A test fixture would have to be developed such that the visible lens would be positioned at 90° relative to the IR lens and the mirror positioned at 45° relative to both. A similar testing configuration was successfully used by Ishikawa et al. 2007 for investigation of freezing phenomena [110].

This work could be further explored by extending the number of GDL materials tested. Including testing of a wider range of GDL materials will allow for parametric studies on the effect of material properties such as thermal conductivity, manufacturing techniques, pore structure, etc.. Specifically, the thermal conductivity of the GDL will affect the temperature gradient but more interesting is its effect on the location of condensation within the GDL. The location of condensation within the GDL will have a strong impact on water saturation and transport resistance within the GDL. Thus, water saturation should be well characterized for accurate modeling.

Incorporation of the previously discussed digital generation of GDL materials would be a very interesting extension of this in situ work. Using the generation algorithm with improved characterization techniques, the thermal conductivity of the GDL materials could be predicted. These predicted values could then be compared to the thermal gradients obtained from IR imaging. Modeling efforts using the generated GDLs could be validated using this or an improved test section for the location of a condensation front as well as interfacial transport resistances.

6.5.3 Ex Situ GDL Dynamic Liquid Transport

The extension of the work on dynamic liquid transport through GDL materials could be extended by expanding the GDL materials tested. Additional investigation of more GDL materials would allow for a detailed parametric study of the effects of GDL thickness, manufacturing technique, PTFE loading, and MPL coating on breakthrough pressure and

water saturation. Insight into the effect of these material properties will add to the current understanding of liquid transport through GDL materials and help provide a direction for future designs of improved GDL materials.

Future work on water breakthrough dynamics could be extended by further characterization of the observed recurrent breakthroughs. The frequency of the recurrent breakthrough events may be a function of the volume of the pores near the surface of the GDL. The draining of a large volume of interconnected pores near the GDL surface would require more time than a smaller volume to refill before the next breakthrough event could occur. This could be further investigated with more BT data from a variety of GDL materials and further characterization of the GDL surface. This further characterization of breakthrough phenomena may reveal treads that could lead to a GDL with improved drainage characteristics.

The test section used in this study could be improved by including the effects of channel lands, compression, and air flow rates. This new design would more closely simulate actual fuel cell operation with air flow rates supplied at a variety of stoichiometries. The blockage of drainage paths by the lands may impact breakthrough dynamics and should be well characterized for modeling efforts. Compression of the GDL will reduce the pore space under the lands and thus significantly affect the local transport properties, including BT dynamics.

An interesting extension of this work would be to use the 3D geometry generated by the proposed algorithm to characterize subsurface pores. The generation algorithm could produce digital GDLs with similar properties to the tested commercial GDLs and would allow for evaluation of the 3D structure that would otherwise be unavailable. This extension may be able to provide trends on what is controlling the water flow paths and the associated dynamics. Further development of a mathematical model to predict and thoroughly describe the proposed mechanism would be of tremendous value for GDL transport modeling efforts.

References

[1] U. S. E. I. A. (eia.gov).

[2] R. Borup, J. Meyers, B. Pivovar, Y. S. Kim, R. Mukundan, N. Garland, D. Myers, M. Wilson, F. Garzon, D. Wood, P. Zelenay, K. More, K. Stroh, T. Zawodzinski, J. Boncella, J. E. McGrath, M. Inaba, K. Miyatake, M. Hori, K. Ota, Z. Ogumi, S. Miyata, A. Nishikata, Z. Siroma, Y. Uchimoto, K. Yasuda, K.-I. Kimijima, and N. Iwashita, "Scientific aspects of polymer electrolyte fuel cell durability and degradation," *Chemical Reviews*, vol. 107, no. 10, pp. 3904 – 3951, 2007.

[3] J. Thomas A. Zawodzinski, C. Derouin, S. Radzinski, R. J. Sherman, V. T. Smith, T. E. Springer, and S. Gottesfeld, "Water uptake by and transport through nafion 117 membranes," *Journal of The Electrochemical Society*, vol. 140, no. 4, pp. 1041–1047, 1993.

[4] C.-Y. Wang, "Fundamental models for fuel cell engineering," *Chemical Reviews*, vol. 104, no. 10, pp. 4727–4765, 2004.

[5] J. P. Owejan, J. J. Gagliardo, J. M. Sergi, S. G. Kandlikar, and T. A. Trabold, "Water management studies in pem fuel cells, part i: Fuel cell design and in situ water distributions," *International Journal of Hydrogen Energy*, vol. 34, no. 8, pp. 3436 – 3444, 2009.

[6] S. Kandlikar and Z. Lu, "Fundamental research needs in combined water and thermal management within a proton exchange membrane fuel cell stack under normal and

cold-start conditions," *Journal of Fuel Cell Science and Technology*, vol. 6, no. 4, pp. 044 001 (13 pp.) –, 2009.

[7] M. Daino, Z. Lu, J. LaManna, J. Owejan, T. Trabold, and S. Kandlikar, "Through-plane water transport visualization in an operating pem fuel cell by visible and infrared imaging," vol. 33, no. 1 PART 2, Las Vegas, NV, United states, 2010, pp. 1423 – 1433.

[8] M. M. Daino, Z. Lu, J. M. LaManna, J. P. Owejan, T. A. Trabold, and S. G. Kandlikar, "Through-plane water transport visualization in a pemfc by visible and infrared imaging," *Electrochemical and Solid-State Letters*, vol. 14, no. 6, pp. B51–B54, 2011.

[9] M. Mathias, J. Roth, J. Fleming, and W. Lehnert, *Handbook of Fuel Cells*, W. Vielstich, A. Lamm, and H. Gasteiger, Eds. John Wiley & Sons Ltd, 2003, vol. 3.

[10] S. G. Kandlikar, "Microscale and macroscale aspects of water management challenges in pem fuel cells," *Heat Transfer Engineering*, vol. 29, no. 7, pp. 575–587, 2008.

[11] N. Yousfi-Steiner, P. Mocoteguy, D. Candusso, D. Hissel, A. Hernandez, and A. Aslanides, "A review on pem voltage degradation associated with water management: Impacts, influent factors and characterization," *Journal of Power Sources*, vol. 183, no. 1, pp. 260–274, 2008.

[12] L. Hui, T. Yanghua, W. Zhenwei, S. Zheng, W. Shaohong, S. Datong, Z. Jianlu, K. Fatih, Z. Jiujun, W. Haijiang, L. Zhongsheng, R. Abouatallah, and A. Mazza, "A review of water flooding issues in the proton exchange membrane fuel cell," *Journal of Power Sources*, vol. 178, no. 1, pp. 103–17, 2008.

[13] P. K. Sinha, P. P. Mukherjee, and C.-Y. Wang, "Impact of gdl structure and wettability on water management in polymer electrolyte fuel cells," *Journal of Materials Chemistry*, vol. 17, no. 30, pp. 3089–3103, 2007.

[14] M. Sahimi, "Flow phenomena in rocks: from continuum models to fractals, percolation, cellular automata, and simulated annealing," *Reviews of Modern Physics*, vol. 65, no. 4, pp. 1393 – 534, 1993.

[15] A. Bazylak, V. Berejnov, B. Markicevic, D. Sinton, and N. Djilali, "Numerical and microfluidic pore networks: Towards designs for directed water transport in gdls," *Electrochimica Acta*, vol. 53, no. 26, pp. 7630 – 7637, 2008.

[16] L. Ceballos and M. Prat, "Invasion percolation with inlet multiple injections and the water management problem in proton exchange membrane fuel cells," *Journal of Power Sources*, vol. 195, no. 3, pp. 825 – 828, 2010.

[17] O. Chapuis, M. Prat, M. Quintard, E. Chane-Kane, O. Guillot, and N. Mayer, "Two-phase flow and evaporation in model fibrous media. application to the gas diffusion layer of pem fuel cells," *Journal of Power Sources*, vol. 178, no. 1, pp. 258 – 268, 2008.

[18] J. T. Gostick, M. W. Fowler, M. A. Ioannidis, M. D. Pritzker, Y. Volfkovich, and A. Sakars, "Capillary pressure and hydrophilic porosity in gas diffusion layers for polymer electrolyte fuel cells," *Journal of Power Sources*, vol. 156, no. 2, pp. 375 – 387, 2006.

[19] J. T. Gostick, M. A. Ioannidis, M. W. Fowler, and M. D. Pritzker, "Pore network modeling of fibrous gas diffusion layers for polymer electrolyte membrane fuel cells," *Journal of Power Sources*, vol. 173, no. 1, pp. 277 – 290, 2007.

[20] T. Koido, T. Furusawa, and K. Moriyama, "An approach to modeling two-phase transport in the gas diffusion layer of a proton exchange membrane fuel cell," *Journal of Power Sources*, vol. 175, no. 1, pp. 127 – 136, 2008.

[21] K.-J. Lee, J. H. Nam, and C.-J. Kim, "Steady saturation distribution in hydrophobic gas-diffusion layers of polymer electrolyte membrane fuel cells: A pore-network study," *Journal of Power Sources*, vol. 195, no. 1, pp. 130 – 141, 2010.

[22] K.-J. Lee, J. H. Kang, J. H. Nam, and C.-J. Kim, "Steady liquid water saturation distribution in hydrophobic gas-diffusion layers with engineered pore paths: an invasion-percolation pore-network analysis," *Journal of Power Sources*, vol. 195, no. 11, pp. 3508 – 12, 2010.

[23] K.-J. Lee, J. H. Nam, and C.-J. Kim, "Pore-network analysis of two-phase water transport in gas diffusion layers of polymer electrolyte membrane fuel cells," *Electrochimica Acta*, vol. 54, no. 4, pp. 1166 – 1176, 2009.

[24] B. Markicevic, A. Bazylak, and N. Djilali, "Determination of transport parameters for multiphase flow in porous gas diffusion electrodes using a capillary network model," *Journal of Power Sources*, vol. 171, no. 2, pp. 706 – 717, 2007.

[25] M. Rebai and M. Prat, "Scale effect and two-phase flow in a thin hydrophobic porous layer. application to water transport in gas diffusion layers of proton exchange membrane fuel cells," *Journal of Power Sources*, vol. 192, no. 2, pp. 534 – 543, 2009.

[26] P. K. Sinha and C.-Y. Wang, "Liquid water transport in a mixed-wet gas diffusion layer of a polymer electrolyte fuel cell," *Chemical Engineering Science*, vol. 63, no. 4, pp. 1081 – 1091, 2008.

[27] ——, "Pore-network modeling of liquid water transport in gas diffusion layer of a polymer electrolyte fuel cell," *Electrochimica Acta*, vol. 52, no. 28, pp. 7936 – 7945, 2007.

[28] V. P. Schulz, J. Becker, A. Wiegmann, P. P. Mukherjee, and C.-Y. Wang, "Modeling of two-phase behavior in the gas diffusion medium of pefcs via full morphology approach," *Journal of the Electrochemical Society*, vol. 154, no. 4, pp. B419 – B426, 2007.

[29] P. P. Mukherjee, C.-Y. Wang, and Q. Kang, "Mesoscopic modeling of two-phase behavior and flooding phenomena in polymer electrolyte fuel cells," *Electrochimica Acta*, vol. 54, no. 27, pp. 6861 – 6875, 2009.

[30] L. Hao and P. Cheng, "Lattice boltzmann simulations of anisotropic permeabilities in carbon paper gas diffusion layers," *Journal of Power Sources*, vol. 186, no. 1, pp. 104 – 114, 2009.

[31] J. Becker, V. Schulz, and A. Wiegmann, "Numerical determination of two-phase material parameters of a gas diffusion layer using tomography images," *Journal of Fuel Cell Science and Technology*, vol. 5, no. 2, pp. 021 006–1, 2008.

[32] J. Becker, R. Fluckiger, M. Reum, F. N. Buchi, F. Marone, and M. Stampanoni, "Determination of material properties of gas diffusion layers: Experiments and simulations using phase contrast tomographic microscopy," *Journal of The Electrochemical Society*, vol. 156, no. 10, pp. B1175–B1181, 2009.

[33] P. Rama, Y. Liu, R. Chen, H. Ostadi, K. Jiang, X. Zhang, R. Fisher, and M. Jeschke, "An x-ray tomography based lattice boltzmann simulation study on gas diffusion layers of polymer electrolyte fuel cells," *Journal of Fuel Cell Science and Technology*, vol. 7, no. 3, pp. 031 015 (12 pp.) –, 2010.

[34] A. Pfrang, D. Veyret, F. Sieker, and G. Tsotridis, "X-ray computed tomography of gas diffusion layers of pem fuel cells: Calculation of thermal conductivity," *International Journal of Hydrogen Energy*, vol. 35, no. 8, pp. 3751 – 3757, 2010.

[35] H. Ostadi, K. Jiang, and P. Prewett, "Micro/nano x-ray tomography reconstruction fine-tuning using scanning electron microscope images," *Micro and Nano Letters*, vol. 3, no. 4, pp. 106 – 109, 2008.

[36] J. Hinebaugh, Z. Fishman, and A. Bazylak, "Unstructured pore network modeling with heterogeneous pemfc gdl porosity distributions," *Journal of The Electrochemical Society*, vol. 157, no. 11, pp. B1651–B1657, 2010.

[37] Z. Fishman, J. Hinebaugh, and A. Bazylak, "Microscale tomography investigations of heterogeneous porosity distributions of pemfc gdls," *Journal of The Electrochemical Society*, vol. 157, no. 11, pp. B1643–B1650, 2010.

[38] M. Abdel-Ghani and G. Davies, "Simulation of non-woven fibre mats and the application to coalescers." *Chemical Engineering Science*, vol. 40, no. 1, pp. 117 – 129, 1985.

[39] K. Schladitz, S. Peters, D. Reinel-Bitzer, A. Wiegmann, and J. Ohser, "Design of acoustic trim based on geometric modeling and flow simulation for non-woven," *Computational Materials Science*, vol. 38, no. 1, pp. 56 – 66, 2006.

[40] B. Kenney, M. Valdmanis, C. Baker, J. Pharoah, and K. Karan, "Computation of tpb length, surface area and pore size from numerical reconstruction of composite solid oxide fuel cell electrodes," *Journal of Power Sources*, vol. 189, no. 2, pp. 1051 – 1059, 2009.

[41] G. Inoue, T. Yoshimoto, Y. Matsukuma, and M. Minemoto, "Development of simulated gas diffusion layer of polymer electrolyte fuel cells and evaluation of its structure," *Journal of Power Sources*, vol. 175, no. 1, pp. 145 – 158, 2008.

[42] R. Thiedmann, F. Fleischer, C. Hartnig, W. Lehnert, and V. Schmidt, "Stochastic 3d modeling of the gdl structure in pemfcs based on thin section detection," *Journal of the Electrochemical Society*, vol. 155, no. 4, pp. 391 – 9, 2008.

[43] R. Thiedmann, C. Hartnig, I. Manke, V. Schmidt, and W. Lehnert, "Local structural characteristics of pore space in gdls of pem fuel cells based on geometric 3d graphs," *Journal of the Electrochemical Society*, vol. 156, no. 11, pp. B1339 – B1347, 2009.

[44] Y. Wang, S. Cho, R. Thiedmann, V. Schmidt, W. Lehnert, and X. Feng, "Stochastic modeling and direct simulation of the diffusion media for polymer electrolyte fuel cells," *International Journal of Heat and Mass Transfer*, vol. 53, no. 5-6, pp. 1128 – 1138, 2010.

[45] P. P. Mukherjee and C.-Y. Wang, "Direct numerical simulation modeling of bilayer cathode catalyst layers in polymer electrolyte fuel cells," *Journal of the Electrochemical Society*, vol. 154, no. 11, pp. B1121 – B1131, 2007.

[46] S. H. Kim and H. Pitsch, "Reconstruction and effective transport properties of the catalyst layer in pem fuel cells," *Journal of the Electrochemical Society*, vol. 156, no. 6, pp. B673 – B681, 2009.

[47] Y. Ji, G. Luo, and C.-Y. Wang, "Pore-level liquid water transport through composite diffusion media of pemfc," *Journal of The Electrochemical Society*, vol. 157, no. 12, pp. B1753–B1761, 2010.

[48] G. Luo, Y. Ji, C.-Y. Wang, and P. K. Sinha, "Modeling liquid water transport in gas diffusion layers by topologically equivalent pore network," *Electrochimica Acta*, vol. 55, no. 19, pp. 5332 – 5341, 2010.

[49] N. Zamel, X. Li, J. Shen, J. Becker, and A. Wiegmann, "Estimating effective thermal conductivity in carbon paper diffusion media," *Chemical Engineering Science*, vol. 65, no. 13, pp. 3994 – 4006, 2010.

[50] I. Fatt, "The network model of porous media i. capillary pressure characteristics," *Trans. AIME*, vol. 207, pp. 144–159, 1956.

[51] ——, "The network model of porous media ii. dynamic properties of a single size tube network," *Trans. AIME*, vol. 207, pp. 160–163, 1956.

[52] ——, "The network model of porous media iii. dynamic properties of networks with tube radius distribution," *Trans. AIME*, vol. 207, pp. 164–181, 1956.

[53] G. Jerauld and S. Salter, "Effect of pore-structure on hysteresis in relative permeability and capillary pressure. pore-level modeling," *Transport in Porous Media*, vol. 5, no. 2, pp. 103 – 151, 1990.

[54] R. Lenormand, E. Touboul, and C. Zarcone, "Numerical models and experiments on immiscible displacements in porous media," *Journal of Fluid Mechanics*, vol. 189, pp. 165 – 87, 1988.

[55] V. Surasani, T. Metzger, and E. Tsotsas, "Consideration of heat transfer in pore network modelling of convective drying," *International Journal of Heat and Mass Transfer*, vol. 51, no. 9-10, pp. 2506 – 2518, 2008.

[56] A. G. Yiotis, I. N. Tsimpanogiannis, A. K. Stubos, and Y. C. Yortsos, "Pore-network study of the characteristic periods in the drying of porous materials," *Journal of Colloid and Interface Science*, vol. 297, no. 2, pp. 738 – 748, 2006.

[57] ——, "Coupling between external and internal mass transfer during drying of a porous medium," *Water Resources Research*, vol. 43, no. 6, pp. 1–12, 2007.

[58] B. Berkowitz and R. Ewing, "Percolation theory and network modeling applications in soil physics," *Surveys in Geophysics*, vol. 19, no. 1, pp. 23 – 72, 1998.

[59] M. J. Blunt, "Flow in porous media – pore-network models and multiphase flow," *Current Opinion in Colloid & Interface Science*, vol. 6, no. 3, pp. 197 – 207, 2001.

[60] M. Prat, "Recent advances in pore-scale models for drying of porous media," *Chemical Engineering Journal*, vol. 86, no. 1-2, pp. 153 – 164, 2002.

[61] Z. Lu, M. M. Daino, C. Rath, and S. G. Kandlikar, "Water management studies in pem fuel cells, part iii: Dynamic breakthrough and intermittent drainage characteristics from gdls with and without mpls," *International Journal of Hydrogen Energy*, vol. 35, no. 9, pp. 4222 – 4233, 2010.

[62] W. B. Haines, "Studies in the physical properties of soil. v. the hysteresis effect in capillary properties, and the modes of moisture distribution associated therewith," *The Journal of Agricultural Science*, vol. 20, no. 01, pp. 97–116, 1930.

[63] J. Wills, "Imaging water in pem fuel cells," *Fuel Cell Review*, vol. 2, no. 5, pp. 27–29, 2005.

[64] J. St-Pierre, "Pemfc in situ liquid-water-content monitoring status," *Journal of the Electrochemical Society*, vol. 154, no. 7, pp. 724–31, 2007.

[65] M. M. Daino and S. G. Kandlikar, "Evaluation of imaging techniques applied to water management research in pemfcs," no. PART A, Pohang, Korea, Republic of, 2009, pp. 467 – 479.

[66] A. Bazylak, "Liquid water visualization in pem fuel cells: A review," *International Journal of Hydrogen Energy*, vol. 34, no. 9, pp. 3845 – 3857, 2009.

[67] R. Mukundan and R. Borup, "Visualising liquid water in pem fuel cells using neutron imaging," *Fuel Cells*, vol. 9, no. 5, pp. 499 – 505, 2009.

[68] S. Tsushima and S. Hirai, "Magnetic resonance imaging of water in operating polymer electrolyte membrane fuel cells," *Fuel Cells*, vol. 9, no. 5, pp. 506 – 17, 2009.

[69] M. Rosli, D. Borman, D. Ingham, M. Ismail, L. Ma, and M. Pourkashanian, "Transparent pem fuel cells for direct visualization experiments," *Journal of Fuel Cell Science and Technology*, vol. 7, no. 6, pp. 061 015 (7 pp.) –, 2010.

[70] J. Cho, H.-S. Kim, and K. Min, "Transient response of a unit proton-exchange membrane fuel cell under various operating conditions," *Journal of Power Sources*, vol. 185, no. 1, pp. 118–28, 2008.

[71] X. Liu, H. Guo, and C. Ma, "Water flooding and two-phase flow in cathode channels of proton exchange membrane fuel cells," *Journal of Power Sources*, vol. 156, no. 2, pp. 267–280, 2006.

[72] X. Liu, H. Guo, F. Ye, and C. F. Ma, "Water flooding and pressure drop characteristics in flow channels of proton exchange membrane fuel cells," *Electrochimica Acta*, vol. 52, no. 11, pp. 3607–3614, 2007.

[73] H. P. Ma, H. M. Zhang, J. Hu, Y. H. Cai, and B. L. Yi, "Diagnostic tool to detect liquid water removal in the cathode channels of proton exchange membrane fuel cells," *Journal of Power Sources*, vol. 162, no. 1, pp. 469–473, 2006.

[74] H. Masuda, K. Ito, T. Oshima, and K. Sasaki, "Comparison between numerical simulation and visualization experiment on water behavior in single straight flow channel polymer electrolyte fuel cells," *Journal of Power Sources*, vol. 177, no. 2, pp. 303–313, 2008.

[75] T. Ous and C. Arcoumanis, "Visualisation of water droplets during the operation of pem fuel cells," *Journal of Power Sources*, vol. 173, no. 1, pp. 137–148, 2007.

[76] D. Spernjak, A. K. Prasad, and S. G. Advani, "Experimental investigation of liquid water formation and transport in a transparent single-serpentine pem fuel cell," *Journal of Power Sources*, vol. 170, no. 2, pp. 334–344, 2007.

[77] K. Sugiura, M. Nakata, T. Yodo, Y. Nishiguchi, M. Yamauchi, and Y. Itoh, "Evaluation of a cathode gas channel with a water absorption layer/waste channel in a pefc by using visualization technique," *Journal of Power Sources*, vol. 145, no. 2, pp. 526–533, 2005.

[78] A. Theodorakakos, T. Ous, M. Gavaises, J. M. Nouri, N. Nikolopoulos, and H. Yanagihara, "Dynamics of water droplets detached from porous surfaces of relevance to pem fuel cells," *Journal of Colloid and Interface Science*, vol. 300, no. 2, pp. 673–687, 2006.

[79] K. Tuber, D. Pocza, and C. Hebling, "Visualization of water buildup in the cathode of a transparent pem fuel cell," *Journal of Power Sources*, vol. 124, no. 2, pp. 403–414, 2003.

[80] I. S. Hussaini and C.-Y. Wang, "Visualization and quantification of cathode channel flooding in pem fuel cells," *Journal of Power Sources*, vol. 187, no. 2, pp. 444–451, 2009.

[81] C.-Y. Wen and G.-W. Huang, "Application of a thermally conductive pyrolytic graphite sheet to thermal management of a pem fuel cell," *Journal of Power Sources*, vol. 178, no. 1, pp. 132–140, 2008.

[82] X. G. Yang, F. Y. Zhang, A. L. Lubawy, and C. Y. Wang, "Visualization of liquid water transport in a pefc," *Electrochemical and Solid-State Letters*, vol. 7, no. 11, pp. 408–411, 2004.

[83] F. Y. Zhang, X. G. Yang, and C. Y. Wang, "Liquid water removal from a polymer electrolyte fuel cell," *Journal of the Electrochemical Society*, vol. 153, no. 2, pp. 225–32, 2006.

[84] T. Ous and C. Arcoumanis, "Visualisation of water accumulation in the flow channels of pemfc under various operating conditions," *Journal of Power Sources*, vol. 187, no. 1, pp. 182–9, 2009.

[85] A. M. Lpez, F. Barreras, A. Lozano, J. A. Garca, L. Valio, and R. Mustata, "Comparison of water management between two bipolar plate flow-field geometries in pro-

ton exchange membrane fuel cells at low-density current range," *Journal of Power Sources*, vol. 192, no. 1, pp. 94 – 99, 2009.

[86] J. M. Sergi and S. G. Kandlikar, "Quantification and characterization of water coverage in pemfc gas channels using simultaneous anode and cathode visualization and image processing," *International Journal of Hydrogen Energy*, vol. In Press, Corrected Proof, pp. –, 2011.

[87] S. Ge and C.-Y. Wang, "Liquid water formation and transport in the pefc anode," *Journal of the Electrochemical Society*, vol. 154, no. 10, pp. 998–1005, 2007.

[88] F.-Y. Zhang, D. Spernjak, A. K. Prasad, and S. G. Advani, "In situ characterization of the catalyst layer in a polymer electrolyte membrane fuel cell," *Journal of the Electrochemical Society*, vol. 154, no. 11, pp. 1152–1157, 2007.

[89] S. Ge and C.-Y. Wang, "In situ imaging of liquid water and ice formation in an operating pefc during cold start," *Electrochemical and Solid-State Letters*, vol. 9, no. 11, pp. 499–503, 2006.

[90] ——, "Characteristics of subzero startup and water/ice formation on the catalyst layer in a polymer electrolyte fuel cell," *Electrochimica Acta*, vol. 52, no. 14, pp. 4825–4835, 2007.

[91] K. Nishida, T. Murakami, S. Tsushima, and S. Hirai, "Microscopic visualization of state and behavior of liquid water in a gas diffusion layer of pefc," *Electrochemistry*, vol. 75, no. 2, pp. 149–151, 2007.

[92] S. Kandlikar, Z. Lu, T. Lin, D. Cooke, and M. Daino, "Uneven gas diffusion layer intrusion in gas channel arrays of proton exchange membrane fuel cell and its effects on flow distribution," *Journal of Power Sources*, vol. 194, no. 1, pp. 328 – 37, 2009.

[93] Z. Lu, S. Kandlikar, C. Rath, M. Grimm, W. Domigan, A. White, M. Hardbarger, J. Owejan, and T. Trabold, "Water management studies in pem fuel cells, part ii: ex situ investigation of flow maldistribution, pressure drop and two-phase flow pattern in gas channels," *International Journal of Hydrogen Energy*, vol. 34, no. 8, pp. 3445 – 56, 2009.

[94] Z. Lu, C. Rath, G. Zhang, and S. G. Kandlikar, "Water management studies in pem fuel cells, part iv: Effects of channel surface wettability, geometry and orientation on the two-phase flow in parallel gas channels," *International Journal of Hydrogen Energy*, vol. 36, no. 16, pp. 9864 – 9875, 2011.

[95] J. Chen, "Dominant frequency of pressure drop signal as a novel diagnostic tool for the water removal in proton exchange membrane fuel cell flow channel," *Journal of Power Sources*, vol. 195, no. 4, pp. 1177 – 81, 2010.

[96] ——, "Experimental study on the two phase flow behavior in pem fuel cell parallel channels with porous media inserts," *Journal of Power Sources*, vol. 195, no. 4, pp. 1122 – 9, 2010.

[97] L. jun Yu, W. can Chen, M. jun Qin, and G. po Ren, "Experimental research on water management in proton exchange membrane fuel cells," *Journal of Power Sources*, vol. 189, no. 2, pp. 882 – 887, 2009.

[98] S. G. Kandlikar, Z. Lu, W. E. Domigan, A. D. White, and M. W. Benedict, "Measurement of flow maldistribution in parallel channels and its application to ex-situ and in-situ experiments in pemfc water management studies," *International Journal of Heat and Mass Transfer*, vol. 52, no. 7-8, pp. 1741–1752, 2009.

[99] S. Basu, J. Li, and C.-Y. Wang, "Two-phase flow and maldistribution in gas channels of a polymer electrolyte fuel cell," *Journal of Power Sources*, vol. 187, no. 2, pp. 431–443, 2009.

[100] J. Sergi, Z. Lu, and S. Kandlikar, "Two-phase flow characteristics in the cathode channels of an operational pem fuel cell with visual access," in *Seventh International Conference on Nanochannels, Microchannels, and Minichannels*, vol. ICNMM2009-82140. ASME, 2009.

[101] L. G. Hector Jr, Y.-H. Lai, W. Tong, and M. J. Lukitsch, "Strain accumulation in polymer electrolyte membrane and membrane electrode assembly materials during a single hydration/dehydration cycle," *Journal of Fuel Cell Science and Technology*, vol. 4, no. 1, pp. 19–28, 2007.

[102] Y.-H. Lai, Y. Li, and J. A. Rock, "A novel full-field experimental method to measure the local compressibility of gas diffusion media," *Journal of Power Sources*, vol. 195, no. 10, pp. 3215 – 3223, 2010.

[103] E. Kimball, J. Benziger, and Y. Kevrekidis, "Effects of gdl structure with an efficient approach to the management of liquid water in pem fuel cells," *Fuel Cells*, vol. 10, no. 4, pp. 530 – 44, 2010.

[104] K. Jiao, J. Park, and X. Li, "Experimental investigations on liquid water removal from the gas diffusion layer by reactant flow in a pem fuel cell," *Applied Energy*, vol. 87, no. 9, pp. 2770 – 7, 2010.

[105] V. Berejnov, D. Sinton, and N. Djilali, "Structure of porous electrodes in polymer electrolyte membrane fuel cells: An optical reconstruction technique," *Journal of Power Sources*, vol. 195, no. 7, pp. 1936 – 1939, 2010.

[106] J. B. Pawley, *Handbook of Biological Confocal Microscopy*, 3rd ed., J. B. Pawley, Ed. Springer Science+Business Media, Inc., 2006.

[107] D. B. Murphy, *Fundamentals of light microscopy and electronic imaging*. New York: Wiley-Liss,Inc., 2001.

[108] R. H. Webb, "Confocal optical microscopy," *Reports on Progress in Physics*, vol. 59, no. 3, pp. 427–71, 1996.

[109] A. Hakenjos, H. Muenter, U. Wittstadt, and C. Hebling, "A pem fuel cell for combined measurement of current and temperature distribution, and flow field flooding," *Journal of Power Sources*, vol. 131, no. 1-2, pp. 213 – 216, 2004.

[110] Y. Ishikawa, T. Morita, K. Nakata, K. Yoshida, and M. Shiozawa, "Behavior of water below the freezing point in pefcs," *Journal of Power Sources*, vol. 163, no. 2, pp. 708–712, 2007.

[111] Y. Ishikawa, H. Hamada, M. Uehara, and M. Shiozawa, "Super-cooled water behavior inside polymer electrolyte fuel cell cross-section below freezing temperature," *Journal of Power Sources*, vol. 179, no. 2, pp. 547–552, 2008.

[112] R. Shimoi, M. Masuda, K. Fushinobu, Y. Kozawa, and K. Okazaki, "Visualization of the membrane temperature field of a polymer electrolyte fuel cell," *Journal of Energy Resources Technology, Transactions of the ASME*, vol. 126, no. 4, pp. 258–261, 2004.

[113] I. H. Son, A. M. Lane, and D. T. Johnson, "The study of the deactivation of water-pretreated pt/-al 2o3 for low-temperature selective co oxidation in hydrogen," *Journal of Power Sources*, vol. 124, no. 2, pp. 415–419, 2003.

[114] L. Martins, J. Gardolinski, J. Vargas, J. Ordonez, S. Amico, and M. Forte, "The experimental validation of a simplified pemfc simulation model for design and optimization purposes," *Applied Thermal Engineering*, vol. 29, no. 14-15, pp. 3036 – 3048, 2009.

[115] M. Matian, A. Marquis, and N. Brandon, "Application of thermal imaging to validate a heat transfer model for polymer electrolyte fuel cells," *International Journal of Hydrogen Energy*, vol. 35, no. 22, pp. 12 308 – 12 316, 2010.

[116] S. Basu, H. Xu, M. W. Renfro, and B. M. Cetegen, "In situ optical diagnostics for measurements of water vapor partial pressure in a pem fuel cell," *Journal of Fuel Cell Science and Technology*, vol. 3, no. 1, pp. 1–7, 2006.

[117] K. Fushinobu, K. Shimizu, N. Miki, and K. Okazaki, "Optical measurement technique of water contents in polymer membrane for pefcs," *Journal of Fuel Cell Science and Technology*, vol. 3, no. 1, pp. 13–17, 2006.

[118] S. Morita, Y. Jojima, Y. Miyata, and K. Kitagawa, "Near-infrared imaging of water in a polymer electrolyte membrane during a fuel cell operation," *Analytical Chemistry*, vol. 82, no. 22, pp. 9221 – 9224, 2010.

[119] A. Bazylak, D. Sinton, and N. Djilali, "Dynamic water transport and droplet emergence in pemfc gas diffusion layers," *Journal of Power Sources*, vol. 176, no. 1, pp. 240–246, 2008.

[120] A. Bazylak, D. Sinton, Z. S. Liu, and N. Djilali, "Effect of compression on liquid water transport and microstructure of pemfc gas diffusion layers," *Journal of Power Sources*, vol. 163, no. 2, pp. 784–792, 2007.

[121] B. Gao, T. S. Steenhuis, Y. Zevi, J.-Y. Parlange, R. N. Carter, and T. A. Trabold, "Visualization of unstable water flow in a fuel cell gas diffusion layer," *Journal of Power Sources*, vol. 190, no. 2, pp. 493 – 498, 2009.

[122] S. Litster, D. Sinton, and N. Djilali, "Ex situ visualization of liquid water transport in pem fuel cell gas diffusion layers," *Journal of Power Sources*, vol. 154, no. 1, pp. 95–105, 2006.

[123] J. E. Steinbrenner, C. H. Hidrovo, F.-M. Wang, S. Vigneron, E. S. Lee, T. A. Kramer, C.-H. Cheng, J. K. Eaton, and K. E. Goodson, "Measurement and modeling of liquid film thickness evolution in stratified two-phase microchannel flows," *Applied Thermal Engineering*, vol. 27, no. 10, pp. 1722–1727, 2007.

[124] B. R. Friess and M. Hoorfar, "Measurement of average contact angles of gas diffusion layers using a novel fluorescence microscopy method," *Journal of Fuel Cell Science and Technology*, vol. 8, no. 2, p. 021006, 2011.

[125] B. Friess and M. Hoorfar, "Measurement of internal wettability of gas diffusion porous media of proton exchange membrane fuel cells," *Journal of Power Sources*, vol. 195, no. 15, pp. 4736 – 4742, 2010.

[126] D. E. Moilanen, D. B. Spry, and M. D. Fayer, "Water dynamics and proton transfer in nafion fuel cell membranes," *Langmuir*, vol. 24, no. 8, pp. 3690–3698, 2008.

[127] Y. P. Patil, T. A. P. Seery, M. T. Shaw, and R. S. Parnas, "In situ water sensing in a nafion membrane by fluorescence spectroscopy," *Industrial and Engineering Chemistry Research*, vol. 44, no. 16, pp. 6141–6147, 2005.

[128] D. B. Spry, A. Goun, K. Glusac, D. E. Moilanen, and M. D. Fayer, "Proton transport and the water environment in nafion fuel cell membranes and aot reverse micelles," *Journal of the American Chemical Society*, vol. 129, no. 26, pp. 8122–8130, 2007.

[129] A. Esposito, A. Montello, Y. Guezennec, and C. Pianese, "Experimental investigation of water droplet-air flow interaction in a non-reacting pem fuel cell channel," *Journal of Power Sources*, vol. 195, no. 9, pp. 2691 – 9, 2010.

[130] J. Z. Fishman, H. Leung, and A. Bazylak, "Droplet pinning by pem fuel cell gdl surfaces," *International Journal of Hydrogen Energy*, vol. 35, no. 17, pp. 9144 – 9150, 2010.

[131] V. R. Albertini, B. Paci, A. Generosi, S. Panero, M. A. Navarra, and M. Di Michiel, "In situ xrd studies of the hydration degree of the polymeric membrane in a fuel cell," *Electrochemical and Solid-State Letters*, vol. 7, no. 12, pp. 519–521, 2004.

[132] C. Hartnig, I. Manke, R. Kuhn, N. Kardjilov, J. Banhart, and W. Lehnert, "Cross-sectional insight in the water evolution and transport in polymer electrolyte fuel cells," *Applied Physics Letters*, vol. 92, no. 13, pp. 134 106–1, 2008.

[133] C. Hartnig, I. Manke, R. Kuhn, S. Kleinau, J. Goebbels, and J. Banhart, "High-resolution in-plane investigation of the water evolution and transport in pem fuel cells," *Journal of Power Sources*, vol. 188, no. 2, pp. 468–474, 2009.

[134] I. Manke, C. Hartnig, M. Grunerbel, W. Lehnert, N. Kardjilov, A. Haibel, A. Hilger, J. Banhart, and H. Riesemeier, "Investigation of water evolution and transport in fuel cells with high resolution synchrotron x-ray radiography," *Applied Physics Letters*, vol. 90, no. 17, pp. 174 105–1, 2007.

[135] T. Mukaide, S. Mogi, J. Yamamoto, A. Morita, S. Koji, K. Takada, K. Uesugi, K. Kajiwara, and T. Noma, "In situ observation of water distribution and behaviour in a polymer electrolyte fuel cell by synchrotron x-ray imaging," *Journal of Synchrotron Radiation*, vol. 15, no. 4, pp. 329–334, 2008.

[136] I. Manke, C. Hartnig, N. Kardjilov, H. Riesemeier, J. Goebbels, R. Kuhn, P. Krger, and J. Banhart, "In situ synchrotron x-ray radiography investigations of water transport in pemfuel cells," *Fuel Cells*, vol. 10, no. 1, pp. 26–34, 2010.

[137] P. Krger, H. Markter, J. Haumann, M. Klages, T. Arlt, J. Banhart, C. Hartnig, I. Manke, and J. Scholta, "Synchrotron x-ray tomography for investigations of water distribution in polymer electrolyte membrane fuel cells," *Journal of Power Sources*, vol. 196, no. 12, pp. 5250 – 5255, 2011.

[138] S. J. Lee, N.-Y. Lim, S. Kim, G.-G. Park, and C.-S. Kim, "X-ray imaging of water distribution in a polymer electrolyte fuel cell," *Journal of Power Sources*, vol. 185, no. 2, pp. 867–870, 2008.

[139] P. K. Sinha, P. Halleck, and C.-Y. Wang, "Quantification of liquid water saturation in a pem fuel cell diffusion medium using x-ray microtomography," *Electrochemical and Solid-State Letters*, vol. 9, no. 7, pp. 344–348, 2006.

[140] J. Mahadevan, M. M. Sharma, and Y. C. Yortsos, "Water removal from porous media by gas injection: Experiments and simulation," *Transport in Porous Media*, vol. 66, no. 3, pp. 287–309, 2007.

[141] A. Pfrang, D. Veyret, G. J. Janssen, and G. Tsotridis, "Imaging of membrane electrode assemblies of proton exchange membrane fuel cells by x-ray computed tomography," *Journal of Power Sources*, vol. 196, no. 12, pp. 5272 – 5276, 2011.

[142] J. Bedet, G. Maranzana, S. Leclerc, O. Lottin, C. Moyne, D. Stemmelen, P. Mutzenhardt, and D. Canet, "Magnetic resonance imaging of water distribution and production in a 6cm2 pemfc under operation," *International Journal of Hydrogen Energy*, vol. 33, no. 12, pp. 3146–9, 2008.

[143] Z. Dunbar and R. I. Masel, "Quantitative mri study of water distribution during operation of a pem fuel cell using teflon [registered trademark] flow fields," *Journal of Power Sources*, vol. 171, no. 2, pp. 678–687, 2007.

[144] Z. W. Dunbar and R. I. Masel, "Magnetic resonance imaging investigation of water accumulation and transport in graphite flow fields in a polymer electrolyte membrane fuel cell: Do defects control transport?" *Journal of Power Sources*, vol. 182, no. 1, pp. 76–82, 2008.

[145] K. W. Feindel, S. H. Bergens, and R. E. Wasylishen, "Insights into the distribution of water in a self-humidifying h 2/o2 proton-exchange membrane fuel cell using 1h nmr microscopy," *Journal of the American Chemical Society*, vol. 128, no. 43, pp. 14 192–14 199, 2006.

[146] ——, "Use of hydrogen-deuterium exchange for contrast in 1h nmr microscopy investigations of an operating pem fuel cell," *Journal of Power Sources*, vol. 173, no. 1, pp. 86–95, 2007.

[147] K. R. Minard, V. V. Viswanathan, P. D. Majors, L.-Q. Wang, and P. C. Rieke, "Magnetic resonance imaging (mri) of pem dehydration and gas manifold flooding during continuous fuel cell operation," *Journal of Power Sources*, vol. 161, no. 2, pp. 856–863, 2006.

[148] K. Teranishi, S. Tsushima, and S. Hirai, "Study of the effect of membrane thickness on the performance of polymer electrolyte fuel cells by water distribution in a membrane," *Electrochemical and Solid-State Letters*, vol. 8, no. 6, pp. 281–284, 2005.

[149] ——, "Analysis of water transport in pefcs by magnetic resonance imaging measurement," *Journal of the Electrochemical Society*, vol. 153, no. 4, pp. 664–668, 2006.

[150] S. Tsushima, K. Teranishi, and S. Hirai, "Magnetic resonance imaging of the water distribution within a polymer electrolyte membrane in fuel cells," *Electrochemical and Solid-State Letters*, vol. 7, no. 9, pp. 269–272, 2004.

[151] S. Tsushima, K. Teranishi, K. Nishida, and S. Hirai, "Water content distribution in a polymer electrolyte membrane for advanced fuel cell system with liquid water supply," *Magnetic Resonance Imaging*, vol. 23, no. 2, pp. 255–8, 2005.

[152] S. Tsushima, K. Teranishi, and S. Hirai, "Water diffusion measurement in fuel-cell spe membrane by nmr," *Energy*, vol. 30, no. 2-4 SPEC ISS, pp. 235–245, 2005.

[153] Z. Zhang, J. Martin, J. Wu, H. Wang, K. Promislow, and B. J. Balcom, "Magnetic resonance imaging of water content across the nafion membrane in an operational pem fuel cell," *Journal of Magnetic Resonance*, vol. 193, no. 2, pp. 259–266, 2008.

[154] Z. Zhang, A. E. Marble, B. MacMillan, K. Promislow, J. Martin, W. Haijiang, and B. J. Balcom, "Spatial and temporal mapping of water content across nafion membranes under wetting and drying conditions," *Journal of Magnetic Resonance*, vol. 194, no. 2, pp. 245–53, 2008.

[155] T. Suzuki, Y. Tabuchi, S. Tsushima, and S. Hirai, "Measurement of water content distribution in catalyst coated membranes under water permeation conditions by magnetic resonance imaging," *International Journal of Hydrogen Energy*, vol. 36, no. 9, pp. 5479 – 5486, 2011.

[156] M. Wang, K. W. Feindel, S. H. Bergens, and R. E. Wasylishen, "In situ quantification of the in-plane water content in the nafion membrane of an operating polymer-electrolyte membrane fuel cell using 1h micro-magnetic resonance imaging experiments," *Journal of Power Sources*, vol. 195, no. 21, pp. 7316 – 7322, 2010.

[157] P. Boillat, D. Kramer, B. C. Seyfang, G. Frei, E. Lehmann, G. G. Scherer, A. Wokaun, Y. Ichikawa, Y. Tasaki, and K. Shinohara, "In situ observation of the water distribution across a pefc using high resolution neutron radiography," *Electrochemistry Communications*, vol. 10, no. 4, pp. 546–550, 2008.

[158] D. Spernjak, S. G. Advani, and A. K. Prasad, "Simultaneous neutron and optical imaging in pem fuel cells," *Journal of the Electrochemical Society*, vol. 156, no. 1, pp. 109–17, 2009.

[159] Y.-S. Chen, H. Peng, D. S. Hussey, D. L. Jacobson, D. T. Tran, T. Abdel-Baset, and M. Biernacki, "Water distribution measurement for a pemfc through neutron radiography," *Journal of Power Sources*, vol. 170, no. 2, pp. 376–386, 2007.

[160] C. Hartnig, I. Manke, N. Kardjilov, A. Hilger, M. Grunerbel, J. Kaczerowski, J. Banhart, and W. Lehnert, "Combined neutron radiography and locally resolved current

density measurements of operating pem fuel cells," *Journal of Power Sources*, vol. 176, no. 2, pp. 452–459, 2008.

[161] M. A. Hickner, N. P. Siegel, K. S. Chen, D. N. McBrayer, D. S. Hussey, D. L. Jacobson, and M. Arif, "Real-time imaging of liquid water in an operating proton exchange membrane fuel cell," *Journal of the Electrochemical Society*, vol. 153, no. 5, pp. 902–908, 2006.

[162] T. Kim, C. Sim, and M. Kim, "Research on water discharge characteristics of pem fuel cells by using neutron imaging technology at the nrf, hanaro," *Applied Radiation and Isotopes*, vol. 66, no. 5, pp. 593–605, 2008.

[163] T. Kim, J. Kim, C. Sim, S. Lee, M. Kaviany, S. Son, and M. Kim, "Experimental approaches for distribution and behavior of water in pemfc under flow direction and differential pressure using neutron imaging technique," *Nuclear Instruments and Methods in Physics Research, Section A: Accelerators, Spectrometers, Detectors and Associated Equipment*, vol. 600, no. 1, pp. 325–327, 2009.

[164] J. J. Kowal, A. Turhan, K. Heller, J. Brenizer, and M. M. Mench, "Liquid water storage, distribution, and removal from diffusion media in pefcs," *Journal of the Electrochemical Society*, vol. 153, no. 10, pp. 1971–1978, 2006.

[165] D. Kramer, J. Zhang, R. Shimoi, E. Lehmann, A. Wokaun, K. Shinohara, and G. G. Scherer, "In situ diagnostic of two-phase flow phenomena in polymer electrolyte fuel cells by neutron imaging: Part a. experimental, data treatment, and quantification," *Electrochimica Acta*, vol. 50, no. 13, pp. 2603–2614, 2005.

[166] D. J. Ludlow, C. M. Calebrese, S. H. Yu, C. S. Dannehy, D. L. Jacobson, D. S. Hussey, M. Arif, M. K. Jensen, and G. A. Eisman, "Pem fuel cell membrane hydration measurement by neutron imaging," *Journal of Power Sources*, vol. 162, no. 1, pp. 271–278, 2006.

[167] I. Manke, C. Hartnig, N. Kardjilov, M. Messerschmidt, A. Hilger, M. Strobl, W. Lehnert, and J. Banhart, "Characterization of water exchange and two-phase flow in porous gas diffusion materials by hydrogen-deuterium contrast neutron radiography," *Applied Physics Letters*, vol. 92, no. 24, p. 244101, 2008.

[168] J. P. Owejan, T. A. Trabold, D. L. Jacobson, D. R. Baker, D. S. Hussey, and M. Arif, "In situ investigation of water transport in an operating pem fuel cell using neutron radiography: Part 2 - transient water accumulation in an interdigitated cathode flow field," *International Journal of Heat and Mass Transfer*, vol. 49, no. 25-26, pp. 4721–4731, 2006.

[169] J. P. Owejan, T. A. Trabold, D. L. Jacobson, M. Arif, and S. G. Kandlikar, "Effects of flow field and diffusion layer properties on water accumulation in a pem fuel cell," *International Journal of Hydrogen Energy*, vol. 32, no. 17, pp. 4489–4502, 2007.

[170] J. P. Owejan, T. A. Trabold, J. J. Gagliardo, D. L. Jacobson, R. N. Carter, D. S. Hussey, and M. Arif, "Voltage instability in a simulated fuel cell stack correlated to cathode water accumulation," *Journal of Power Sources*, vol. 171, no. 2, pp. 626–633, 2007.

[171] J. Park, L. Xianguo, D. Tran, T. Abdel-Baset, D. S. Hussey, D. L. Jacobson, and M. Arif, "Neutron imaging investigation of liquid water distribution in and the performance of a pem fuel cell," *International Journal of Hydrogen Energy*, vol. 33, no. 13, pp. 3373–84, 2008.

[172] N. Pekula, K. Heller, P. A. Chuang, A. Turhan, M. M. Mench, J. S. Brenizer, and K. Unlu, "Study of water distribution and transport in a polymer electrolyte fuel cell using neutron imaging," *Nuclear Instruments and Methods in Physics Research, Section A: Accelerators, Spectrometers, Detectors and Associated Equipment*, vol. 542, no. 1-3, pp. 134–141, 2005.

[173] R. Satija, D. L. Jacobson, M. Arif, and S. A. Werner, "In situ neutron imaging technique for evaluation of water management systems in operating pem fuel cells," *Journal of Power Sources*, vol. 129, no. 2, pp. 238–245, 2004.

[174] J. B. Siegel, D. A. McKay, A. G. Stefanopoulou, D. S. Hussey, and D. L. Jacobson, "Measurement of liquid water accumulation in a pemfc with dead-ended anode," *Journal of the Electrochemical Society*, vol. 155, no. 11, pp. 1168–78, 2008.

[175] A. Turhan, K. Heller, J. S. Brenizer, and M. M. Mench, "Quantification of liquid water accumulation and distribution in a polymer electrolyte fuel cell using neutron imaging," *Journal of Power Sources*, vol. 160, no. 2 SPEC ISS, pp. 1195–1203, 2006.

[176] ——, "Passive control of liquid water storage and distribution in a pefc through flow-field design," *Journal of Power Sources*, vol. 180, no. 2, pp. 773–783, 2008.

[177] J. Zhang, D. Kramer, R. Shimoi, Y. Ono, E. Lehmann, A. Wokaun, K. Shinohara, and G. G. Scherer, "In situ diagnostic of two-phase flow phenomena in polymer electrolyte fuel cells by neutron imaging: Part b. material variations," *Electrochimica Acta*, vol. 51, no. 13, pp. 2715–2727, 2006.

[178] M. A. Hickner, N. P. Siegel, K. S. Chen, D. S. Hussey, D. L. Jacobson, and M. Arif, "Understanding liquid water distribution and removal phenomena in an operating pemfc via neutron radiography," *Journal of the Electrochemical Society*, vol. 155, no. 3, pp. 294–302, 2008.

[179] D. Spernjak, A. K. Prasad, and S. G. Advani, "In situ comparison of water content and dynamics in parallel, single-serpentine, and interdigitated flow fields of polymer electrolyte membrane fuel cells," *Journal of Power Sources*, vol. 195, no. 11, pp. 3553 – 3568, 2010.

[180] J. Gagliardo, J. Owejan, T. Trabold, and T. Tighe, "Neutron radiography characterization of an operating proton exchange membrane fuel cell with localized current distribution measurements," *Nuclear Instruments and Methods in Physics Research Section A: Accelerators, Spectrometers, Detectors and Associated Equipment*, vol. 605, no. 1-2, pp. 115 – 118, 2009.

[181] M. A. Hickner, N. P. Siegel, K. S. Chen, D. S. Hussey, D. L. Jacobson, and M. Arif, "In situ high-resolution neutron radiography of cross-sectional liquid water profiles in proton exchange membrane fuel cells," *Journal of the Electrochemical Society*, vol. 155, no. 4, pp. 427–434, 2008.

[182] D. S. Hussey, D. L. Jacobson, M. Arif, J. P. Owejan, J. J. Gagliardo, and T. A. Trabold, "Neutron images of the through-plane water distribution of an operating pem fuel cell," *Journal of Power Sources*, vol. 172, no. 1, pp. 225–228, 2007.

[183] A. Z. Weber and M. A. Hickner, "Modeling and high-resolution-imaging studies of water-content profiles in a polymer-electrolyte-fuel-cell membrane-electrode assembly," *Electrochimica Acta*, vol. 53, no. 26, pp. 7668–7674, 2008.

[184] P. Quan, M.-C. Lai, D. S. Hussey, D. L. Jacobson, A. Kumar, and S. Hirano, "Time-resolved water measurement in a pem fuel cell using high-resolution neutron imaging technique," *Journal of Fuel Cell Science and Technology*, vol. 7, no. 5, p. 051009, 2010.

[185] R. J. Bellows, M. Y. Lin, M. Arif, A. K. Thompson, and D. Jacobson, "Neutron imaging technique for in situ measurement of water transport gradients within nafion in polymer electrolyte fuel cells," *Journal of the Electrochemical Society*, vol. 146, no. 3, pp. 1099–103, 1999.

[186] E. Medici and J. Allen, "Existence of the phase drainage diagram in proton exchange membrane fuel cell fibrous diffusion media," *Journal of Power Sources*, vol. 191, no. 2, pp. 417 – 427, 2009.

[187] J. D. Fairweather, P. Cheung, J. St-Pierre, and D. T. Schwartz, "A microfluidic approach for measuring capillary pressure in pemfc gas diffusion layers," *Electrochemistry Communications*, vol. 9, no. 9, pp. 2340 – 2345, 2007.

[188] J. T. Gostick, M. A. Ioannidis, M. W. Fowler, and M. D. Pritzker, "Direct measurement of the capillary pressure characteristics of water-air-gas diffusion layer systems for pem fuel cells," *Electrochemistry Communications*, vol. 10, no. 10, pp. 1520 – 1523, 2008.

[189] P. Cheung, J. D. Fairweather, and D. T. Schwartz, "Characterization of internal wetting in polymer electrolyte membrane gas diffusion layers," *Journal of Power Sources*, vol. 187, no. 2, pp. 487 – 492, 2009.

[190] A. Turhan, K. Heller, J. Brenizer, and M. Mench, "Quantification of liquid water accumulation and distribution in a polymer electrolyte fuel cell using neutron imaging," *Journal of Power Sources*, vol. 160, no. 2, pp. 1195 – 1203, 2006.

[191] J. H. Nam, K.-J. Lee, G.-S. Hwang, C.-J. Kim, and M. Kaviany, "Microporous layer for water morphology control in pemfc," *International Journal of Heat and Mass Transfer*, vol. 52, no. 11-12, pp. 2779 – 2791, 2009.

[192] J. H. Nam and M. Kaviany, "Effective diffusivity and water-saturation distribution in single- and two-layer pemfc diffusion medium," *International Journal of Heat and Mass Transfer*, vol. 46, no. 24, pp. 4595 – 4611, 2003.

[193] U. Pasaogullari and C. Y. Wang, "Liquid water transport in gas diffusion layer of polymer electrolyte fuel cells," *Journal of The Electrochemical Society*, vol. 151, no. 3, pp. A399–A406, 2004.

[194] A. Z. Weber, R. M. Darling, and J. Newman, "Modeling two-phase behavior in pefcs," *Journal of The Electrochemical Society*, vol. 151, no. 10, pp. A1715–A1727, 2004.

[195] L. Pisani, G. Murgia, M. Valentini, and B. D'Aguanno, "A working model of polymer electrolyte fuel cells," *Journal of The Electrochemical Society*, vol. 149, no. 7, pp. A898–A904, 2002.

[196] F. A. L. Dullien, *Porous Media: Fluid Transport and Pore Structure*. Academic Press, 1991.

[197] Z. Qi and A. Kaufman, "Improvement of water management by a microporous sublayer for pem fuel cells," *Journal of Power Sources*, vol. 109, no. 1, pp. 38 – 46, 2002.

[198] L. Jordan, A. Shukla, T. Behrsing, N. Avery, B. Muddle, and M. Forsyth, "Effect of diffusion-layer morphology on the performance of polymer electrolyte fuel cells operating at atmospheric pressure," *Journal of Applied Electrochemistry*, vol. 30, pp. 641–646, 2000.

[199] C. S. Kong, D.-Y. Kim, H.-K. Lee, Y.-G. Shul, and T.-H. Lee, "Influence of pore-size distribution of diffusion layer on mass-transport problems of proton exchange membrane fuel cells," *Journal of Power Sources*, vol. 108, no. 1-2, pp. 185 – 191, 2002.

[200] X. Wang, H. Zhang, J. Zhang, H. Xu, Z. Tian, J. Chen, H. Zhong, Y. Liang, and B. Yi, "Micro-porous layer with composite carbon black for pem fuel cells," *Electrochimica Acta*, vol. 51, no. 23, pp. 4909 – 4915, 2006.

[201] X. Wang, H. Zhang, J. Zhang, H. Xu, X. Zhu, J. Chen, and B. Yi, "A bi-functional micro-porous layer with composite carbon black for pem fuel cells," *Journal of Power Sources*, vol. 162, no. 1, pp. 474 – 479, 2006.

[202] G.-G. Park, Y.-J. Sohn, S.-D. Yim, T.-H. Yang, Y.-G. Yoon, W.-Y. Lee, K. Eguchi, and C.-S. Kim, "Adoption of nano-materials for the micro-layer in gas diffusion layers of pemfcs," *Journal of Power Sources*, vol. 163, no. 1, pp. 113 – 118, 2006.

[203] H. Tang, S. Wang, M. Pan, and R. Yuan, "Porosity-graded micro-porous layers for polymer electrolyte membrane fuel cells," *Journal of Power Sources*, vol. 166, no. 1, pp. 41 – 46, 2007.

[204] A. Z. Weber and J. Newman, "Effects of microporous layers in polymer electrolyte fuel cells," *Journal of The Electrochemical Society*, vol. 152, no. 4, pp. A677–A688, 2005.

[205] G. Lin and T. V. Nguyen, "A two-dimensional two-phase model of a pem fuel cell," *Journal of The Electrochemical Society*, vol. 153, no. 2, pp. A372–A382, 2006.

[206] K. Karan, H. Atiyeh, A. Phoenix, E. Halliop, J. Pharoah, and B. Peppley, "An experimental investigation of water transport in pemfcs," *Electrochemical and Solid-State Letters*, vol. 10, no. 2, pp. B34–B38, 2007.

[207] H. K. Atiyeh, K. Karan, B. Peppley, A. Phoenix, E. Halliop, and J. Pharoah, "Experimental investigation of the role of a microporous layer on the water transport and performance of a pem fuel cell," *Journal of Power Sources*, vol. 170, no. 1, pp. 111 – 121, 2007.

[208] J. T. Gostick, M. A. Ioannidis, M. W. Fowler, and M. D. Pritzker, "On the role of the microporous layer in pemfc operation," *Electrochemistry Communications*, vol. 11, no. 3, pp. 576 – 579, 2009.

[209] R. Gonzalez and R. Woods, *Digital Image Processing Third Edition*, M. McDonald, Ed. Pearson Education,Inc., 2008.

[210] I. Toray Industries, Manufacturer Data.

[211] J. Lobato, P. Caizares, M. Rodrigo, C. Ruiz-Lpez, and J. Linares, "Influence of the teflon loading in the gas diffusion layer of pbi-based pem fuel cells," *Journal of Applied Electrochemistry*, vol. 38, pp. 793–802, 2008.

[212] M. Planck, "On the law of distribution of energy in the normal spectrum," *Annalen der Physik*, vol. 4, p. 553, 1901.

[213] J. R. Schott, *Remote Sensing: The Image Chain Approach, 2nd Edition Edition*. Oxford University Press, Inc., 2007.

[214] X. Liu, H. Guo, F. Ye, and C. F. Ma, "Flow dynamic characteristics in flow field of proton exchange membrane fuel cells," *International Journal of Hydrogen Energy*, vol. 33, no. 3, pp. 1040 – 1051, 2008.

[215] A. Radhakrishnan, "Thermal conductivity measurement of gas diffusion layer used in pemfc," Master's thesis, Rochester Institute of Technology, 2009.

[216] T. Ous and C. Arcoumanis, "The formation of water droplets in an air-breathing pemfc," *International Journal of Hydrogen Energy*, vol. 34, no. 8, pp. 3476 – 3487, 2009.